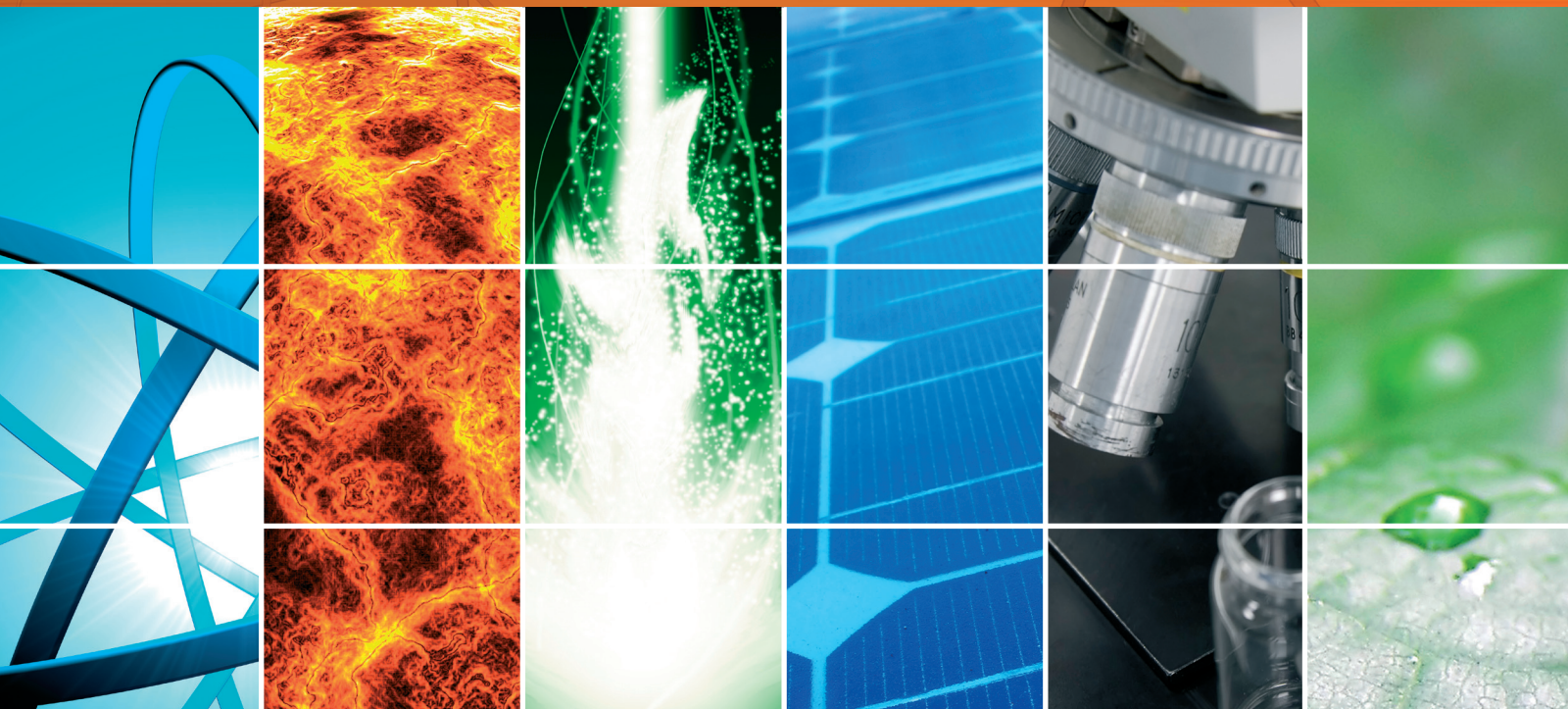


Thin-Film Photovoltaics 2014

Guest Editors: Gaetano Di Marco, Giuseppe Calogero, Aldo Di Carlo,
Salvatore Lombardo, Leonardo Palmisano, and Olindo Isabella





Thin-Film Photovoltaics 2014

International Journal of Photoenergy

Thin-Film Photovoltaics 2014

Guest Editors: Gaetano Di Marco, Giuseppe Calogero,
Aldo Di Carlo, Salvatore Lombardo, Leonardo Palmisano,
and Olindo Isabella



Copyright © 2015 Hindawi Publishing Corporation. All rights reserved.

This is a special issue published in "International Journal of Photoenergy." All articles are open access articles distributed under the Creative Commons Attribution License, which permits unrestricted use, distribution, and reproduction in any medium, provided the original work is properly cited.

Editorial Board

M.S.A. Abdel-Mottaleb, Egypt
Xavier Allonas, France
Nicolas Alonso-Vante, France
Wayne A. Anderson, USA
Yanhui Ao, China
Raja S. Ashraf, UK
Vincenzo Augugliaro, Italy
Detlef W. Bahnemann, Germany
Ignazio Renato Bellobono, Italy
Raghu N. Bhattacharya, USA
Thomas M. Brown, Italy
Stephan Buecheler, Switzerland
Gion Calzaferri, Switzerland
Chuncheng Chen, China
Sung Oh Cho, Republic of Korea
Věra Cimrová, Czech Republic
Juan M. Coronado, Spain
Ying Dai, China
Dionysios D. Dionysiou, USA
Abderrazek Douhal, Spain
Mahmoud M. El-Nahass, Egypt
Polycarpos Falaras, Greece
Chris Ferekides, USA
Paolo Fornasiero, Italy
Hermenegildo García, Spain
Germà Garcia-Belmonte, Spain
Elisa Isabel Garcia-Lopez, Italy
Beverley Glass, Australia
M. A. Gondal, Saudi Arabia
Anthony M. Harriman, UK
Jr-Hau He, Taiwan
Shinya Higashimoto, Japan
Cheuk-Lam Ho, Hong Kong
Wing-Kei Ho, Hong Kong
Fuqiang Huang, China
Jürgen Hüpkes, Germany
Adel A. Ismail, Egypt
Chun-Sheng Jiang, USA
Misook Kang, Republic of Korea
Shahed Khan, USA
Sungjee Kim, Korea

Sun-Jae Kim, Korea
Jong Hak Kim, Korea
Fernando Langa, Spain
Cooper H. Langford, Canada
Tae-Woo Lee, Korea
Lecheng Lei, China
Xinjun Li, China
Zhaosheng Li, China
Stefan Lis, Poland
Vittorio Loddo, Italy
Gongxuan Lu, China
Dongge Ma, China
Nai Ki Mak, Hong Kong
Rajaram S. Mane, India
Dionissios Mantzavinos, Greece
Ugo Mazzucato, Italy
Sheng Meng, China
Jacek Miller, Poland
Claudio Minero, Italy
Thomas Moehl, Switzerland
Antoni Morawski, Poland
Franca Morazzoni, Italy
Fabrice Morlet-Savary, France
Mohammad Muneer, India
Kun Na, Korea
Ebinazar B. Namdas, Australia
Maria da Graa P. Neves, Portugal
Tebello Nyokong, South Africa
Tsuyoshi Ochiai, Japan
Kei Ohkubo, Japan
Haridas Pal, India
Leonidas Palilis, Greece
Leonardo Palmisano, Italy
Ravindra K. Pandey, USA
Hyunwoong Park, Korea
Thierry Pauporté, France
Pierre Pichat, France
Gianluca Li Puma, UK
Tijana Rajh, USA
Peter Robertson, UK
Avigdor Scherz, Israel

Elena Selli, Italy
Ganesh D. Sharma, India
Jinn Kong Sheu, Taiwan
Panagiotis Smirniotis, USA
Bhushan Sopori, USA
Zofia Stasicka, Poland
Elias Stathatos, Greece
Jegadesan Subbiah, Australia
Meenakshisundaram Swaminathan, India
Kazuhiro Takanabe, Saudi Arabia
Mohamad-Ali Tehfe, Canada
K. R. Justin Thomas, India
Yang Tian, China
Nikolai V. Tkachenko, Finland
Ahmad Umar, Saudi Arabia
Thomas Unold, Germany
Veronica Vaida, USA
Roel van De Krol, Germany
Mark van Der Auweraer, Belgium
Rienk Van Grondelle, The Netherlands
Wilfried G.J.H.M. Van Sark, The Netherlands
Sergey Varlamov, Australia
Mingkuai Wang, China
Xuxu Wang, China
Sheng Wang, China
David Worrall, UK
Jeffrey C. S. Wu, Taiwan
Yanfa Yan, USA
Jiannian Yao, China
Minjoong Yoon, Korea
Hongtao Yu, USA
Ying Yu, China
Jiangbo Yu, USA
Klaas Zachariasse, Germany
Juan Antonio Zapien, Hong Kong
Tianyou Zhai, China
Guijiang Zhou, China
Yong Zhou, China
Rui Zhu, China

Contents

Thin-Film Photovoltaics 2014, Gaetano Di Marco, Giuseppe Calogero, Aldo Di Carlo, Salvatore Lombardo, Leonardo Palmisano, and Olindo Isabella
Volume 2015, Article ID 936458, 3 pages

Enhancement of Spectral Response in $\mu\text{c-Si}_{1-x}\text{Ge}_x\text{:H}$ Thin-Film Solar Cells with a-Si:H/ $\mu\text{c-Si:H}$ P-Type Window Layers, Yen-Tang Huang, Cheng-Hang Hsu, and Chuang-Chuang Tsai
Volume 2015, Article ID 841614, 8 pages

Surface Photovoltage Spectroscopy and AFM Analysis of CIGSe Thin Film Solar Cells, Nima E. Gorji, Ugo Reggiani, and Leonardo Sandrolini
Volume 2015, Article ID 829530, 5 pages

Graded Carrier Concentration Absorber Profile for High Efficiency CIGS Solar Cells, Antonino Parisi, Riccardo Pernice, Vincenzo Rocca, Luciano Curcio, Salvatore Stivala, Alfonso C. Cino, Giovanni Cipriani, Vincenzo Di Dio, Giuseppe Ricco Galluzzo, Rosario Miceli, and Alessandro C. Busacca
Volume 2015, Article ID 410549, 9 pages

Light Scattering and Current Enhancement for Microcrystalline Silicon Thin-Film Solar Cells on Aluminium-Induced Texture Glass Superstrates with Double Texture, Yunfeng Yin, Nasim Sahraei, Selvaraj Venkataraj, Sonya Calnan, Sven Ring, Bernd Stannowski, Rutger Schlatmann, Armin G. Aberle, and Rolf Stangl
Volume 2015, Article ID 358276, 8 pages

Optical Characterization of Different Thin Film Module Technologies, R. Ebner, B. Kubicek, G. Újvári, S. Novalin, M. Rennhofer, and M. Halwachs
Volume 2015, Article ID 159458, 12 pages

Measurements and Simulations on the Mechanisms of Efficiency Losses in HIT Solar Cells, Silvio Pierro, Andrea Scuto, Luca Valenti, Marina Foti, Anna Battaglia, Giovanni Mannino, Cosimo Gerardi, Felice Crupi, and Salvatore Lombardo
Volume 2015, Article ID 515767, 7 pages

Editorial

Thin-Film Photovoltaics 2014

**Gaetano Di Marco,¹ Giuseppe Calogero,¹ Aldo Di Carlo,² Salvatore Lombardo,³
Leonardo Palmisano,⁴ and Olindo Isabella⁵**

¹Istituto per i Processi Chimico-Fisici (IPCF), CNR, Viale Ferdinando Stagno d'Alcontres 37, 98158 Messina, Italy

²Centre for Hybrid and Organic Solar Energy (CHOSE), University of Rome "Tor Vergata", Via del Politecnico 1, 00133 Rome, Italy

³Istituto per la Microelettronica e Microsistemi (IMM), CNR, Zona Industriale Ottava Strada 5, 95121 Catania, Italy

⁴DEIM, Università degli Studi di Palermo, Viale delle Scienze, Edificio 6, 90128 Palermo, Italy

⁵Photovoltaic Materials and Devices EEMCS Faculty, Delft University of Technology, Mekelweg 4, 2628 CD Delft, Netherlands

Correspondence should be addressed to Gaetano Di Marco; dimarco@its.me.cnr.it

Received 11 May 2015; Accepted 11 May 2015

Copyright © 2015 Gaetano Di Marco et al. This is an open access article distributed under the Creative Commons Attribution License, which permits unrestricted use, distribution, and reproduction in any medium, provided the original work is properly cited.

The interest toward alternative energy sources to fossil fuels (still the most convenient in terms of efficiency and cost) is current. Initiatives that seek to convert wind, geothermal energy, hydropower, marine, solar thermal energy, and photovoltaics or derived from biomass energy into other forms continue to involve several research groups. For example, the transfer from solar energy into electricity, which in turn can be used for water splitting and for the subsequent production of hydrogen, seems a major challenge to provide a sustainable contribution to the "Earth system" together with the realization of devices having high conversion efficiencies, low environmental impact, and low production costs. In our opinion the use of heterogeneous forms of available energy could definitely give a rational response to the growing global demand of energy, respecting the environment.

This special issue is following a series that began in 2010. The aim is to provide a continuous update on state-of-the-art in the field of materials, nanotechnology, theoretical models, and technological aspects that belong to the science of thin film photovoltaics (TFPV). Despite this issue having a limited number of contributions, it is interesting to point out that the contribution provided by colleagues with their research have kept alive this initiative undertaken by this journal. Here is a timely synthesis of all contributions received which can stimulate the development of new ideas in the field of photovoltaic and highlight interest in this initiative in the future.

In "Graded Carrier Concentration Absorber Profile for High Efficiency CIGS Solar Cells," an innovative CIGS-based solar cells model with a graded doping concentration absorber profile is demonstrated, in order to achieve high efficiency values (up to 21%). A depth-dependent study has shown that the proposed graded carrier concentration profile structures owns the same advantages of a CIGS cell having a Ga back graded profile, thanks to a quasidelectrical field generated through the absorber and directed towards the back-contact. In addition, both the E_C and the E_V increase in the direction of the back-contact; that is, E_g is constant along the depth. For this reason, the proposed cell structure overcomes the limitation of Ga back graded profile presenting a generation process that is definitely more efficient.

In "Enhancement of Spectral Response in $\mu\text{c-Si}_{1-x}\text{Ge}_x$:H Thin-Film Solar Cells with a-Si:H/ $\mu\text{c-Si:H}$ P-Type Window Layers", a technique to improve microcrystalline silicon-germanium p-i-n single-junction thin-film solar cells deposited on textured SnO_2 :F-coated glass substrates is studied. In fact, in thin film silicon solar cells deposited on glass, the prevalent technology is based on hydrogenated amorphous silicon. In this field hydrogenated microcrystalline silicon has attracted attention as alternative promising material, since compared to amorphous Si has a higher resistance to the Staebler-Wronski effect, a light-induced degradation which deteriorates the long-term efficiency, and a narrower bandgap which improves the near-infrared (NIR) response. As further

improvement it has been shown that the addition of Ge into the microcrystalline Si network, that is, the use of a microcrystalline silicon germanium absorber, enhances even more the NIR spectral response. Finally, also the quality of the front transparent conducting oxide (TCO), generally textured $\text{SnO}_2:\text{F}$, has a significant influence on the cell performance. To form hydrogenated microcrystalline Si, a gas mixture of H_2 and SiH_4 with a large H_2 content is generally utilized, and the exposure to H_2 -containing plasma of the $\text{SnO}_2:\text{F}$ TCO is believed to produce Sn reduction which degrades solar cell performance. The effect worsens with the addition of GeH_4 to form the hydrogenated microcrystalline SiGe. In the contribution reported in this special issue it is shown that the performances of hydrogenated microcrystalline SiGe solar cells can be improved by using a novel structure based on a double p-type window layer made of hydrogenated amorphous Si and microcrystalline Si films.

In "Surface Photovoltage Spectroscopy and AFM Analysis of CIGSe Thin Film Solar Cells," the band gap, grain size, and topography of a $\text{Cu}(\text{In,Ga})\text{Se}_2$ (CIGSe) thin film solar cell are analyzed using surface photovoltage spectroscopy (SPV) and atomic force microscopy (AFM) techniques. The sample investigated has been fabricated by a three-stage coevaporation process. The band gap energy of the CIGSe, In_2S_3 , and ZnO is deduced by extrapolation of the SPV signal slopes to the photon energy axis and found to be 1.1, 1.3, and 2.6 eV, respectively. The AFM measurements yield information on orientation of the atomic nucleation and material homogeneity, founding grains very oriented with average size almost uniform $<1\ \mu\text{m}$. The topography presents a homogeneous diffusion of the In_2S_3 or deionized water into the CIGSe layer after the annealing at 400°C . These growth conditions have a strong influence on the surface which looks slightly rough (root mean square 37.8 nm) almost smooth with no cracks.

In "Measurements and Simulations on the Mechanisms of Efficiency Losses in HIT Solar Cells," the optoelectrical behaviour of heterojunction solar cells was investigated by means of TCAD simulations and compared with that of conventional crystalline silicon solar cell. In this way the main problems affecting heterojunction devices could be identified. After measuring and simulating optimized structures from both technologies, two different losses mechanisms could be addressed into heterojunction devices. In particular, the presence of the amorphous silicon layer led to smaller distance between the metal lines causing higher shadowing and to a slight increase of reflectivity around the 600 nm wavelength. That is, a lower fill factor and a higher reflectivity for the heterojunction solar cell could be seen. The fill factor decrease is due to a higher potential loss along the p-n junction that causes a higher diode current. Shrinking the pitch can prevent this shortcoming but causes a higher shadowing. In addition, the not ideal optical coupling between the amorphous silicon and the antireflective coating in the wavelength range from 400 nm to 600 nm causes lower short circuit current density. This effect could be reduced

by reducing the thickness of the amorphous silicon layer; however it cannot be smaller than the value in use to prevent quantum effects.

In "Light Scattering and Current Enhancement for Microcrystalline Silicon Thin-Film Solar Cells on Aluminium-Induced Texture Glass Superstrates with Double Texture," some microcrystalline silicon ($\mu\text{c-Si:H}$) thin solar cells are processed on glass superstrates having both micro- and nanoscale surface textures. The AIT glass superstrates employed in the solar cells are double textured and are prepared by conventional acid etching of the sputter-deposited transparent conductive oxide (TCO). The influence of the surface topology on the optical scattering behavior and on the $\mu\text{c-Si:H}$ film grown was investigated by means atomic force microscopy (AFM), diffuse scattering into air for visible light, and short circuit current enhancement measurements. Also the mean feature size of the textured superstrates is a good indicator for the mean lateral feature size of randomly textured surfaces and can be obtained from AFM image data processing. In order to investigate the benefit of this double texture different samples are used. The resulting double texture has much higher surface roughness (RMS) than the reference sample. As expected, from this study the current enhancement is mainly ascribed to the better light absorption for the infrared light since the haze values in the long-wavelength region improved significantly by using AIT1 and AT2 glass superstrates. However a local shunt formation also emerged, due to defective areas (cracks) formed when the ($\mu\text{c-Si:H}$) films are deposited on AIT glass superstrates above the deep valleys of the microtextured kinks decreasing the solar cells efficiency. Further optimization still needs to be done in order to decrease the shunting effect while maintaining the light scattering abilities of the superstrates.

In "Optical Characterization of Different Thin Film Module Technologies," a combination of fast and nondestructive methods for a complete quality control of three types of thin film solar module technologies such as a-Si, CdTe, and CIS is investigated. The authors propose camera-based measurements using electroluminescence (EL), photoluminescence (PL), and infrared (IR) technologies, with the aim to increase the numbers of detectable defects and to determine their origin. By using the thermal behavior of cells in a module it is possible to see short circuits, shunts, inactive cell parts, moisture, and defective bypass diodes. With the Dark-lock-in thermography a pulsed current is applied to the solar device without illumination and when the current applied as dark current flows in the solar device causes heating which can be detected and analyzed by a cooled microbolometer based IR-camera. EL measurements take advantages of the radiative interband recombination of the excited charge carriers in the solar devices. The light emitted signal is detected by a Si-CCD-camera (range 300 nm–1000 nm). This method is a useful tool for investigating electrical nonhomogeneities caused by intrinsic defects. PL measurements can be used to detect defects throughout the entire solar cell manufacturing process. PL-images help to find out if material defects or contacting problems are the reason for power losses in

solar cells in modules. Anyway according to this study the combination of all these techniques is necessary to identify as many defects as possible in nondestructive way.

*Gaetano Di Marco
Giuseppe Calogero
Aldo Di Carlo
Salvatore Lombardo
Leonardo Palmisano
Olindo Isabella*

Research Article

Enhancement of Spectral Response in $\mu\text{c-Si}_{1-x}\text{Ge}_x\text{:H}$ Thin-Film Solar Cells with a-Si:H/ $\mu\text{c-Si:H}$ P-Type Window Layers

Yen-Tang Huang, Cheng-Hang Hsu, and Chuang-Chuang Tsai

Department of Photonics and Institute of Electro-Optical Engineering, National Chiao Tung University, Hsinchu 30010, Taiwan

Correspondence should be addressed to Yen-Tang Huang; yen.tang.huang@gmail.com

Received 28 July 2014; Accepted 3 November 2014

Academic Editor: Salvatore Lombardo

Copyright © 2015 Yen-Tang Huang et al. This is an open access article distributed under the Creative Commons Attribution License, which permits unrestricted use, distribution, and reproduction in any medium, provided the original work is properly cited.

The hydrogenated amorphous silicon (a-Si:H)/hydrogenated microcrystalline silicon ($\mu\text{c-Si:H}$) double p-type window layer has been developed and applied for improving microcrystalline silicon-germanium p-i-n single-junction thin-film solar cells deposited on textured $\text{SnO}_2\text{:F}$ -coated glass substrates. The substrates of $\text{SnO}_2\text{:F}$, $\text{SnO}_2\text{:F}/\mu\text{c-Si:H(p)}$, and $\text{SnO}_2\text{:F}/\text{a-Si:H(p)}$ were exposed to H_2 plasma to investigate the property change. Our results showed that capping a thin layer of a-Si:H(p) on $\text{SnO}_2\text{:F}$ can minimize the Sn reduction during the deposition process which had H_2 -containing plasma. Optical measurement has also revealed that a-Si:H(p) capped $\text{SnO}_2\text{:F}$ glass had a higher optical transmittance. When the 20 nm $\mu\text{c-Si:H(p)}$ layer was replaced by a 3 nm a-Si:H(p)/17 nm $\mu\text{c-Si:H(p)}$ double window layer in the cell, the conversion efficiency (η) and the short-circuit current density (J_{SC}) were increased by 16.6% and 16.4%, respectively. Compared to the standard cell with the 20 nm $\mu\text{c-Si:H(p)}$ window layer, an improved conversion efficiency of 6.19% can be obtained for the cell having a-Si:H(p)/ $\mu\text{c-Si:H(p)}$ window layer, with $V_{\text{OC}} = 490$ mV, $J_{\text{SC}} = 19.50$ mA/cm², and FF = 64.83%.

1. Introduction

Hydrogenated microcrystalline silicon ($\mu\text{c-Si:H}$) has attracted attentions as a promising material for an absorbing layer in Si-based thin-film solar cells [1–3]. Compared to hydrogenated amorphous silicon (a-Si:H), $\mu\text{c-Si:H}$ has a higher resistance to Staebler-Wronski effect [4]. The effect generally found in amorphous materials could lead to the light-induced degradation [5–7] which deteriorates the long-term film quality as well as the efficiency in solar cells. Moreover, in contrast to the wider bandgap of 1.73 eV for a-Si:H [8], an extended near-infrared (NIR) response arising from the narrower bandgap of 1.1 eV [9, 10] of $\mu\text{c-Si:H}$ film can be attained. However, $\mu\text{c-Si:H}$ has a low absorption coefficient due to its indirect bandgap. A relatively thick $\mu\text{c-Si:H}$ absorber is required for generating sufficient photon-excited carriers. For reducing the thickness of $\mu\text{c-Si:H}$ absorber, $\mu\text{c-Si}_{1-x}\text{Ge}_x\text{:H}$ has been employed as an absorber. Matsui et al. [11] reported that adding Ge into microcrystalline Si-Si network effectively enhanced NIR spectral response. For a $\mu\text{c-Si}_{1-x}\text{Ge}_x\text{:H}$ film having Ge content of 50 at.%, approximately one order of absorption coefficient greater than that of $\mu\text{c-Si:H}$ was

observed. The absorption coefficient can achieve 10^4 cm⁻¹ at 1.5 eV for $\mu\text{c-Si}_{1-x}\text{Ge}_x\text{:H}$. Matsui et al. [12] have later revealed that the $\mu\text{c-Si}_{1-x}\text{Ge}_x\text{:H}$ single-junction solar cell achieved a cell efficiency of 6.3% with Ge content of approximately 20 at.% in the absorber.

For Si-based thin-film solar cells, the quality of the front transparent conducting oxide (TCO) also significantly influences the cell performance. The textured $\text{SnO}_2\text{:F}$ -coated glass substrates have been widely applied. To promote the crystallization of $\mu\text{c-Si:H}$ films, a highly H_2 -containing gas mixture of H_2 and SiH_4 is generally utilized. Although there is a p-type layer on the TCO surface, the energetic hydrogen atom impinging on the surface can further penetrate into subsurface growth zone (up to 20 nm) [13–16]. When the $\text{SnO}_2\text{:F}$ is directly or indirectly exposed to H_2 -containing plasma, Sn reduction could appear and degrade cell performance due to the decreased light absorption [17–19]. In contrast to $\mu\text{c-Si:H}$ film, we have found that adding GeH_4 for $\mu\text{c-Si}_{1-x}\text{Ge}_x\text{:H}$ growth had an adverse effect on crystallization. A much higher H_2 dilution is required to maintain the crystallization of $\mu\text{c-Si}_{1-x}\text{Ge}_x\text{:H}$ films. Thus, to alleviate unfavorable Sn reduction of $\text{SnO}_2\text{:F}$ surface is one

TABLE 1: Parameters for different growth processes and H₂-plasma treatment.

Parameter	unit	a-Si:H(p)	$\mu\text{c-Si:H(p)}$	$\mu\text{c-Si}_{1-x}\text{Ge}_x\text{:H(i)}$	$\mu\text{c-SiO}_x\text{:H(n)}$	H ₂ Plasma
Power density	mW/cm ²	34	325	148	44	325
Growth pressure	pa	40	500	1200	600	500
H ₂ flow	sccm	50	800	1128–1960	1500	800
SiH ₄ flow	sccm	20	10	15	11	0
GeH ₄ flow	sccm	0	0	0.8	0	0
2% B ₂ H ₆ /H ₂ flow	sccm	10	5	0	0	0
1% PH ₃ /H ₂ flow	sccm	0	0	0	5	0
CO ₂ flow	sccm	0	0	0	6	0

of the key issues for achieving high-efficiency $\mu\text{c-Si}_{1-x}\text{Ge}_x\text{:H}$ cells.

Previous works [20, 21] have indicated that zinc oxide (ZnO) has a higher resistance to H₂-containing plasma environment. A thin aluminum-doped zinc oxide (AZO) layer deposited onto SnO₂:F surface has been proposed as a protection layer [22, 23]. However, a magnetron sputtering and a post-annealing treatment may generally be required for reducing the defects of the sputtered AZO and improving AZO/SnO₂:F interface. In this contribution, we introduced a simple in situ PECVD method to protect the SnO₂:F from Sn reduction. The double p-type window layer of a-Si:H/ $\mu\text{c-Si:H}$ has been developed to improve cell performance of $\mu\text{c-Si}_{1-x}\text{Ge}_x\text{:H}$ p-i-n single-junction solar cells. We have investigated the effect of H₂ plasma on the transmittance and the surface morphology of the SnO₂:F. The results demonstrated that capping a thin p-type amorphous silicon (a-Si:H(p)) on SnO₂:F can minimize unfavorable Sn reduction during the deposition of microcrystalline films.

2. Experimental Details

In this work, Si-based films were deposited by a 27.12 MHz multichamber plasma-enhanced chemical vapor deposition (PECVD) system with a single chamber process at a substrate temperature of approximately 200°C. The parameters for different growth processes and H₂-plasma treatment were added in Table 1. The germane flow ratio and hydrogen ratio for SiGe alloys were defined as $R_{\text{GeH}_4} = [\text{GeH}_4]/([\text{GeH}_4] + [\text{SiH}_4])$ and $R_{\text{H}_2} = [\text{H}_2]/([\text{GeH}_4] + [\text{SiH}_4])$, respectively. The hydrogen ratio was varied from 71.4 to 124 with R_{GeH_4} of 0 and 5.06%. The dark and the photoconductivities were measured by an *I-V* measurement system under dark and AM1.5G illumination. The standard cell structure was textured SnO₂:F-coated glass/ $\mu\text{c-Si:H(p)}$ /0.9 μm $\mu\text{c-Si}_{0.88}\text{Ge}_{0.12}\text{:H}/\mu\text{c-SiO}_y\text{:H(n)}/\text{Ag}$, as shown in Figure 1(a). In our previous work [24], the optimization and details of $\mu\text{c-Si}_{1-x}\text{Ge}_x\text{:H}$ absorber were reported. The optimized $\mu\text{c-Si}_{1-x}\text{Ge}_x\text{:H}$ absorber was deposited at $R_{\text{GeH}_4} = 5.06\%$ and $R_{\text{H}_2} = 95.2$, which corresponded to a Ge content of approximately 12 at.%. The film Ge content was evaluated by an X-ray photoelectron spectrometer. On the other hand, n-type $\mu\text{c-SiO}_y\text{:H}$ was employed in the cells. N-type $\mu\text{c-SiO}_y\text{:H}$ has been reported for improving cell performance in thin-film silicon solar cells [25, 26], in which there was less

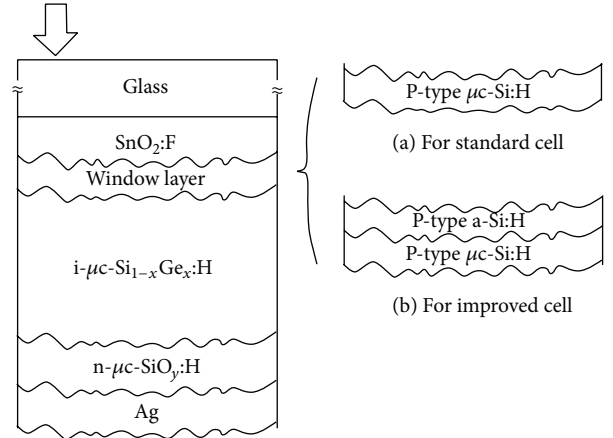


FIGURE 1: Schematic diagrams of the $\mu\text{c-Si}_{1-x}\text{Ge}_x\text{:H}$ p-i-n single-junction solar cells with two types of the window layers: (a) 20 nm $\mu\text{c-Si:H(p)}$ and (b) 3 nm a-Si:H(p)/17 nm $\mu\text{c-Si:H(p)}$.

parasitic light loss in n-type layer and more long-wavelength reflection at i/n interface. Then, the cells were defined by the metal electrode with a cell area of 0.25 cm².

For standard cell, 20 nm thick $\mu\text{c-Si:H(p)}$ layer was applied as a window layer. The $\mu\text{c-Si:H(p)}$ layer was deposited by highly hydrogen-diluted SiH₄ and B₂H₆ ($[\text{H}_2]/[\text{SiH}_4] = 80$ and $[\text{B}_2\text{H}_6]/[\text{SiH}_4] = 1\%$) with 1-minute deposition time. The 200 nm thick $\mu\text{c-Si:H(p)}$ layer has a conductivity of 6.82×10^{-1} S/cm. On the other hand, the 200 nm thick a-SiH(p) deposited with a relatively low H₂-to-SiH₄ ratio of 2.5 has a conductivity of 1.83×10^{-6} S/cm. The schematic structure of the improved cell is illustrated as Figure 1(b).

To investigate the change in the optical property, different film stacks on glass substrate including SnO₂:F, SnO₂:F/ $\mu\text{c-Si:H(p)}$ and SnO₂:F/a-Si:H(p) were prepared and exposed to the H₂ plasma for 1 minute. As can be seen in Table 1, the gas phase concentration of H₂ in the process of $\mu\text{c-Si:H(p)}$ is 98.8% which is quite similar to the pure H₂ process (100%). Parameters such as pressure and power were kept the same for the H₂-plasma treatment and the deposition of $\mu\text{c-Si:H}$ p-layer. This parameter setting should minimize the potential discrepancy between conditions treated by direct H₂-plasma exposure and the growth of $\mu\text{c-Si:H}$ p-layer in the cell process. The samples were then measured by an ultraviolet-visible

TABLE 2: The optical transmittance (%) of the samples at the wavelength of 400 nm and 600 nm: glass/SnO₂:F, glass/SnO₂:F + H₂ plasma, glass/SnO₂:F/1–5 nm a-Si:H(p) + H₂ plasma, and glass/SnO₂:F/1–5 nm μ c-Si:H(p) + H₂ plasma.

Wavelength (nm)	Raw SnO ₂ :F		SnO ₂ :F/a-Si:H(p) + H ₂ plasma			SnO ₂ :F/ μ c-Si:H(p) + H ₂ plasma		
	Raw SnO ₂ :F	SnO ₂ :F + H ₂ plasma	1 nm	3 nm	5 nm	1 nm	3 nm	5 nm
400	73.5	68.3	69.7	71.8	70.3	68.7	68.0	68.1
600	81.8	80.2	80.3	81.5	80.2	79.6	79.6	79.3

spectrophotometry for optical transmittance. The scanning electron microscope (SEM) was also used to reveal the surface morphologies. The experiments of optical transmittance and characterization of surface morphology changes provided clues for the TCO reduction. Furthermore, we characterized the cell performance by an I - V measurement system and a solar simulator under AM1.5G illumination. The quantum efficiency (QE) measurement was used to analyze the spectral response in the range of 300–1100 nm.

3. Results and Discussion

3.1. Effect of Hydrogen Ratio on Microcrystalline Si and SiGe Thin Films. Figure 2(a) shows the crystalline volume fraction (X_C) of μ c-Si:H and μ c-Si_{1-x}Ge_x:H films as a function of hydrogen ratio. When the hydrogen ratio was increased, an increase in the X_C was observed. With a higher hydrogen ratio in the plasma, more atomic hydrogen promotes the crystallization. In contrast to μ c-Si:H film, a higher hydrogen dilution was needed to have the same X_C for μ c-Si_{1-x}Ge_x:H. With an X_C of approximately 50%, the hydrogen ratios for μ c-Si:H and μ c-Si_{1-x}Ge_x:H growth were 80 and 95.2, respectively. The result suggested that the crystallization of the silicon film is suppressed by adding Ge. The difference in the atomic radius interrupts the ordered crystalline network which reduces the degree of crystallization. Moreover, the GeH₃ related species on the film surface during deposition were relatively harder to reach relaxation, which also decreases the crystalline volume fraction. In Figure 2(b), it can be seen that the photo- and dark conductivities of μ c-Si:H and μ c-Si_{1-x}Ge_x:H films increased with raising the hydrogen ratio. With a similar X_C of 50%, μ c-Si:H and μ c-Si_{1-x}Ge_x:H films had the dark conductivities of 7.63×10^{-8} and 6.62×10^{-7} S/cm, with the photoconductivities of 1.86×10^{-5} and 1.06×10^{-5} S/cm, respectively. Compared to μ c-Si:H, the lower photoconductivity and the higher dark conductivity of μ c-Si_{1-x}Ge_x:H were obtained. The more defective μ c-Si_{1-x}Ge_x:H films were mainly due to the Ge incorporation which induces Ge-related defects in the films [11, 12].

3.2. Effect of H₂ Plasma on SnO₂:F-Coated Glass Substrate. As discussed in the previous section, silicon film with Ge incorporation requires a relatively higher hydrogen ratio to have appropriate crystallization. To suppress the Sn reduction of SnO₂:F due to hydrogen plasma during the deposition of the window layer is beneficial for the development of p-i-n μ c-Si_{1-x}Ge_x:H single-junction solar cells.

Table 2 shows the optical transmittance of the different film-stacked glass substrates with or without the H₂-plasma

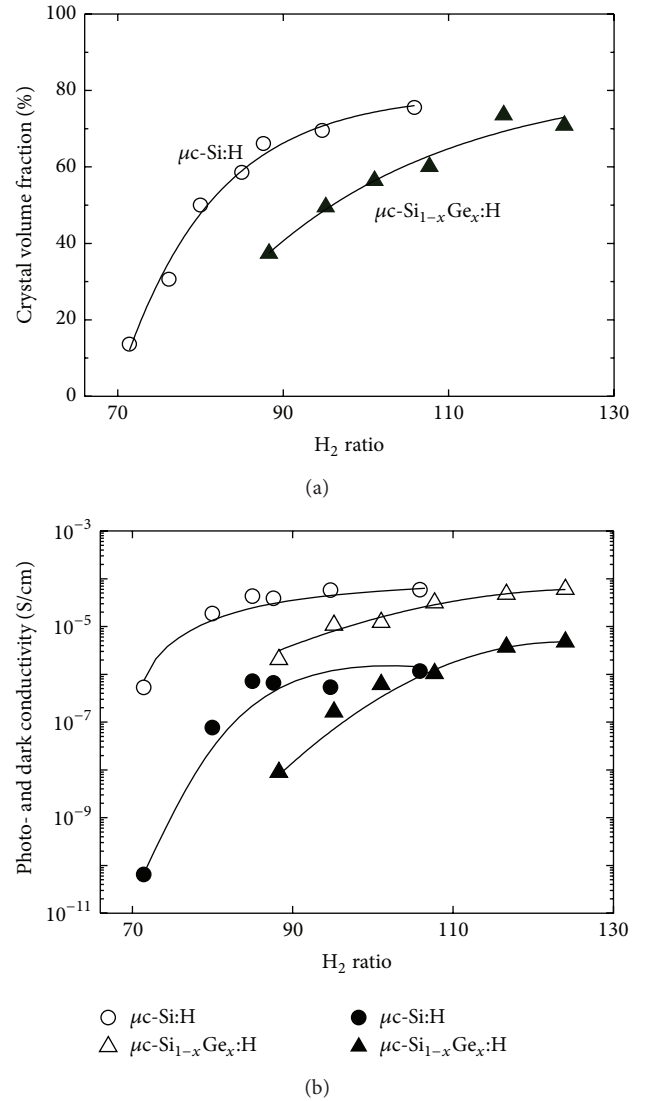


FIGURE 2: (a) Crystalline volume fraction and (b) conductivity as a function of hydrogen ratio for μ c-Si:H ($R_{\text{GeH}_4} = 0$) and μ c-Si_{1-x}Ge_x:H ($R_{\text{GeH}_4} = 5\%$). In (b), the open and closed symbols represent the photo- and the dark conductivities, respectively.

treatment. In order to quantify the difference, the transmittance at the wavelength of 400 nm and 600 nm was compared. When the textured SnO₂:F-coated glass was treated by the H₂-plasma treatment for 1 minute, the transmittance decreased by 2.9% and 1.6% at 400 nm and 600 nm, respectively, compared to the fresh SnO₂:F-coated glass. This transmittance loss of SnO₂:F after H₂-plasma treatment has

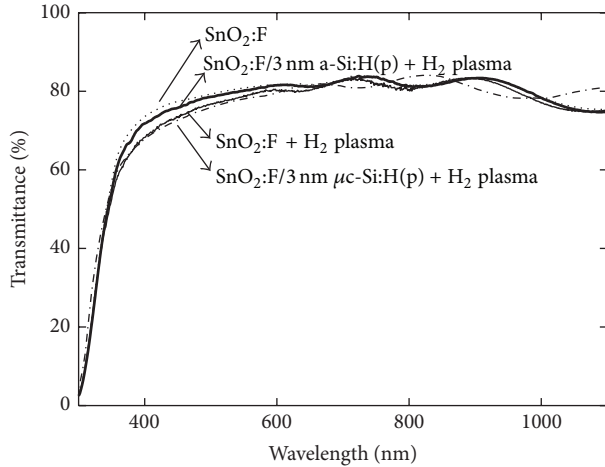


FIGURE 3: The optical transmittance of glass/SnO₂:F (dot line), glass/SnO₂:F + H₂ plasma (slim line), glass/SnO₂:F/3 nm a-Si:H(p) + H₂ plasma (bold line), and glass/SnO₂:F/3 nm μ c-Si:H(p) + H₂ plasma (dash line).

also been demonstrated by Wallinga et al. [18]. For the SnO₂:F underwent H₂-plasma treatment, the binding energies of Sn in 3d_{5/2} orbit shifted to 486.5 eV and 484.8 eV, related to suboxides of tin and metallic tin [18, 19]. Therefore, the suboxides and the metallic Sn reduce the transmittance.

Compared to μ c-Si:H(p), a much lower H₂-to-SiH₄ ratio was used for the deposition of a-Si:H(p) layer. As shown in Table 2, after being treated by H₂ plasma for 1 minute, the sample having structure of SnO₂:F/a-Si:H(p) had higher transmittance, compared to the raw SnO₂:F substrate. When the thickness of a-Si:H(p) on SnO₂:F increased from 1 nm to 3 nm, the transmittance at 400 nm increased from 69.7% to 71.8% and the transmittance at 600 nm increased from 80.3% to 81.5%. On the contrary, the transmittance decreased to 70.3% and 80.2% at 400 nm and 600 nm, respectively, as the thickness of a-Si:H(p) increased to 5 nm. Considering the trade-off between SnO₂:F protection and optical transmission, a 3 nm thick a-Si:H(p) layer was suited for SnO₂:F substrate. Moreover, the H₂-plasma treated SnO₂:F/ μ c-Si:H(p) had the worst transmittance, compared to the H₂-plasma treated SnO₂:F-coated glass and the H₂-plasma treated SnO₂:F/a-Si:H(p). This should be due to the higher hydrogen dilution during the deposition of μ c-Si:H(p) and the less dense μ c-Si:H film for resisting hydrogen penetration.

Figure 3 shows the optical transmittance of different glass substrates in the wavelength ranged from 300 to 1100 nm. The results show that the transmittance of the H₂-plasma treated SnO₂:F/3 nm a-Si:H(p) glass substrate was greater than that of the H₂-plasma treated SnO₂:F glass substrate. For the wavelength shorter than 780 nm, the H₂-plasma treated SnO₂:F/3 nm a-Si:H(p) glass substrate exhibited a superior transmittance, compared to the H₂-plasma treated SnO₂:F/3 nm μ c-Si:H(p) glass substrate. Depositing a thin layer of a-Si:H(p) could be suitable for a microcrystalline silicon process on SnO₂:F based glass substrates.

Figures 4(a), 4(c), and 4(e) show the SEM images of the SnO₂:F surface, SnO₂:F surface covered with 3 nm thick a-Si:H(p), and SnO₂:F surface covered with 3 nm thick μ c-Si:H(p) before the hydrogen plasma treatment, respectively. The surface morphologies of SnO₂:F surface covered with 3 nm thick films (Figures 4(c) and 4(e)) were both similar to the surface morphology of SnO₂:F before hydrogen plasma treatment (Figure 4(a)). To emulate the morphological change after the growth of p-type window layer in the cell process, the samples were treated with 1-minute H₂ plasma. As can be seen in Figure 4(b), the surface of the H₂-plasma treated SnO₂:F had many small particle-like structures with a size of approximately 20 nm, which indicated that the H₂ plasma significantly changed the surface morphology. Study had reported that it could be due to the Sn reduction or surface damage by H₂ plasma [27]. When the SnO₂:F is capped with a 3 nm thick a-Si:H(p) layer followed by the H₂-plasma treatment, the nanostructures were effectively decreased, as shown in Figure 4(d). In contrast, Figure 4(f) showed that the H₂ plasma still significantly changed the surface morphology of the SnO₂:F which was capped with a 3 nm thick μ c-Si:H(p) layer. This surface morphology was similar to the surface of the H₂-plasma treated SnO₂:F. According to these results, a 3 nm thick a-Si:H(p) layer can minimize the effect of H₂ plasma on the SnO₂:F surface, while maintaining acceptable optical performance. Regarding the surface coverage of the 3-nm thick films on the textured SnO₂:F surface, Tsai et al. have reported that the device-quality a-Si:H films were deposited conformally on the substrates with aspect ratio (width/height) ranging from 0.2 to 2 [28]. Since the random pyramidal-like texture of SnO₂:F-coated substrates had smoother surface with roughness of approximately 40 nm and correlation length of approximately 175 nm [29, 30], a 3 nm thick a-Si:H(p) or a 3 nm thick μ c-Si:H(p) film can effectively cover the SnO₂:F surface.

3.3. Improving the Cell Performance of μ c-SiGe:H Single-Junction Cells by Capping an a-Si:H(p) Film on SnO₂:F. Figures 5 and 6 show the *J-V* characteristics and the spectral responses, respectively, of the μ c-Si_{0.88}Ge_{0.12}:H p-i-n solar cells with a 0.9 μ m active layer. The cell performance of the μ c-Si_{0.88}Ge_{0.12}:H p-i-n single-junction solar cells with different p-type window layer is demonstrated in Table 3. The thickness of p-type window layer was kept at 20 nm for comparison. The standard cell with a 20 nm thick single p-type μ c-Si:H window layer can achieve a conversion efficiency of 5.31%. Based on the structure, we employed a 3 nm a-Si:H(p)/17 nm μ c-Si:H(p) double window layer in the μ c-Si_{1-x}Ge_x:H p-i-n single-junction solar cell. This cell with the double p-type window layer has an improved cell performance, especially in the short-circuit current (*J*_{SC}). Compared to the standard cell, the *J*_{SC} can be significantly enhanced from 16.75 to 19.50 mA/cm², which was a 16.4% improvement.

As can be seen in Figure 6, the cell with the a-Si:H(p)/ μ c-Si:H(p) double window layer had a greater quantum efficiency in the wavelength ranging from 300 to 1100 nm. It is also shown in Table 4 that the spectral response of the short wavelength (400 nm) was increased by 19.6% as compared

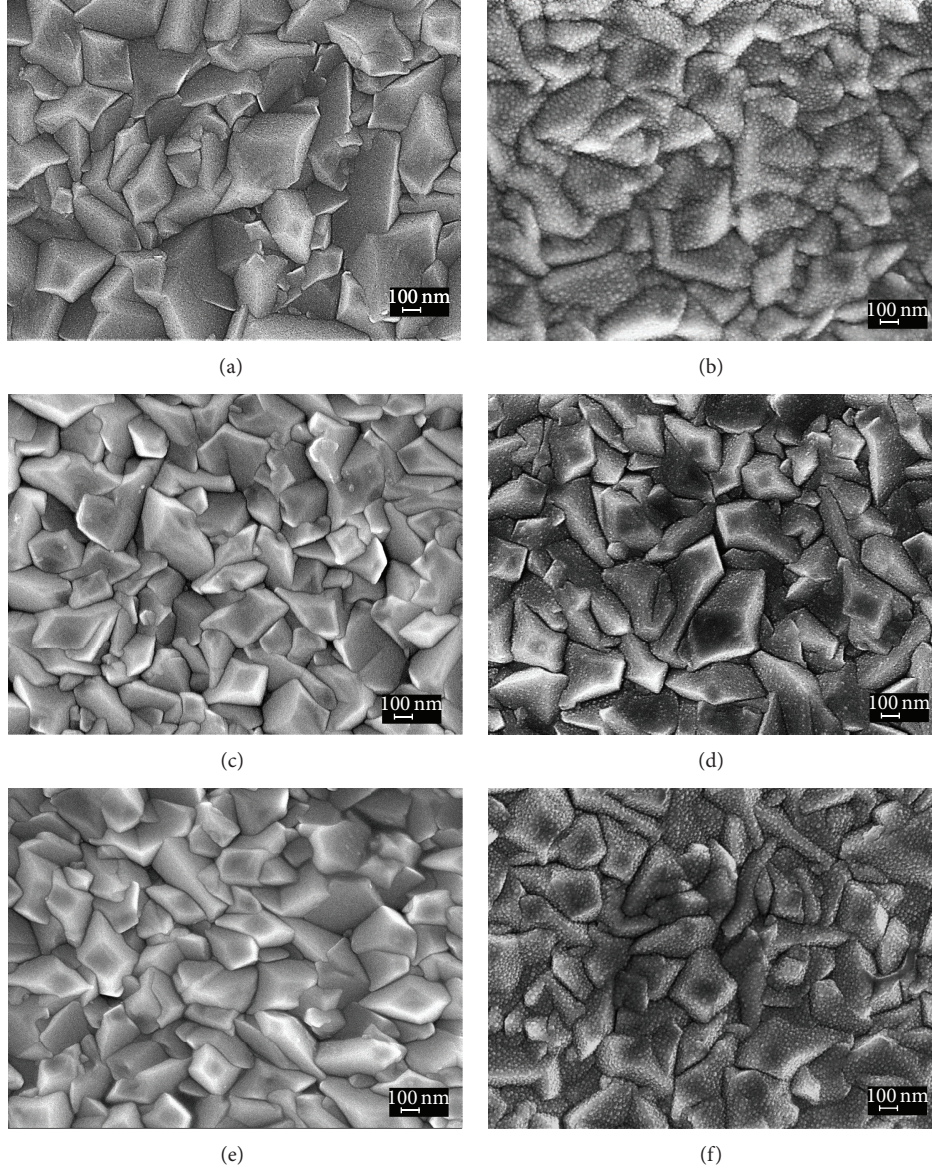


FIGURE 4: The scanning electron microscope (SEM) images of substrates having structures of (a) glass/SnO₂:F, (b) glass/SnO₂:F + H₂ plasma, (c) glass/SnO₂:F/3 nm a-Si:H(p), (d) glass/SnO₂:F/3 nm a-Si:H(p) + H₂ plasma, (e) glass/SnO₂:F/3 nm μ c-Si:H(p), and (f) glass/SnO₂:F/3 nm μ c-Si:H(p) + H₂ plasma.

TABLE 3: The cell performance of the μ c-Si_{0.88}Ge_{0.12}:H p-i-n single-junction solar cells with different p-type window layers.

Window layer	V_{OC} (mV)	J_{SC} (mA/cm ²)	FF (%)	Eff. (%)
μ c-Si:H(p)	480	16.75	66.08	5.31
a-Si:H(p)/ μ c-Si:H(p)	490	19.50	64.83	6.19
a-Si:H(p)/H ₂ plasma/ μ c-Si:H(p)	500	18.19	64.77	5.89
H ₂ plasma/a-Si:H(p)/ μ c-Si:H(p)	465	14.22	63.35	4.20

to the cell having only μ c-Si:H(p). Moreover, the long-wavelength (800 nm) absorption was increased by 32.4%. The improved spectral response can be due to the less Sn reduction of the SnO₂:F surface. More incident light can get into the active layer of the cell and be absorbed to generate photoexcited carriers. Besides, the open circuit voltage (V_{OC})

was also enhanced by 10 mV. The larger V_{OC} could be attributed to a lower defect density at the TCO/p interface or in the p-layer, which has less metastable suboxides of tin and metallic tin arising from Sn reduction. The Sn reduction could also decrease work function of SnO₂:F which would lead to a larger potential barrier at the TCO/p interface.

TABLE 4: The external quantum efficiency at the wavelength of 400, 600, and 800 nm for the $\mu\text{c-Si}_{0.88}\text{Ge}_{0.12}:\text{H}$ p-i-n single-junction solar cells with different p-type window layer.

Window layer	QE _{400 nm}	QE _{600 nm} %	QE _{800 nm}	J _{SC} (QE) mA/cm ²
$\mu\text{c-Si}:\text{H}(\text{p})$	34.02	72.48	31.39	16.74
a-Si:H(p)/ $\mu\text{c-Si}:\text{H}(\text{p})$	40.68	79.58	41.56	19.25
a-Si:H(p)/H ₂ plasma/ $\mu\text{c-Si}:\text{H}(\text{p})$	39.85	78.00	32.50	17.98
H ₂ plasma/a-Si:H(p)/ $\mu\text{c-Si}:\text{H}(\text{p})$	22.45	65.31	26.94	14.47

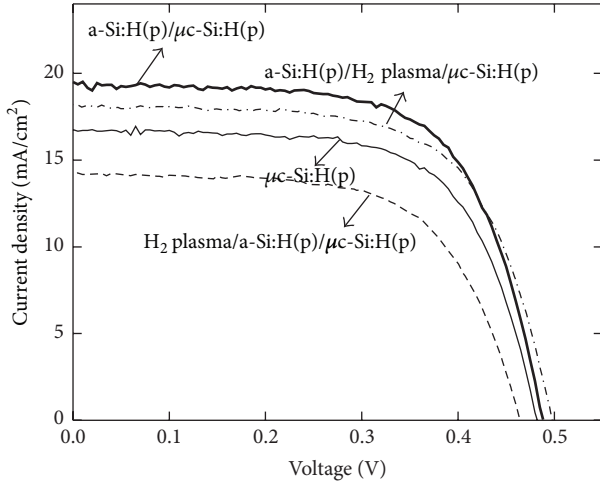


FIGURE 5: The J - V characteristics of $\mu\text{c-Si}_{0.88}\text{Ge}_{0.12}:\text{H}$ p-i-n single-junction solar cells with different p-type window layers.

The $\text{SnO}_2:\text{F}$ can be protected by capping the 3 nm thick a-Si:H(p) layer to minimize the Sn reduction which comes from the sequent films growth of $\mu\text{c-Si}:\text{H}(\text{p})$ and $\mu\text{c-Si}_{0.88}\text{Ge}_{0.12}:\text{H}$ layers with high H₂-containing plasma environment. The improved TCO/p interface enhanced the built-in field and facilitated the carrier transport. As a result, the cell with the a-Si:H(p)/ $\mu\text{c-Si}:\text{H}(\text{p})$ double window layer reached a greater conversion efficiency of 6.19%, which is significantly increased by 16.6% compared to the standard cell structure.

We have further investigated the durability of the double p-type window layer against Sn reduction of the $\text{SnO}_2:\text{F}$ surface. When the H₂ plasma/a-Si:H(p)/ $\mu\text{c-Si}:\text{H}(\text{p})$ structure was implemented as the window layer in the cell, the V_{OC} decreased to 465 mV and the J_{SC} decreased to 14.22 mA/cm². The drop of V_{OC} may be due to more defects at TCO/p interface. The significant absorption loss in the wavelength ranging from 300 to 1100 nm was revealed by the quantum efficiency measurement, which would lead to the decrease in J_{SC} . When the p-i-n cell was prepared on the direct H₂-plasma treated $\text{SnO}_2:\text{F}$ surface, the reduction of SnO_2 liberated Sn, which could migrate into p-layer [31]. In addition, oxygen could also diffuse to p-layer and form SiO_x [31–34]. As a result, these defects led to a built-in potential loss which degraded cell performance of the device. On the other hand, using the a-Si:H(p)/H₂ plasma/ $\mu\text{c-Si}:\text{H}(\text{p})$ structure as the window layer in the cell had only slight degradation of J_{SC} and V_{OC} , as compared to the optimized a-Si:H(p)/ $\mu\text{c-Si}:\text{H}(\text{p})$

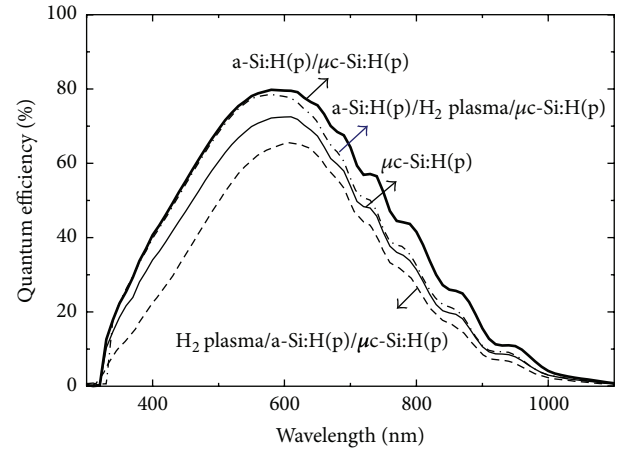


FIGURE 6: The quantum efficiency of $\mu\text{c-Si}_{0.88}\text{Ge}_{0.12}:\text{H}$ p-i-n single-junction solar cells with different p-type window layers.

structure. This suggested that the 3 nm thick a-Si:H(p) layer reduced the effect of H₂ plasma on $\text{SnO}_2:\text{F}$ surface compared to the H₂ plasma/a-Si:H(p)/ $\mu\text{c-Si}:\text{H}(\text{p})$ structure. In contrast to the optimized cell, lower cell efficiency of 5.89% and J_{SC} of 18.19 mA/cm² were shown. The result indicates that the thin a-Si:H(p) layer cannot completely eliminate the effect of H₂ plasma on $\text{SnO}_2:\text{F}$ surface. Certain amount of hydrogen radical could still affect $\text{SnO}_2:\text{F}$ surface during the growth of a-Si:H(p) layer. However, considering the absorption loss arising from the a-Si:H(p) layer, a thickness of 3 nm is suited for optimizing the $\mu\text{c-SiGe}:\text{H}$ single-junction cell performance.

On the other hand, the enhancement in EQE between cells with $\mu\text{c-Si}:\text{H}(\text{p})$ and a-Si:H(p)/ $\mu\text{c-Si}:\text{H}(\text{p})$ can only be partly explained by the difference in transmittance observed between the H₂-plasma treated $\text{SnO}_2:\text{F}$ and the 3 nm thick a-Si:H(p) capped $\text{SnO}_2:\text{F}$ as shown in Figure 3. This indicated that the H₂ plasma also degraded the electrical property of the $\text{SnO}_2:\text{F}$ substrates. Kambe et al. reported that [35] H₂-plasma treated $\text{SnO}_2:\text{F}$ had an increased resistivity and a decreased hall mobility. In addition, the liberated Sn may migrate into the p-layer [31], which causes the degradation of the doped layer. In this study, the significant improvement of the cell performance should majorly arise from the improved TCO/p interface, accompanied with minor optical improvement. In comparison with the state-of-art $\mu\text{c-Si}_{1-x}\text{Ge}_x:\text{H}$ cell with an efficiency of 8.2% ($J_{\text{SC}} = 25.5 \text{ mA/cm}^2$, $V_{\text{OC}} = 0.494 \text{ V}$, and

FF = 0.651) reported by Matsui et al. [36], the reference cell reported in this work exhibited comparable V_{OC} and FF but lower J_{SC} . The reduction in J_{SC} can be mainly attributed to the difference in front TCO layer and antireflection coating. The commercial SnO_2 :F-coated substrate is much more chemically unstable in the hydrogen-rich plasma than the ZnO :Ga, which limited the J_{SC} of the reference cell. Furthermore, since the surface texture of commercial SnO_2 :F-coated substrate is not optimized for the $\mu\text{C-Si}_{1-x}\text{Ge}_x$:H cell [36], the chemically etched ZnO :Ga should lead to an enhancement in J_{SC} . In our case, the lack of antireflection bilayer in the reference cell also posted a constraint on J_{SC} in our case [37]. We have demonstrated that the protection of SnO_2 :F surface from the hydrogen-rich plasma significantly enhanced the J_{SC} from 16.75 to 19.50 mA/cm^2 in this work. Further improvement on performance of solar cell is expected as light-trapping technique and optimization on the process condition are performed in the current cell.

4. Conclusions

In conclusion, we have shown that H_2 plasma significantly degraded the transmittance and changed the surface morphology of SnO_2 :F. An adequate thickness of a-Si:H(p) layer has been successfully applied to minimize the harmful H_2 -plasma effect on SnO_2 :F surface during the sequent deposition of $\mu\text{C-Si:H}$ (p) and $\mu\text{C-SiGe:H}$ layers. In contrast to the standard $\mu\text{C-Si}_{0.88}\text{Ge}_{0.12}$:H p-i-n single-junction cell with a 20 nm thick $\mu\text{C-Si:H}$ (p) window layer, an improved cell performance can be achieved by employing the 3 nm a-Si:H(p)/17 nm $\mu\text{C-Si:H}$ (p) window layer. Due to an improvement in TCO/p interface, the better spectral response at the wavelength of 300–1100 nm was observed. The corresponding J_{SC} increased from 16.75 to 19.50 mA/cm^2 . As a result, the conversion efficiency was improved from 5.31% to 6.19% which was a marked increase of 16.6%.

Conflict of Interests

The authors do not have any conflict of interests with the content of the paper.

Acknowledgments

This study was sponsored by the National Science Council in Taiwan under contract nos. MOST-103-3113-P-008-001 and MOST-103-2221-E-009-068. The Instrument Center of the National Science Council has provided support to complete this research.

References

- [1] A. V. Shah, J. Meier, E. Vallat-Sauvain et al., "Material and solar cell research in microcrystalline silicon," *Solar Energy Materials and Solar Cells*, vol. 78, no. 1–4, pp. 469–491, 2003.
- [2] K. Saito, M. Sano, S. Okabe, S. Sugiyama, and K. Ogawa, "Microcrystalline silicon solar cells fabricated by VHF plasma CVD method," *Solar Energy Materials & Solar Cells*, vol. 86, no. 4, pp. 565–575, 2005.
- [3] B. Yan, G. Yue, X. Xu, J. Yang, and S. Guha, "High efficiency amorphous and nanocrystalline silicon solar cells," *Physica Status Solidi (A) Applications and Materials Science*, vol. 207, no. 3, pp. 671–677, 2010.
- [4] D. L. Staebler and C. R. Wronski, "Reversible conductivity changes in discharge-produced amorphous Si," *Applied Physics Letters*, vol. 31, no. 4, pp. 292–294, 1977.
- [5] F. Meillaud, E. Vallat-Sauvain, X. Niquille et al., "Light-induced degradation of thin film amorphous and microcrystalline silicon solar cells," in *Proceedings of the 31st IEEE Photovoltaic Specialists Conference*, pp. 1412–1415, January 2005.
- [6] J. Meier, R. Flückiger, H. Keppner, and A. Shah, "Complete microcrystalline p-i-n solar cell—crystalline or amorphous cell behavior," *Applied Physics Letters*, vol. 65, no. 7, pp. 860–862, 1994.
- [7] M. Stutzmann, W. B. Jackson, and C. C. Tsai, "Light-induced metastable defects in hydrogenated amorphous silicon: a systematic study," *Physical Review B*, vol. 32, no. 1, pp. 23–47, 1985.
- [8] C. R. Wronski, S. Lee, M. Hicks, and S. Kumar, "Internal photoemission of holes and the mobility gap of hydrogenated amorphous silicon," *Physical Review Letters*, vol. 63, no. 13, pp. 1420–1423, 1989.
- [9] N. Beck, P. Torres, J. Fric et al., "Optical and electrical properties of undoped microcrystalline silicon deposited by the VHF-GD with different dilutions of silane in hydrogen," *Proceedings of the Materials Research Society Symposium*, vol. 452, pp. 761–766, 1997.
- [10] M. A. Green, "Third generation photovoltaics: solar cells for 2020 and beyond," *Physica E: Low-Dimensional Systems and Nanostructures*, vol. 14, no. 1–2, pp. 65–70, 2002.
- [11] T. Matsui, M. Kondo, K. Ogata, T. Ozawa, and M. Isomura, "Influence of alloy composition on carrier transport and solar cell properties of hydrogenated microcrystalline silicon-germanium thin films," *Applied Physics Letters*, vol. 89, no. 14, Article ID 142115, 2006.
- [12] T. Matsui, C.-W. Chang, T. Takada, M. Isomura, H. Fujiwara, and M. Kondo, "Microcrystalline $\text{Si}_{1-x}\text{Ge}_x$ solar cells exhibiting enhanced infrared response with reduced absorber thickness," *Applied Physics Express*, vol. 1, no. 3, Article ID 031501, 2008.
- [13] K. Nakamura, K. Yoshino, S. Takeoka, and I. Shimizu, "Roles of atomic hydrogen in chemical annealing," *Japanese Journal of Applied Physics*, vol. 34, no. 2, pp. 442–449, 1995.
- [14] I. An, Y. Li, C. R. Wronski, and R. W. Collins, "Sub-surface equilibration of hydrogen with the a-Si:H network under film growth conditions," *Materials Research Society Symposium Proceedings*, vol. 297, p. 43, 1993.
- [15] A. Matsuda, "Growth mechanism of microcrystalline silicon obtained from reactive plasmas," *Thin Solid Films*, vol. 337, no. 1–2, pp. 1–6, 1999.
- [16] A. Matsuda, "Microcrystalline silicon: growth and device application," *Journal of Non-Crystalline Solids*, vol. 338–340, no. 1, pp. 1–12, 2004.
- [17] R. Das, T. Jana, and S. Ray, "Degradation studies of transparent conducting oxide: a substrate for microcrystalline silicon thin film solar cells," *Solar Energy Materials and Solar Cells*, vol. 86, no. 2, pp. 207–216, 2005.
- [18] J. Wallinga, W. M. Arnoldbik, A. M. Vredenberg, R. E. I. Schropp, and W. F. van der Weg, "Reduction of tin oxide by hydrogen radicals," *Journal of Physical Chemistry B*, vol. 102, no. 32, pp. 6219–6224, 1998.

- [19] S. Major, M. C. Bhatnagar, S. Kumar, and K. L. Chopra, "The degradation of fluorine doped tin oxide films in a hydrogen plasma," *Journal of Vacuum Science and Technology A*, vol. 6, no. 4, pp. 2415–2420, 1988.
- [20] S. Major, S. Kumar, M. Bhatnagar, and K. L. Chopra, "Effect of hydrogen plasma treatment on transparent conducting oxides," *Applied Physics Letters*, vol. 49, no. 7, pp. 394–396, 1986.
- [21] S. Kumar and B. Drevillon, "A real time ellipsometry study of the growth of amorphous silicon on transparent conducting oxides," *Journal of Applied Physics*, vol. 65, no. 8, pp. 3023–3034, 1989.
- [22] R. H. Franken, C. H. M. van der Werf, J. Löffler, J. K. Rath, and R. E. I. Schropp, "Beneficial effects of sputtered ZnO:Al protection layer on SnO₂:F for high-deposition rate hot-wire CVD p-i-n solar cells," *Thin Solid Films*, vol. 501, no. 1-2, pp. 47–50, 2006.
- [23] A. Masuda, K. Imamori, and H. Matsumura, "Influence of atomic hydrogen on transparent conducting oxides during hydrogenated amorphous and microcrystalline Si preparation by catalytic chemical vapor deposition," *Thin Solid Films*, vol. 411, no. 1, pp. 166–170, 2002.
- [24] Y. T. Huang, H. J. Hsu, S. W. Liang, C. H. Hsu, and C. C. Tsai, "Development of hydrogenated microcrystalline silicon-germanium alloys for improving long-wavelength absorption in Si-based thin-film solar cells," *International Journal of Photoenergy*, Article ID 579176, pp. 1–7, 2014.
- [25] P. Delli Veneri, L. V. Mercaldo, and I. Usatii, "Silicon oxide based n-doped layer for improved performance of thin film silicon solar cells," *Applied Physics Letters*, vol. 97, no. 2, Article ID 023512, 2010.
- [26] S. W. Liang, Y. T. Huang, H. J. Hsu, C. H. Hsu, and C. C. Tsai, "Applications of $\mu\text{c-SiO}_x\text{:H}$ as integrated n-layer and back transparent conductive oxide for a-Si:H/ $\mu\text{c-Si:H}$ tandem cells," *Japanese Journal of Applied Physics*, vol. 53, no. 5S1, Article ID 05FV08, 2014.
- [27] H. C. Weller, R. H. Mauch, and G. H. Bauer, "Novel type of ZnO studied in combination with 1.5eV a-SiGe:H pin diodes," in *Proceedings of the 22th IEEE Photovoltaic Specialists Conference*, pp. 1290–1295, Las Vegas, Nev, USA, October 1991.
- [28] C. C. Tsai, J. C. Knights, G. Chang, and B. Wacker, "Film formation mechanisms in the plasma deposition of hydrogenated amorphous silicon," *Journal of Applied Physics*, vol. 59, no. 8, pp. 2998–3001, 1986.
- [29] K. Jäger, M. Fischer, R. A. C. M. M. Van Swaaij, and M. Zeman, "A scattering model for nano-textured interfaces and its application in opto-electrical simulations of thin-film silicon solar cells," *Journal of Applied Physics*, vol. 111, no. 8, Article ID 083108, 2012.
- [30] K. Sato, Y. Gotoh, Y. Wakayama, Y. Hayashi, K. Adachi, and H. Nishimura, "Highly textured SnO₂:F TCO films for a-Si solar cells," *Reports of the Research Laboratory, Asahi Glass*, vol. 42, pp. 129–137, 1992.
- [31] A. Nuruddin and J. R. Abelson, "Improved transparent conductive oxide/p⁺/i junction in amorphous silicon solar cells by tailored hydrogen flux during growth," *Thin Solid Films*, vol. 394, no. 1-2, pp. 49–63, 2001.
- [32] K. Kawabata, Y. Shiratsuki, T. Hayashi, K. Yamada, S. Miyazaki, and M. Hirose, "Diffusion barrier effect of ultra-thin photo-nitrided a-Si:H overlayer on SnO₂/glass substrate," *Japanese Journal of Applied Physics, Part 2: Letters*, vol. 30, no. 7B, pp. L1231–L1234, 1991.
- [33] W. Beyer, J. Hüpkes, and H. Stiebig, "Transparent conducting oxide films for thin film silicon photovoltaics," *Thin Solid Films*, vol. 516, no. 2–4, pp. 147–154, 2007.
- [34] A. Eicke and G. Bilger, "XPS and SIMS characterization of metal oxide/amorphous silicon-carbon interfaces," *Surface and Interface Analysis*, vol. 12, no. 6, pp. 344–350, 1988.
- [35] M. Kambe, K. Sato, D. Kobayashi et al., "TiO₂-coated transparent conductive oxide (SnO₂:F) films prepared by atmospheric pressure chemical vapor deposition with high durability against atomic hydrogen," *Japanese Journal of Applied Physics*, vol. 45, no. 8–11, pp. L291–L293, 2006.
- [36] T. Matsui, H. Jia, and M. Kondo, "Thin film solar cells incorporating microcrystalline Si_{1-x}Ge_x as efficient infrared absorber: an application to double junction tandem solar cells," *Progress in Photovoltaics: Research and Applications*, vol. 18, no. 1, pp. 48–53, 2010.
- [37] T. Fujibayashi, T. Matsui, and M. Kondo, "Improvement in quantum efficiency of thin film Si solar cells due to the suppression of optical reflectance at transparent conducting oxide/Si interface by TiO₂/ZnO antireflection coating," *Applied Physics Letters*, vol. 88, no. 18, Article ID 183508, 2006.

Research Article

Surface Photovoltage Spectroscopy and AFM Analysis of CIGSe Thin Film Solar Cells

Nima E. Gorji, Ugo Reggiani, and Leonardo Sandrolini

Department of Electrical, Electronic, and Information Engineering, University of Bologna, 40136 Bologna, Italy

Correspondence should be addressed to Nima E. Gorji; nima.eshaghgorji2@unibo.it

Received 31 July 2014; Revised 17 September 2014; Accepted 28 October 2014

Academic Editor: Olindo Isabella

Copyright © 2015 Nima E. Gorji et al. This is an open access article distributed under the Creative Commons Attribution License, which permits unrestricted use, distribution, and reproduction in any medium, provided the original work is properly cited.

The band gap, grain size, and topography of a Cu(In,Ga)Se₂ (CIGSe) thin film solar cell are analyzed using surface photovoltage spectroscopy (SPV) and atomic force microscopy (AFM) techniques. From the steep increase in SPV signal the band gap of the CIGSe absorber, In₂S₃ and ZnO layers are extracted and found to be 1.1, 1.3 and 2.6 eV, respectively. Already below the band gap of ZnO layer, a slight SPV response at 1.40 eV photon energies is observed indicating the presence of deep donor states. The root mean square (rms) of the surface roughness is found to be 37.8 nm from AFM surface topography maps. The grain sizes are almost uniform and smaller than 1 μm.

1. Introduction

Surface photovoltage spectroscopy is a nondestructive but very precise technique to extract the band gap of thin film devices as well as the energy levels of shallow or deep defects distributed through the surface and bulk of the material [1]. Several different graded band gap profiles were proposed and simulated for CIGSe thin film solar cells [2]. Thus, the SPV technique could be used to extract the band gap of fabricated devices with similar graded profiles. Moreover, this technique can characterize the effect of grain boundaries and surface electronics which are the critical aspects of such polycrystalline materials [3]. CdTe semiconductors were already analyzed with the SPV method in order to verify the role of the level and concentration of deep defects on the electrical resistivity (or conductivity) of the layer after deposition [4]. It is well-known that the deep defects around the Fermi level or at the mid-gap (0.7-0.8 eV) are responsible for the low conductivity of the semiconductor. In thin film solar cell fabrication, the postgrowth treatment and annealing at the high temperature can induce such defects across the film thickness. These recombination centers are the complexes of vacancy-ions or metallic defects interdiffused into the junction at high temperature. Moreover, the metallic back contacts can critically influence the carrier transport

through the film. When uncompensated defects increase at the space charge region, the electric field is reduced to a narrower region at the junction. This causes an uncompleted transport of the carriers to the respective electrodes and increases the recombination or series resistance of the device. However, the SPV method has to be accompanied with other techniques which can detect the origin of such defects. Thus, investigating the grain boundaries, traps, and dislocations (morphology) of the films can assist to understand the defect/trap resources many of which diffuse from the back contact to the junction through the grain boundaries. Further studies on the surface topography of thin film devices can be achieved in nanometer scale by atomic force microscopy. AFM can scan the surface roughness and grain sizes with different orientation of the crystal facets which form areas with different work functions [1]. In the present study, the band gap, grain size, and topography of a CIGSe thin film device are analyzed using SPV and AFM techniques. The SPV signals for a wide range of illuminated photon energies can verify the graded band gap where the energy gap of each layer is extracted. Similar to photoluminescence studies, the amplitude of the peaks represents the presence of defects across the film. These defects are detected and scanned by the AFM method to analyze their origin and type. AFM analysis of Liao et al. on a similar device revealed that the film

homogeneity, grain size, and surface roughness play a critical role on the characteristics of the finished device [5].

2. Experimental Procedure

The sample has been fabricated by a three-stage coevaporation process in the Institut des Matériaux Jean Rouxel, Université de Nantes, Nantes, France. The following data were provided by the manufacturer. The thin film solar cell investigated in this work is a heterojunction SLG/Mo/CIGSe/ In_2S_3 /ZnO/ZnO:Al. SLG is 3 mm soda-lime glass substrate coated with a 300 nm Mo layer. The thicknesses of CIGSe and In_2S_3 are 1.8 and 50 μm , respectively. The In_2S_3 buffer layer was grown by coevaporation of In and S elements. The ratio of In and Ga (group III) is $\text{Ga}/(\text{In}+\text{Ga}) = 0.25$. The process was bithermal for the CIGSe (with chalcopyrite structure), 400–620°C measured by thermocouple at the back of the cell. The deposition temperature for In_2S_3 was 175°C. CIGSe has a chalcopyrite structure, and In_2S_3 is in the beta form, which is a defect spinel structure. Further information about the fabrication details can be found in [6]. The band gap of the absorber layer should have been graded through a three-stage coevaporation process (between 1.1 eV and 1.3 eV) and is V-shape. The $\text{Ga}/(\text{In}+\text{Ga})$ ratio rules the band gap and the “natural” gradients (inherent to the 3-stage process used for the CIGSe growth). The minimum Ga content (thus minimum E_g) is about 200 nm far from the CIGSe surface. In principal, the minimum E_g is about 1.1 eV whereas the top CIGSe as well as the CIGSe close to the Mo back contact can be 1.2–1.3 eV. The area of the cell is 0.5 cm^2 .

Then, the CIGSe/ In_2S_3 structure has been covered with standard window bilayer consisting of ZnO (50 nm) and conductive ZnO:Al (200 nm). These two oxide layers have been deposited consecutively in the same chamber by RF sputtering (no air exposure after the ZnO deposition). CIGSe/ In_2S_3 structure has been rinsed with deionized water. Then the completed device was annealed in air at 200°C for 20 minutes.

For the SPV measurements at room temperature, the photon beam generated by a white light source passed through the monochromator SPEX 500M and was focused onto the sample surface. The contribution of the local photocurrent to the tunneling current while sweeping the voltage applied to the conductive tip allowed the measurement of the SPV signal in a wide spectral range from 300 to 2000 nm using different gratings and light sources (quartz-tungsten-halogen and xenon lamps). In the SPV experiment, with the beam on, at the interface of the CIGSe/ In_2S_3 layer the equilibrium was driven away and the photons of the beam created the electron hole pairs. The built-in potential separates the pairs near the band edge which creates a negative photovoltage at the CIGSe surface called surface photovoltage. However, the other properties both from surface and subsurface of the film, that is, the width of the surface space charge region and the recombination rate, contributed to the SPV signal [7–9]. Moreover, surface topography was performed by noncontact mode AFM (NT MDT-Solver PRO 47). Silicon tips coated with Pt/Ir, diamond tips and conductive nanoneedles (Ag_2Ga

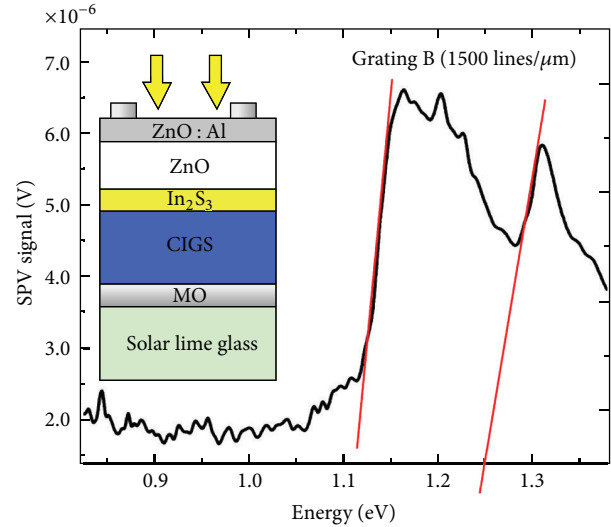


FIGURE 1: SPV signal versus photon energy impinging through grating B (1500 lines/ μm).

Nauganeedles) were used to obtain the current maps (Ag_2Ga Nauganeedles). The topographic and current images were obtained simultaneously, as AFM tip scans the surface and the current is measured. SPV and AFM analyses were carried out in the laboratory “Physics of Defects in Semiconductors,” Department of Physics, University of Bologna, Bologna, Italy.

3. Results and Discussion

3.1. SPV Analysis. Surface photovoltage spectroscopy analysis is based on measuring the SPV signal (which is a light-induced variation of the surface potential) as a function of the impinging photon beam energy. Here, we consider the application of SPV measurements on CIGSe materials for the approximate determination of the graded band gap and understanding the surface formation.

Figure 1 shows the SPV signal plotted versus the energy of impinging photons passing through grating B with 1500 lines/ μm for photon energies in the range of 0.8–1.4 eV. The most important features to interpret a SPV spectrum are the sharp slope changes, “knees,” associated with an abrupt increase of an additional carrier excitation mechanism. At low photon excitation energies (below 0.8 eV) the SPV signal is undetectable since the light energy is not sufficient to excite the charge carriers in CIGSe material. Three peaks and two knees for $h\nu > 1.1$ eV are displayed in Figure 1. At around 1.1 and 1.2 eV, two peaks are observed with almost the same amplitude of 6.5 μV . The next peak is seen at energies higher than 1.3 eV but with a lower SPV signal magnitude (5.9 μV). These results indicate that the E_g of CIGSe is graded with a V-shape with the minimum of 1.1 eV whereas it is about 1.2–1.3 eV at the top and close to Mo. We might also note that the peak related to 1.3 eV can be due to Cu interdiffusion to In_2S_3 (formation of $\text{In}_2\text{S}_3:\text{Cu}$). Furthermore, the first knee occurs at subband gap photon energies and corresponds to the onset of carrier excitation from surface

states. This assumption should also include the transitions of the uncompensated defects localized at levels above the valence band. The second knee happens in the vicinity of the band gap energy and corresponds to the onset of the band-to-band carrier excitation. The peak seen in 1.2 eV may be a noise coming from the SPV measurements. However the experiments were reproducible. Thus, it can be a shallow donor level in the CIGSe absorber layer in close level to the minimum of conduction band.

The very small values of the SPV signal (2–7 μV) were suggested to arise from the high recombination rate of carriers at the surface [7]. However, the strong electric field at the interface of the absorber/window layer of the cell (normally $\sim 1 \mu\text{V}/\text{cm}$) can collect the carriers at the space charge region. Several slopes in the SPV signal indicate the variation of the CIGSe band gap, the presence of surface states, and acceptor/donor defects (deep/shallow).

At photon energies close to E_g , the SPV signal should increase rapidly up to a saturation value and E_g should be determined by the energy position of the knee. Sometimes, as in the present case, a peak rather than a knee is observed due to electron-hole recombination at the surface which strongly reduces the SPV signal for $E < E_g$ [10]. The main peak can be related to the energy gap value E_g of the other compounds. Thus, at photon energies close to E_g , electron-hole pairs are generated in the near-surface layer and mainly recombine there through the available high density of surface states and thus the resulting SPV signal to decrease. At $h\nu > E_g$, the signal starts decreasing due to electron-hole recombination at the surface, and then it increases again to a maximum at 1.3 eV. The measured E_g in our experiments is in agreement with the reported values in [6]. The SPV spectrum normalized to its maximum value is reported in Figure 2. Grating A with 300 lines/ μm allowed higher energy (2.6 eV) in the spectrum to be measured. Now, the increased slope of the SPV signal represents the band gap energy at which the photon energies can excite the charge carriers and change the surface band bending. The excitation occurs after 2.7 eV and a sharp knee is seen until 3 eV. A linear slope extraction gives $E_g = 2.6 \text{ eV}$ relevant to a defect level in ZnO.

In Figure 2 at higher energies there are still some slopes at $E > 2.8 \text{ eV}$ which are bigger than the band gap of the device layers. These features are probably relevant to the transitions at the interface where the electrons from the conduction band in the CIGSe layer recombine with the holes at the valence band of CIGSe layer. In this work we could not observe a peak at 2.2 eV relevant to In_2S_3 layer which means that this layer was thin enough and transparent to the respective photons. Similarly, they related the peaks for energies above 2.8 eV to the Xe lamp used for illuminating the device. In some investigations with SPV techniques, such anomalies were attributed to the transitions from the defect levels to the subband gap levels of the adjacent layers [7]. They rather concluded that when the SPV spectrum, detected from illuminated CIGSe/ In_2S_3 , started to rise at photon energies above 1.2 eV the formation of the CIGSe/ In_2S_3 (Cl) interface was very influential on the separation of charge carriers photogenerated in the In_2S_3 layer. This effect concerns the existence of acceptor/donor levels in the respective n -type

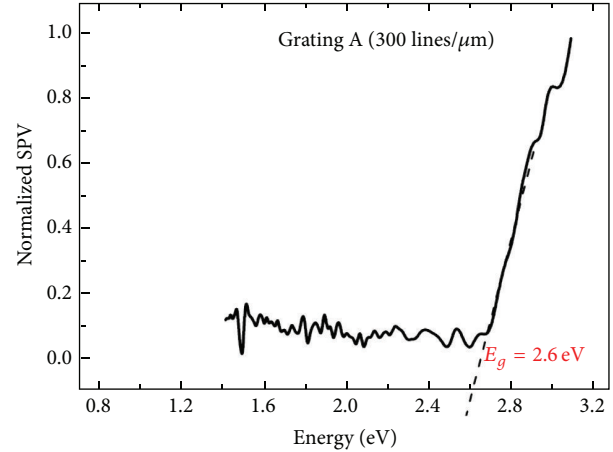


FIGURE 2: Normalized SPV spectrum versus photon energy impinging through grating A (300 lines/ μm).

and p -type layers. Such transitions are not far from the expectation because the treatment and postgrowth annealing induce many different defects, states, and complexes at both surface and bulk of the materials. Interface states play an essential role in the origin of the SPV signals. Their effect can be rather investigated by photoluminescence measurements [11]. The concentration of holes at each layer can have a similar effect localized at interface states. Since the SPV signal amplitude is related to the concentration of the excited carriers, one could expect the signal to be higher if the device goes under illumination. Thus the back surface could have bigger signals than the interface ones due to the lower recombination rate at the back surface. It is known that the recombination rate at the junction of a pn structure has the maximum rate. In order to obtain an insight into the source of defects and interdiffusion of the materials into the adjacent layers as well as the surface roughness and homogeneity of the film, the AFM analysis was performed on the same sample.

3.2. AFM Analysis. Dittrich et al. have applied the SPV technique to CIGSe thin film solar cells with two different CdS and In_2S_3 buffer layers [9]. They obtained higher SPV signals for the device with In_2S_3 . However, they reported that the deposition of ZnO can significantly change the amplitude of the SPV signal. They measured the SPV signal after ZnO deposition which was lower than the one detected for the cell with CdS. This observable change was attributed to the variation in the absorption range relevant to defect states with levels below the band gap of In_2S_3 ($E_g = 2.6 \text{ eV}$). Unfortunately, the morphology of the device was not performed to obtain a clearer idea about the distribution of defects through the film and/or the grain size and the boundary. Photoluminescence measurements or atomic force microscopy could be applied correspondingly.

Atomic force microscopy was used to map the surface morphology and phase inhomogeneities of the same device. The grading ratio of the In and Ga concentrations can spatially vary the surface energy due to differences in the chemical composition. Thus, a phase image can represent

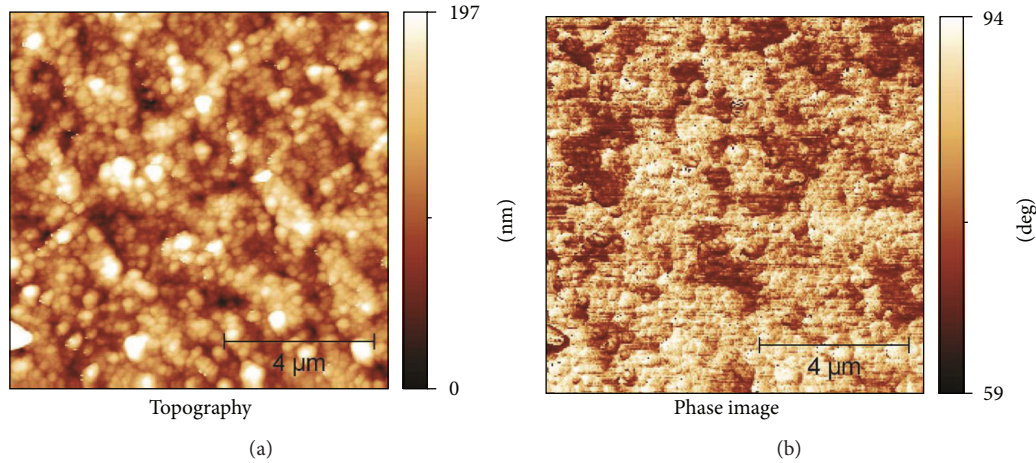


FIGURE 3: Topography and phase images of the CIGSe surface showing the roughness and grain size distribution.

the compositional surface inhomogeneity [11]. Figure 3 shows the topographic images obtained in AFM semicontact mode surface in the dark at low positive sample bias. The estimated average root mean square (rms) roughness is about 37.8 nm for a 400°C annealed film. The grains have almost uniform sizes of about 1 μm. The morphology shows the presence of granular grains typical of three-stage deposition and treatment solutions (CdCl₂ or deionized water) as white spots. Figure 3 displays also the phase image of the same area. The variation of grains and grain boundaries (GB) are due to differences in crystallographic orientation, contaminants, and film quality. The pixels in the two images have a corresponding relationship.

The surface height in dark red parts is 100 nm and in lighter ones is lower than 190 nm with 94-degree phase. The phase image is a signature of inhomogeneity in the composition of the sample surface; this image can be attributed to In segregation at surface defect states [8]. Indium would more likely segregate, as its surface diffusivity is higher than that of the other chemical components. The surface of the cell looks slightly rough (rms = 37.8 nm) but almost smooth with no cracks. This conclusion is attributed to the presence of an In₂S₃ buffer layer. Clearly the growth conditions (e.g., annealing) have a strong influence on the surface topography. The improvement in crystallinity occurs by the recrystallization of the layers under annealing at high temperature. Comparing the rms of the treated and as-deposited films, it can be deduced that the treated surface at 400°C is smoother than that of the as-deposited films annealed at 200°C. A smoother film reduces the light trapping at the surface and the number of interface states at CIGSe/In₂S₃. The films show (112) oriented peaks with slightly random orientation and the grain average size is about 1 μm. The three-stage process reduces the orientation of the nucleation but the grain sizes are smaller than those of the four-source elemental evaporation. Insertion of an In₂S₃ layer improved the surface roughness of the film comparing with the same sample and AFM results that are reported in [5]. Probably, the intermix of the layers from CIGSe to In₂S₃ or interdiffusion of Cu

into In₂S₃ (In₂S₃:Cu) and vice versa ceased due to this interface layer. Rather analyses are required to understand the interdiffusion and grain nucleation mechanism in thin films solar cells [12–14].

4. Summary

In summary, a graded band gap chalcopyrite CIGSe solar cell has been investigated by the surface photovoltage spectroscopy and atomic force microscopy. The band gap of a thin film solar cell based on CIGSe can be graded through a coevaporation stage. This is a conventional way to enhance light absorption as well as a better carrier extraction in a CIGSe solar cell. The band gap grading range is deduced by the extrapolation of the SPV signal slopes to the photon energy axis giving $E_g = 1.1\text{--}1.2/1.3$ eV which is acceptable for the In concentration against Ga of about 0.3. The ZnO shows a 2.6 eV band gap in agreement with the conventional reports on that. The SPV analysis can lead to understanding the effect of surface states and/or uncompensated defect states present in the CIGSe or ZnO layer as well as the interdiffusion of Cu into In₂S₃ layer. The photoluminescence measurements can also assist in understanding the levels of transition and the band gap grading induced by changes in the material components. However, the levels of subband gap transitions and defects can also be reviewed by the nondestructive SPV technique in room temperature. Such studies are extremely subject of debate among photovoltaic specialists and the effectiveness of any method to understand a specific phenomenon can be comparable and meaningful. The SPV signal observed at 1.3 eV is attributed to signature of In₂S₃:Cu which is formed because of the Cu diffusion from CIGSe into In₂S₃. Thus also the band gap of In₂S₃ is much smaller than 2 eV. The second SPV peak at 2.6 eV is attributed to metastabilities in CIGSe cells and could be also due to a defect level in ZnO. The AFM measurements yield information on the orientation of the atomic nucleation and material homogeneity. The grains are very oriented and the average size is almost uniform (less than 1 μm). The topography shows a uniform diffusion of

In_2S_3 or deionized water into the absorber layer after the treatment and annealing. The surface of the cell looks slightly rough (rms = 37.8 nm) but almost smooth with no cracks.

Conflict of Interests

The authors declare that there is no conflict of interests regarding the publication of this paper.

Acknowledgments

The authors thank Professor N. Barreau from the Université de Nantes, Nantes, France, for providing the sample. The authors highly appreciate Professor A. Cavallini, Dr. A. Minj, and S. Pandey from the Department of Physics, University of Bologna, Bologna, Italy, for their collaboration and valuable discussions. This work was partially funded by Intel Doctoral Student Honor Award, 2013.

References

- [1] S. Pandey, D. Cavalcoli, and A. Cavallini, "Band bowing and Si donor levels in InGaN layers investigated by surface photo voltage spectroscopy," *Applied Physics Letters*, vol. 102, no. 14, Article ID 142101, 2013.
- [2] N. E. Gorji, U. Reggiani, and L. Sandrolini, "Graded band gap CIGS solar cells considering the valence band widening," in *Proceedings of the 38th IEEE Photovoltaic Specialists Conference*, pp. 906–908, 2012.
- [3] L. Kronik, B. Mishori, E. Fefer, Y. Shapira, and W. Riedl, "Quality control and characterization of Cu(In,Ga)Se₂-based thin-film solar cells by surface photovoltage spectroscopy," *Solar Energy Materials and Solar Cells*, vol. 51, no. 1, pp. 21–34, 1998.
- [4] B. Fraboni, D. Cavalcoli, A. Cavallini, and P. Fochuk, "Electrical activity of deep traps in high resistivity CdTe: spectroscopic characterization," *Journal of Applied Physics*, vol. 105, no. 7, Article ID 073705, 2009.
- [5] Y.-K. Liao, S.-Y. Kuo, M.-Y. Hsieh et al., "A look into the origin of shunt leakage current of Cu(In,Ga)Se₂ solar cells via experimental and simulation methods," *Solar Energy Materials and Solar Cells*, vol. 117, pp. 145–151, 2013.
- [6] F. Jacob, N. Barreau, S. Gall, and J. Kessler, "Performance of CuIn_{1-x}Ga_xSe₂/(PVD)In₂S₃ solar cells versus gallium content," *Thin Solid Films*, vol. 515, no. 15, pp. 6028–6031, 2007.
- [7] S. Pandey, D. Cavalcoli, A. Minj et al., "Electronic transitions and fermi edge singularity in polar heterostructures studied by absorption and emission spectroscopy," *Journal of Applied Physics*, vol. 112, no. 12, Article ID 123721, 2012.
- [8] H. Mönig, Y. Smith, R. Caballero, C. Kaufmann, M. Lux-Steiner, and S. Sadewasser, "Direct evidence for a reduced density of deep level defects at grain boundaries of Cu(In,Ga)Se₂ thin films," *Physical Review Letters*, vol. 105, no. 11, Article ID 116802, 2010.
- [9] T. Dittrich, A. González, T. Rissom et al., "Comparative study of Cu(In,Ga)Se₂/CdS and Cu(In,Ga)Se₂/In₂S₃ systems by surface photovoltage techniques," *Thin Solid Films*, vol. 535, no. 1, pp. 357–361, 2013.
- [10] D. Cavalcoli, B. Fraboni, and A. Cavallini, "Surface photovoltage spectroscopy analyses of Cd_{1-x}Zn_xTe," *Journal of Applied Physics*, vol. 103, no. 4, Article ID 043713, 2008.
- [11] A. Darga, W. Favre, M. Fruzzetti et al., "Study of the electronic properties of wide band gap CIGSe solar cells: influence of copper off-stoichiometry," *Journal of Non-Crystalline Solids*, vol. 358, no. 17, pp. 2428–2430, 2012.
- [12] N. E. Gorji, U. Reggiani, and L. Sandrolini, "A simple model for the photocurrent density of a graded band gap CIGS thin film solar cell," *Solar Energy*, vol. 86, no. 3, pp. 920–925, 2012.
- [13] A. Minj, D. Cavalcoli, and A. Cavallini, "Investigation of the properties of In-related alloys by AFM," *Physica Status Solidi C*, vol. 9, no. 3-4, pp. 982–985, 2012.
- [14] A. Minj, D. Cavalcoli, and A. Cavallini, "Structural and local electrical properties of AlInN/AlN/GaN heterostructures," *Physica B: Condensed Matter*, vol. 407, no. 15, pp. 2838–2840, 2012.

Research Article

Graded Carrier Concentration Absorber Profile for High Efficiency CIGS Solar Cells

Antonino Parisi, Riccardo Pernice, Vincenzo Rocca, Luciano Curcio, Salvatore Stivala, Alfonso C. Cino, Giovanni Cipriani, Vincenzo Di Dio, Giuseppe Ricco Galluzzo, Rosario Miceli, and Alessandro C. Busacca

DEIM, University of Palermo, Viale delle Scienze, Building 9, 90128 Palermo, Italy

Correspondence should be addressed to Alessandro C. Busacca; alessandro.busacca@unipa.it

Received 28 November 2014; Revised 9 April 2015; Accepted 19 April 2015

Academic Editor: Cheuk-Lam Ho

Copyright © 2015 Antonino Parisi et al. This is an open access article distributed under the Creative Commons Attribution License, which permits unrestricted use, distribution, and reproduction in any medium, provided the original work is properly cited.

We demonstrate an innovative CIGS-based solar cells model with a graded doping concentration absorber profile, capable of achieving high efficiency values. In detail, we start with an in-depth discussion concerning the parametrical study of conventional CIGS solar cells structures. We have used the wxAMPS software in order to numerically simulate cell electrical behaviour. By means of simulations, we have studied the variation of relevant physical and chemical parameters—characteristic of such devices—with changing energy gap and doping density of the absorber layer. Our results show that, in uniform CIGS cell, the efficiency, the open circuit voltage, and short circuit current heavily depend on CIGS band gap. Our numerical analysis highlights that the band gap value of 1.40 eV is optimal, but both the presence of Molybdenum back contact and the high carrier recombination near the junction noticeably reduce the crucial electrical parameters. For the above-mentioned reasons, we have demonstrated that the efficiency obtained by conventional CIGS cells is lower if compared to the values reached by our proposed graded carrier concentration profile structures (up to 21%).

1. Introduction

Quaternary chalcopyrite semiconductor alloy $\text{Cu}(\text{In,Ga})\text{Se}_2$ (CIGS) represents one of the most suitable materials to produce low-cost and high-efficiency photovoltaic modules and hence can be considered as an appropriate alternative to the silicon technology. Recently, CIGS solar cells have gathered a noteworthy attention, since they possess a direct band gap falling within the range useful for several important applications, such as solid state lighting and high-efficiency photovoltaic modules [1]. Specifically, thin-film CIGS solar cells have emerged as a technology that could challenge the current dominance of silicon solar cells. This is possible thanks to the peculiar optical and structural properties of CIGS cells, which possess an extraordinary stability under a wide range of operating conditions. Nowadays, CIGS technology is industrially well exploited and commercial modules are broadly available.

In detail, this semiconductor presents a band gap tunable through the progressive Gallium incorporation, varying from

1.02 to 1.68 eV. Potentially, a wide band gap of the absorber designed to match the solar spectrum represents an effective way to increase the efficiency. Moreover, in this manner the open-circuit voltage (V_{OC}) can be increased, thus allowing to minimize the number of cells in series in the final assembled panel, and hence the interconnection losses.

In the literature, several research groups have demonstrated the realization of CIGS cells having conversion efficiencies of over 20%, quite similar to the value obtained by crystalline silicon cells, that is, around 25% [2]. A great deal of research is devoted to improve the performance, and this can only be achieved starting from a better understanding of the basic properties and of the common challenges that can limit the electrical parameters. For example, several papers in the literature reported on CIGS solar cells presenting lateral inhomogeneities on the μm scale that affect the main parameters, in particular the local splitting of quasi-Fermi levels obtained from photoluminescence measurements and thus decrease the overall performance [3]. Reducing or avoiding these problems is of great importance, since it is

worth noting that the direct conversion of sunlight into electricity, that is, photovoltaics, can be surely considered as a fundamental alternative to fossil fuels and could become, as experts say, “the biggest supplier of electricity by the end of the century” [4]. For this reason, over the last decades, many efforts have been made in this research field, in particular to accurately control the composition of deposited absorbers material. In addition, it is worth noting that the technological requirements to obtain reproducible and controllable compositions are in common with optical applications previously developed in different research environments [5–9].

Finally, it is worth mentioning that, from a broader perspective, interesting results can be expected from even more complex materials, for example, those based on pentanary $\text{Cu}(\text{In,Ga})(\text{S,Se})_2$ alloys [10] or comprising nanostructured layers/contacts [11]. For example, in [11], the authors have developed Al_2O_3 rear surface passivated CIGS solar cells with the local rear contacts consisting of Mo nanoparticles, in order to improve the optical confinement and hence to obtain an increased short circuit current density, if compared to CIGS solar cells with a standard back contact.

In literature, it has been reported that nonuniform Ga/In composition versus the absorber depth can improve the device performance [12]. The Ga fraction [i.e., $x = ([\text{Ga}]/([\text{Ga}] + [\text{In}]))$] influences the CIGS electron affinity, changing the value of E_c , while E_v is almost independent of x . [13]. The three most used typologies of grading are (i) linear front grading, in which the Ga fraction content increases in z (i.e., the depth) towards the junction; (ii) back grading, in which the increase is towards the back contact; (iii) *double* grading, in which the Ga first decreases from the front surface to a minimum position inside the absorber (i.e., in the centre of the structure) and then increases again towards the back contact [12]. The back grading causes the band gap of the absorber to linearly increase towards the back contact. Therefore, back grading creates an extra drift field for the minority electrons that improves the carrier collection and decreases bulk and surface recombination in the back contact interface. The V_{OC} of the cell is also augmented due to a lower recombination current (saturation current) [14]. However, a disadvantage consists in the Short-Circuit Current Density (J_{SC}) which does not efficiently exploit the solar spectrum. Instead, in a linear front grading, the gradual reduction of the Ga content through the absorber layer causes the band gap to linearly decrease with the depth. In this way, J_{SC} increases due to the augmented photon absorption for lower band gaps (i.e., thermalization losses are reduced). However, this increase can be negligible due to a concurrent reduced probability of the electron collection caused by the reverse quasioletrical field [14]. A double graded profile allows increased performance since the front grading improves the open-circuit voltage of the cell, while the back grading favours the collection of photo generated carriers, enhancing the photocurrent [12]. The maximum band gap at the back contact should be optimized to achieve the desired improved J_{SC} [14].

In this paper, we show a simulative analysis aimed at investigating the possible effects of both tailoring the absorber band gap and changing the carrier concentration

profile on the main electrical parameters of CIGS based solar cells, in order to design graded absorber profiles that are able to increase the efficiency. This has been performed to simulate structures suitable to be realized within an ongoing experimental activity. The technology of choice is single-step electrodeposition [15–18], which allows to finely adjust Ga content up to the found optimum band gap value of the CIGS absorber. During our simulations, performed using the wxAMPS software, we have first analysed five band gap values at varying absorber thickness, and then we have focused on a novel graded linear absorber profile, as will be illustrated in the following sections.

2. Numerical Modelling and Material Parameters

2.1. Numerical Analysis of CIGS Cells. CIGS polycrystalline solar cells are quite complex structures. This is due to the fact that they are composed of a large number of layers and, moreover, the effects of some phenomena, mechanisms or material parameters often cannot be directly derived from theoretical laws. Conversely, an empirical approach has to be followed. In order to understand and explain the results obtained through experimental measurements and, furthermore, try to solve the problems, numerical simulations have to be exploited. The latter are also carried out to clarify the potential advantages of a certain cell structure or the limits imposed by a specific technology. In particular, by means of simulations, it is possible to quantitatively describe the measurements carried out, thus providing an in-depth analysis of the physical behaviour of the cell. Moreover, it is possible to evaluate how the variation of some parameters of the used material influences the solar cell [19]. In fact, the variation of the considered properties in the ranges of acceptable values can strongly change the efficiency of the solar cell under study. By performing a parametric study, it is thus possible to determine the best values that optimize the efficiency, giving the experimental researcher some important information about fabrication methods to use, in order to improve device and product performances.

Several software solutions, such as Analysis of Microelectronic and Photonic Structures (AMPS-1D) [20], wxAMPS (Analysis of Microelectronic and Photonic Structure, wxWidgets provided) [21], Photovoltaic cell 1-Dimension (PC1D) [22], and Solar Cell Capacitance Simulator in 1 Dimension (SCAPS-1D) [23], have been developed to perform an in-depth simulation study of the functioning of multilayer structures, including those used for our thin film solar cells.

In this study, we have conducted our investigations extensively using wxAMPS, a freeware solar-cell simulation software. This program is an enhanced version, rewritten in C++ by Rockett et al. at the University of Illinois, of the previous AMPS-1D software, as developed by Fonash et al. at Pennsylvania State University [21, 24]. wxAMPS allows the simulation of optical and electronic behavior for multiple designs of solar cell devices. By means of this software, it is possible to easily design the solar cell structure and to properly select the input parameters. Subsequently, the computation of many parameters and characteristics, such

as J-V curves, fill-factor, efficiency, energy band diagrams, electric field, density carrier, generation, and recombination velocity, can be easily and automatically carried out.

wxAMPS versatility has also allowed us to investigate, in detail, the optical responses and the electrical transport phenomena of envisioned structures in our solar cells. A very large number of layers, with any kind of combination and composition can be engineered, to simulate the cross section of any feasible device. Sophisticated algorithms, such as the combination of the Gummel and Newton methods, are used in wxAMPS for the simulations. The advantages consist in an increased stability and a more consistent convergence in those instances in which intraband tunneling is critical to calculate specific solutions [25]. Finally, wxAMPS allows to setting, by means of a complete and user-friendly graphical interface, the environmental conditions and the physical properties of each layer. A good starting set of simulation parameters is provided by the University of Illinois, Engineering Wiki website [26], but it is also possible to freely customize the database by means of worksheets.

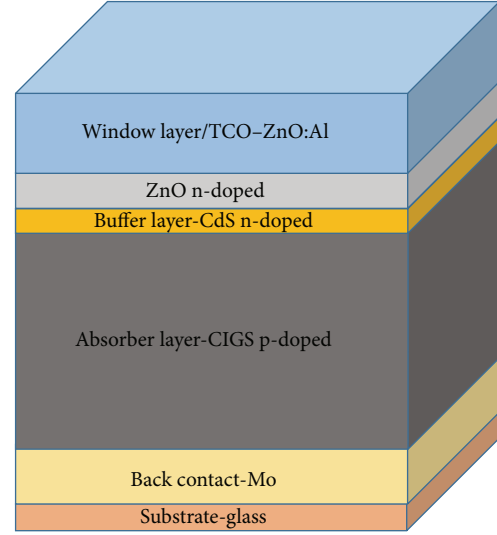
2.2. Stacked Structure. In this paper, we refer to a solar cell of the type ZnO:Al/ZnO/CdS/CIGS/Mo/substrate, as sketched in Figure 1(a).

The most important layer of the abovementioned photovoltaic cell is the CIGS absorber. In our work, we have first considered a single absorber layer with constant properties (i.e., doping concentrations, energy gap, etc.), as in *conventional* CIGS solar cells. Afterwards, we have taken into account a newly proposed absorber structure (Figure 1(b)), consisting of several different layers having each one a different doping concentration (N_A). In detail, we have considered a linearly increasing doping concentration profile, with the maximum value of N_A in the layer located near the absorber-Molibdenum interface.

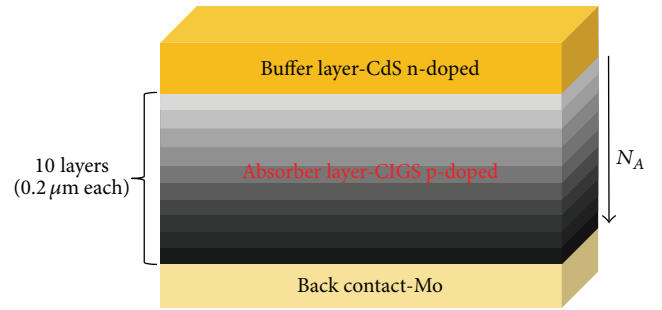
With regard to the CdS buffer layer, it is known that CdS is a direct band gap semiconductor (band-gap = 2.4 eV) and its use as a buffer layer improves the performance of the solar cell, since it provides a lower interface recombination, the prevention of undesirable shunt paths through the absorber and less structural damage due to the subsequent deposition of ZnO onto CIGS. Moreover, CdS layer also reduces reflection losses at the cell surface, since its refractive index falls between those of ZnO and CIGS.

As evident in Figure 1(a) a p-n junction is formed by the ZnO-CdS (n-type material) with p-type CIGS. The thickness of CdS is usually chosen within the 50–100 nm range, since this value represents the best compromise between the abovementioned advantages and losses due to optical absorption. On the top of the buffer layer, an n-doped ZnO and an aluminium-doped ZnO (ZnO:Al) layers are deposited.

These two layers form the so-called transparent conductive oxide (TCO), since they both possess a wider band-gap, so being transparent to most of the solar spectrum. The most important layer in the photovoltaic cell is the absorber one, represented by the CIGS layer. $\text{Cu}(\text{In,Ga})\text{Se}_2$ is a semiconductor compound exhibiting a chalcopyrite crystal structure and possessing a high absorption coefficient ($\alpha \sim 10^5 \text{ cm}^{-1}$) [27].



(a)



(b)

FIGURE 1: (a) Structure of CIGS-based solar cells (drawing not to scale); (b) graded absorber profile structure.

TABLE 1: Simulation material parameters of the CIGS thin-film solar cell.

Parameter	ZnO:Al	ZnO	CdS	CIGS
d (μm)	0.2	0.2	0.05	Variable
ϵ_R	9	9	10	13.6
E_g (eV)	3.3	3.3	2.4	Variable
χ (eV)	4.4	4.4	4.2	Variable
N_C [cm^{-3}]	2.2×10^{18}	2.2×10^{18}	2.2×10^{18}	2.2×10^{18}
N_V [cm^{-3}]	1.8×10^{19}	1.8×10^{19}	1.8×10^{19}	1.8×10^{19}
μ_n [$\text{cm}^2/(\text{V}\cdot\text{s})$]	100	100	100	Variable
μ_p [$\text{cm}^2/(\text{V}\cdot\text{s})$]	25	25	25	Variable
N_D [cm^{-3}]	1×10^{20}	Variable	Variable	0
N_A [cm^{-3}]	0	0	0	Variable

Simulation of the device has been performed by setting, for each layer, the optical and electrical parameters in Table 1, as reported in literature [28–30].

We have analysed different band-gap values, with the corresponding absorption spectra taken from Paulson et al. [19]. The band gap of the absorber surges from 1.04 eV (pure CIS)

TABLE 2: Simulation material Gaussian defect for the CIGS solar layers.

Parameter	ZnO:Al	ZnO	CdS	CIGS
Defect type	Donor	Donor	Acceptor	Donor
Energy level [eV]	1.65	1.65	1.2	0.6
Deviation [eV]	0.1	0.1	0.1	0.1
σ_n [cm ²]	1×10^{-12}	1×10^{-12}	1×10^{-17}	5×10^{-13}
σ_p [cm ²]	1×10^{-15}	1×10^{-15}	1×10^{-12}	1×10^{-15}
N_t [cm ⁻³]	1×10^{17}	1×10^{17}	1×10^{18}	1×10^{14}

TABLE 3: Contact parameters applied in the simulations.

Parameter	Back contact	Front contact
Φ_B [eV]	Variable	0
S_n [cm/s]	2×10^7	1×10^7
S_p [cm/s]	2×10^7	1×10^7
Reflectivity	0.8	0.05

TABLE 4: Explanation of the parameters used during the simulations.

Parameter	Explanation
D	Layer thickness
ϵ_R	Permittivity constant
χ	Electron affinity
N_C/N_V	Effective density of states in the conduction/valence band
μ_n/μ_p	Mobility of electrons/holes
σ_n/σ_p	Capture cross section of electrons/holes
N_D/N_A	Doping concentration
N_t	Defect concentration
Φ_B	Potential barrier height
S_n/S_p	Surface recombination velocity of electrons/holes

to 1.69 eV (pure CGS) according to the following relationship [31]:

$$E_g(x) = 1.02 + 0.67x + 0.24x(x - 1), \quad (1)$$

where x is the Ga fraction in the absorber layer.

Tables 2 and 3 summarize material Gaussian defect states and contact parameters, respectively, while Table 4 provides an explanation of the symbols used in the previous tables. Finally, front and back contacts are defined by means of the corresponding metal work function. Numerical simulations have been performed by using the standard AM1.5G solar spectrum, a reflection coefficient on the top of the cell equal to 5% and a cell temperature of 300 K.

It is worth noting that a stable and not considerably rectifying back-contact is needed in a CIGS solar cell to obtain good performance and stability. For this reason, the development of a low barrier back-contact and, hence, a low contact resistance is an ongoing challenge in the fabrication of high performance CIGS based solar cells.

In general, metal-to-semiconductor contacts can act either as a rectifying (Schottky) or as an ohmic contact, according to the properties of the interface. In detail, in the case of a p-type semiconductor having a band-gap E_g , electron affinity χ , and a metal with work function Φ_m , an ohmic metal/semiconductor contact is obtained when

$$\Phi_m > E_g + \chi. \quad (2)$$

On the other hand, a rectifying contact is formed when the following relationship occurs:

$$\Phi_m < E_g + \chi. \quad (3)$$

At the Schottky-contact interface, majority carriers (holes) see a barrier Φ_B , as they travel from the semiconductor towards the metal, but such a barrier is not present in the case of an ohmic contact interface.

Most metals, however, do not have sufficiently high work functions and therefore form Schottky-barrier contacts: this is indeed the case for the p-CIGS absorber layers/Molybdenum interface.

In the case of an ideal contact between a metal and a p-type semiconductor, and in the absence of surface states, it is possible to express the contact barrier height for holes as follows [32]:

$$\Phi_B = E_g + \chi - \Phi_m. \quad (4)$$

For the simulations that we have carried out, at varying E_g we have assumed $E_g + \chi$ constant and equal to 5.55 eV [33], and also Φ_m (Mo) = 4.95 eV [34], obtaining $\Phi_B = 0.6$ eV. In other words, our simulations were performed keeping the back-contact barrier Φ_B constant.

3. Results and Discussion

CIGS photovoltaic cells are typically composed of a Cu(In,Ga)Se₂ layer having a thickness of about $2 \div 3 \mu\text{m}$. Decreasing such a thickness without reducing the performance too much would allow to cutting the deposition time of the CIGS thin-film and thus a considerable saving of the raw materials employed, with a substantial decrease of production costs. Moreover, decreasing the usage of Indium and Gallium during the mass production of CIGS solar cells would surely have positive ecological and environmental impacts. Nonetheless, there are some drawbacks caused by the reduction of the absorber layer thickness, reported in detail in [35–37].

By means of the aforementioned software, we have first performed some simulative campaigns of conventional CIGS cells (herein called Uniform Carrier Concentration Profile, UCCP). The simulations have been carried out at several different energy gap values, keeping constant the properties of the different layers while changing the absorber thickness, as shown in Figure 2. In this manner, it has been possible to investigate on the effect of the absorber layer thickness on the electrical parameters of the solar cell.

As reported in Figure 2, with a thickness greater than $2 \mu\text{m}$, the solar cell absorbs most of the useful solar spectrum

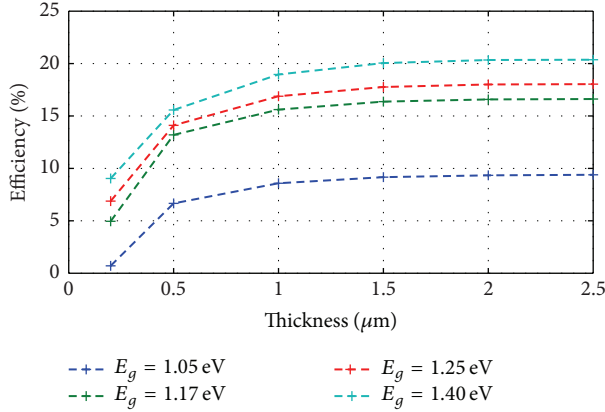


FIGURE 2: Efficiency versus CIGS absorber thickness at varying absorber energy gap values.

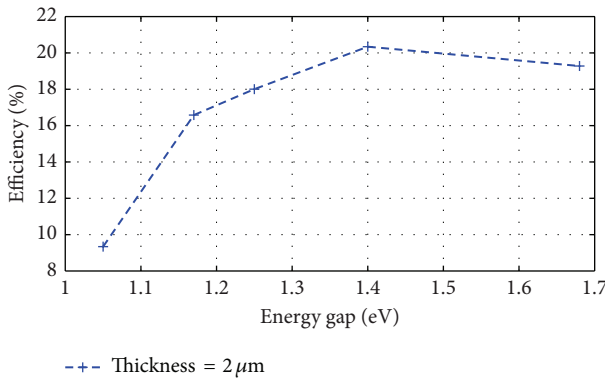


FIGURE 3: Efficiency of solar cell versus CIGS energy gap for a 2 μm thick absorber layer.

which it is sensitive to and, thus, the efficiency is practically constant. In particular, we were able to obtain a value higher than 95% of the maximum efficiency possible when the absorber thickness is greater than 1 μm , regardless of the energy gap, that is, irrespective of the fraction of Ga in the CIGS.

In Figure 3 the efficiency versus energy gap curve is shown, going from a pure CIS composition ($E_g = 1.02$ eV) to a CGS ($E_g = 1.68$ eV), for a 3 μm thick absorber layer. As reported, the absolute maximum efficiency is obtained for an energy gap value (E_g) of about 1.4 eV, which corresponds to a Ga/(Ga + In) ratio of 0.66.

A similar behavior is observed for other thickness values, not reported here for brevity, and thus this trend happens regardless of the absorber thickness. Similarly, the maximum fill factor (FF), around 75%, is obtained again for an $E_g = 1.4$ eV.

Figure 4 depicts the variation of both J_{SC} and V_{OC} when increasing the energy gap from 1.02 to 1.68 eV. The obtained results show that, in the range under investigation, J_{SC} decreases almost linearly whereas the V_{OC} increases.

By using this simple structure of conventional CIGS cells, it is possible to achieve a good efficiency only for high values

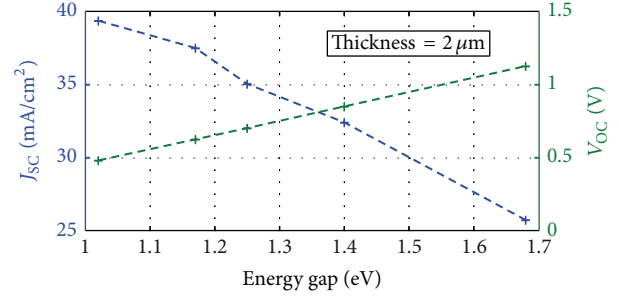


FIGURE 4: Short-circuit current density J_{SC} and open-circuit voltage V_{OC} versus CIGS energy gap for a 2 μm thick absorber layer.

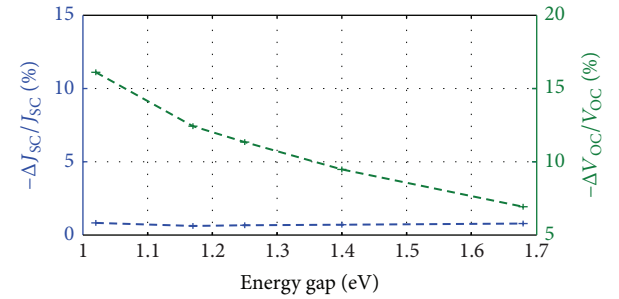


FIGURE 5: Relative variation of the short-circuit current density J_{SC} and the open-circuit voltage V_{OC} versus CIGS energy gap when employing the Mo back-contact.

of energy gap, as expected. However, augmenting the E_g gap is not the ideal technological solution, since it causes an increased defect density in the areas presenting high Ga content [38]. Therefore, this high efficiency reported in the simulations cannot be achieved in a real device.

In addition, another reason that can reduce the performance in real devices consists in the presence of the back contact barrier at CIGS/Mo interface. In order to quantify this effect, we have performed some additional measurement campaigns comparing the device performances in the presence both of a real back-contact (i.e., Molybdenum) and an ideal back-contact. The ideal interface has been simulated with a surface recombination speed equal to the carrier thermal velocity and a barrier height equal to zero. The results are shown in Figures 5 and 6. In detail, Figure 5 depicts the relative variation of the short-circuit current density J_{SC} and the open-circuit voltage V_{OC} —at increasing energy gap—when employing the real back-contact. The reference values (J_{SC} and V_{OC}) refers to the case with the Mo back-contact. Similarly, Figure 6 illustrates the variation of the efficiency and the fill factor. The results indicate that the open-circuit voltage decreases of about 7% at higher E_g values, while the difference is even more pronounced for lower E_g values (up to 16%). With regard to the short circuit current, there are no noticeable differences for the whole range of considered energy gaps. The fill factor decreases of just 2% at higher energy gaps, while the difference is more noticeable for lower E_g absorbers (about 9%). The same trend can be observed for the efficiency: for absorbers with lower energy gaps the Mo

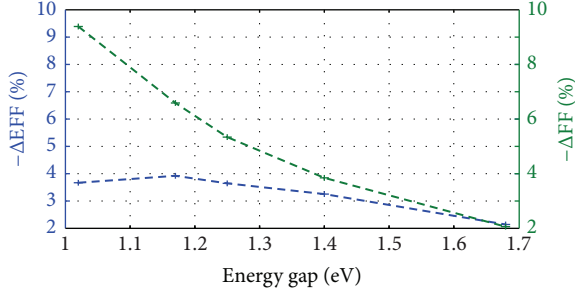


FIGURE 6: Variation of the efficiency and the fill factor versus CIGS energy gap when employing the Mo back-contact.

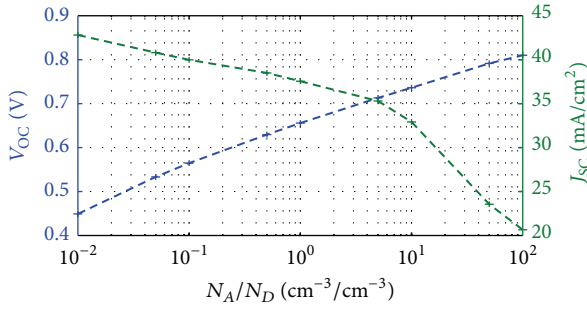


FIGURE 7: Open-circuit voltage and short circuit density versus the ratio between the N_A concentration and the donors concentration N_D , for a given fixed value of $N_D = 10^{17} \text{ cm}^{-3}$.

real back-contact causes a decrease in efficiency of about 4%, whereas this effect is less noticeable at increasing E_g .

From the above-mentioned results, it is clear that it would be convenient to use high energy gap absorbers, but this would cause an increase of density defects when augmenting the Ga content, as already before-mentioned. In order to overcome this limitation, in the literature other kinds of cells have been realized [39] having a variable absorber composition with an increased energy gap only in the area near the Mo back-contact. In particular, the above-mentioned cells possess, in the CIGS layer, a Ga fraction increasing from about 0.3 ($E_g \sim 1.2 \text{ eV}$) near the junction up to 0.5 ($E_g \sim 1.4 \text{ eV}$) near the Mo contact. In this way, it is possible to reach an efficiency slightly higher than 20%.

In order to reduce the overall effect of the Molybdenum back-contact, acceptor doping concentration of absorber CIGS layer N_A must be augmented. For this reason, in the literature [40], high efficiency cells have been recently obtained through an accurate control of the doping concentration of the absorber during its growth.

Figure 7 shows both the V_{OC} and the J_{SC} versus the ratio between the N_A concentration and the donors concentration N_D , for a given fixed value of $N_D = 10^{17} \text{ cm}^{-3}$. As reported, V_{OC} increases with N_A , while J_{SC} decreases due to an increased recombination rate near the space charge region (SCR). Similar trends have been obtained for N_D in the range between 10^{15} and 10^{18} cm^{-3} and are not reported here for brevity.

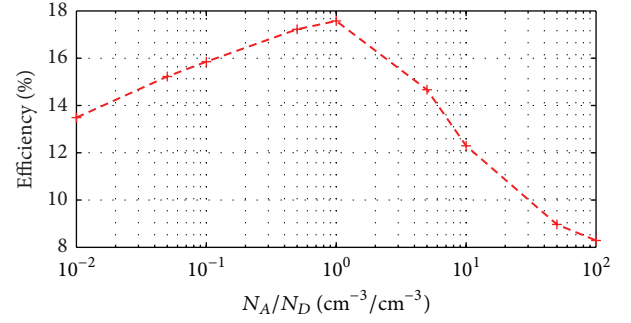


FIGURE 8: Efficiency versus the ratio between the N_A concentration and the donors concentration N_D for a given fixed value of $N_D = 10^{17} \text{ cm}^{-3}$.

As a consequence, the efficiency has a maximum value, as reported in Figure 8 that depicts the efficiency versus the ratio between the N_A concentration and the donors concentration N_D .

In detail, the maximum is obtained when N_D is almost equal to N_A . Also in this case, similar trends have been obtained for other values of N_D in the range between 10^{15} and 10^{18} cm^{-3} .

In order to improve both V_{OC} and J_{SC} , we propose the innovative structure having a graded carrier concentration absorber profile, already described in Section 2.2 and herein called Graded Carrier Concentration Profile, GCCP.

In other words, we have simulated a CIGS solar cell with the absorber consisting of 10 different $0.2 \mu\text{m}$ -thick layers each one having a different doping concentration (N_A). The overall CIGS absorber thickness (i.e., $2 \mu\text{m}$) has been chosen to make it an easy comparison possible with the above-analysed conventional cell.

In detail, the doping concentration in the absorber is supposed to linearly increase towards the back contact, with the maximum value of N_A in the layer located near the absorber-Molybdenum interface. In our simulations, the minimum value of N_A is supposed to be in the layer near the junction ($N_{A,LJ}$) and varies from 10^{14} cm^{-3} to 10^{19} cm^{-3} , while the maximum value of N_A is in the layer placed near the absorber-Molybdenum interface ($N_{A,Mo}$) and it is assumed constant to $N_{A,Mo} = 10^{19} \text{ cm}^{-3}$. This upper bound has been chosen since it is very difficult, from a technological point of view, to realize higher N_A concentrations. In addition, we want to underline that we will focus on an absorber having a Ga fraction equal to 0.31, which can be easily realized with a better quality, contrarily to absorbers with higher Ga content.

In order to reveal more information on the working principle of such structures, we have first carried out a depth-dependent investigation of our CIGS cells. In particular, in Figure 9, we depict the energy-band diagram versus depth for a GCCP cell, with $N_D = N_{A,LJ} = 10^{17} \text{ cm}^{-3}$, compared to a conventional uniform CIGS absorber profile, with $N_D = N_A = 10^{17} \text{ cm}^{-3}$. As reported, the GCCP structure causes the energy band of the absorber to linearly increase towards the back contact.

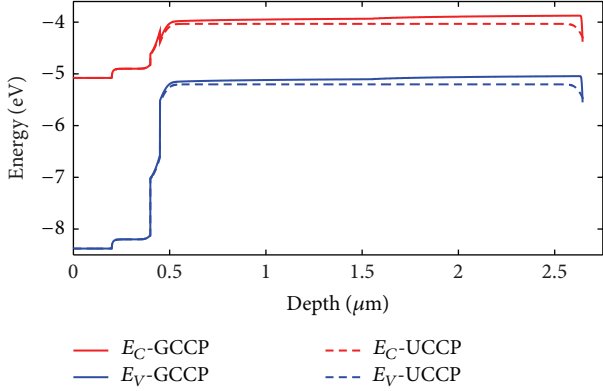


FIGURE 9: The schematic energy-band diagram versus depth of a GCCP ($N_D = N_{A,LJ} = 10^{17} \text{ cm}^{-3}$) and UCCP ZnO:Al/ZnO/CdS/CIGS/Mo solar cell under standard AM1.5G solar spectrum condition.

Therefore, similarly to what happens inside a CIGS cell having a Ga back graded profile, a quasioelectrical field directed towards the back-contact is induced through the absorber. For the case shown in Figure 9 the value of the generated quasioelectrical field is about 600 V/cm. This field causes the drift of the photogenerated electrons and of the holes, the first towards the SCR and the latter towards the back-contact, respectively. Therefore, the minority-carrier “drift-diffusion length” is increased, and thus an efficient collection of the carrier at the junction can be achieved in GCCP CIGS cells. This effect reduces both bulk and back surface recombination at the contact, and thus J_{SC} , V_{OC} , FF, and the efficiency are enhanced.

However, an important difference compared to Ga back graded profile consists in the fact that in our structure both E_C and E_V increase towards the back-contact, and thus the energy gap keeps constant along the absorber depth. Thanks to this behaviour, the generation process is more efficient in the proposed cells if compared to Ga back-graded structures that present higher thermalization losses.

As depicted in Figure 10, due to the above-mentioned quasioelectrical field, the minority carrier current direction changes just before the back-contact in a GCCP cell, when the back surface field at the CIGS/Mo interface becomes dominant. Instead, in an UCCP cell this change happens near the junction, and thus all the carriers photogenerated deeper inside the absorber contribute to reduce the cell performances. Hence, in our proposed GCCP solar cell the total current density increases compared to a conventional cell.

Using the above-mentioned GCCP structure, we have performed several simulation campaigns aimed at analysing how the main parameters (i.e., efficiency, short circuit current, and open circuit voltage) are improved if compared to the conventional structure.

The results are depicted in Figure 11, in which we show the efficiency versus the $N_{A,LJ}/N_D$ ratio. In detail, $N_{A,LJ}$ is the concentration near the junction, while N_D is the donors concentration of the two n-type junction layers (i.e., CdS and

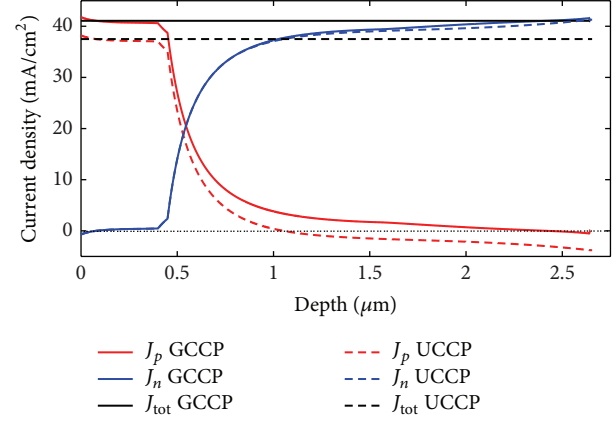


FIGURE 10: Current density versus depth of a GCCP ($N_D = N_{A,LJ} = 10^{17} \text{ cm}^{-3}$) and UCCP ZnO/CdS/CIGS solar cell under standard AM1.5G solar spectrum condition.

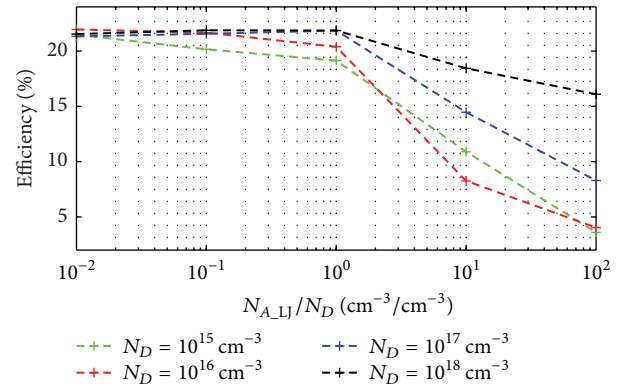


FIGURE 11: Efficiency versus the ratio between the N_A concentration near the junction and the donors concentration N_D at several different values of N_D .

ZnO) composing the structure. Several different N_D values were taken into account, ranging from 10^{15} cm^{-3} to 10^{18} cm^{-3} .

As reported, by using the proposed cell structure and properly choosing the value of N_A near the junction, it is possible to achieve high efficiency (up to about 22%), regardless of the N_D concentration. Comparing these values with the conventional CIGS structure, see Figure 3 at the corresponding $E_g = 1.2 \text{ eV}$, a strong surge in efficiency (more than 4%) can be observed. It is worth noting that this is true only if we have an N_A near the junction less or equal to the N_D concentration (i.e., $N_{A,LJ} \leq N_D$); otherwise, the efficiency noticeably decreases due to the already mentioned photo carrier recombination effect close to the junction, which decreases the J_{SC} , as reported in Figure 12. A similar trend is observed for the fill factor, not reported here for brevity.

Lastly, Figure 13 shows the V_{OC} versus $N_{A,LJ}/N_D$ ratio, for N_D in the range between 10^{15} and 10^{18} cm^{-3} . As reported, the V_{OC} increases with the doping concentration.

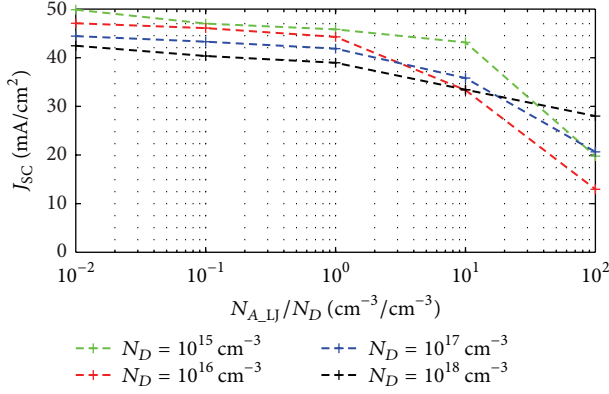


FIGURE 12: J_{SC} versus the ratio between the N_A concentration near the junction and the donors concentration N_D at several different values of N_D .

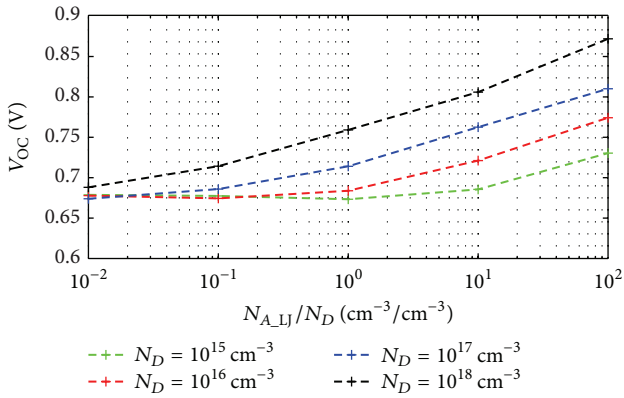


FIGURE 13: V_{OC} versus the ratio between the N_A concentration near the junction and the donors concentration N_D at several different values of N_D .

4. Conclusions

In this study, we have performed some simulative campaigns by means of the wxAMPS software, to investigate on the effects of the absorber band gap on the main electrical parameters in conventional CIGS solar cells. In detail, our results show that the efficiency increases with energy gap, up to a maximum peak around 1.40 eV. In addition, the Ga content also influences V_{OC} e J_{SC} : in detail, V_{OC} increases linearly with E_g , while J_{SC} decreases considerably. Furthermore, we have shown that all the electrical parameters remain almost constant when the absorber thickness is greater than $2 \mu\text{m}$. Moreover, we have investigated on the effects of the molybdenum back-contact on the above-mentioned parameters, showing a decrease in efficiency of about 3–5% in presence of the back-contact, especially at lower values of Ga content.

However, the obtained efficiency is quite lower if compared to other kinds of cell already reported in the literature. For this reason, we have proposed a novel structure with a graded doping concentration absorber profile. A depth-dependent investigation has shown that, in GCCP structures, a quasioletrical field directed towards the back-contact is

induced through the absorber, E_C and E_V increase towards the back-contact, and thus the energy gap keeps constant along the depth. Therefore, the generation process is more efficient in GCCP cells compared to Ga back-graded structures. Close to the Mo back contact, the N_A concentration should be the highest technologically feasible, while the N_A concentration near the junction should be lower than N_D to avoid an excessive photo carrier recombination effect. In this way, we were able to increase the efficiency up to over 21%.

These results are of great importance to allow technological optimization during future experimental work.

Conflict of Interests

The authors declare that there is no conflict of interests regarding the publication of this paper.

Acknowledgments

This activity was supported by PON 01 1725 “Nuove Tecnologie Fotovoltaiche per Sistemi Intelligenti Integrati in Edifici” and PON 02 00355 “Tecnologie per l’ENERGIA e l’Efficienza enERGETICa—ENERGETIC” Research Programs. Contributions came also from SDESLab, University of Palermo.

References

- [1] T. Unold and C. A. Kaufmann, “1.18. Chalcopyrite thin-film materials and solar cells,” in *Comprehensive Renewable Energy*, E.-C. A. Sayigh, Ed., pp. 399–422, Elsevier, Oxford, UK, 2012.
- [2] V. S. Saji, I.-H. Choi, and C.-W. Lee, “Progress in electrodeposited absorber layer for $\text{CuIn}_{(1-x)}\text{Ga}_x\text{Se}_2$ (CIGS) solar cells,” *Solar Energy*, vol. 85, no. 11, pp. 2666–2678, 2011.
- [3] W. Witte, M. Powalla, D. Hariskos et al., “Chemical gradients in $\text{Cu}(\text{In,Ga})(\text{S,Se})_2$ thin-film solar cells: results of the GRACIS project,” in *Proceedings of the 27th European Photovoltaic Solar Energy Conference and Exhibition*, pp. 2166–2173, Frankfurt, Germany, 2012.
- [4] “Achievements and challenges of solar electricity from photovoltaics,” in *Handbook of Photovoltaic Science and Engineering*, A. Luque and S. Hegedus, Eds., John Wiley & Sons, 2nd edition, 2011.
- [5] A. Tomasino, A. Parisi, S. Stivala et al., “Wideband THz time domain spectroscopy based on optical rectification and electro-optic sampling,” *Scientific Reports*, vol. 3, article 3116, pp. 1–8, 2013.
- [6] A. Pasquazi, A. Busacca, S. Stivala, R. Morandotti, and G. Assanto, “Nonlinear disorder mapping through three-wave mixing,” *IEEE Photonics Journal*, vol. 2, no. 1, pp. 18–28, 2010.
- [7] A. Parisi, A. C. Cino, A. C. Busacca, M. Cherchi, and S. Riva-Sanseverino, “Integrated optic surface plasmon resonance measurements in a borosilicate glass substrate,” *Sensors*, vol. 8, no. 11, pp. 7113–7124, 2008.
- [8] R. Pernice, G. Adamo, S. Stivala et al., “Opals infiltrated with a stimuli-responsive hydrogel for ethanol vapor sensing,” *Optical Materials Express*, vol. 3, no. 11, pp. 1820–1833, 2013.
- [9] M. Cherchi, S. Bivona, A. C. Cino, A. C. Busacca, and R. L. Oliveri, “Universal charts for optical difference frequency generation in the terahertz domain,” *IEEE Journal of Quantum Electronics*, vol. 46, no. 6, pp. 1009–1013, 2010.

- [10] Y. Goushi, H. Hakuma, K. Tabuchi, S. Kijima, and K. Kushiya, "Fabrication of pentanary Cu(InGa)(SeS)₂ absorbers by selenization and sulfurization," *Solar Energy Materials and Solar Cells*, vol. 93, no. 8, pp. 1318–1320, 2009.
- [11] B. B. Vermang, J. T. Wätjen, V. Fjällström et al., "Highly reflective rear surface passivation design for ultra-thin Cu(In,Ga)Se₂ solar cells," *Thin Solid Films*, vol. 582, pp. 300–303, 2015.
- [12] M. Gloeckler and J. R. Sites, "Band-gap grading in Cu(In,Ga)Se₂ solar cells," *Journal of Physics and Chemistry of Solids*, vol. 66, no. 11, pp. 1891–1894, 2005.
- [13] N. E. Gorji, M. D. Perez, U. Reggiani, and L. Sandrolini, "A new approach to valence and conduction band grading in CIGS thin film solar cells," *International Journal of Engineering and Technology*, vol. 4, no. 5, pp. 573–576, 2012.
- [14] J. Mattheis, P. J. Rostan, U. Rau, and J. H. Werner, "Carrier collection in Cu(In,Ga)Se₂ solar cells with graded band gaps and transparent ZnO:Al back contacts," *Solar Energy Materials and Solar Cells*, vol. 91, no. 8, pp. 689–695, 2007.
- [15] R. Inguanta, S. Piazza, C. Sunseri et al., "An electrochemical route towards the fabrication of nanostructured semiconductor solar cells," in *Proceedings of the International Symposium on Power Electronics, Electrical Drives, Automation and Motion (SPEEDAM '10)*, pp. 1166–1171, IEEE, June 2010.
- [16] A. Parisi, L. Curcio, V. Rocca et al., "Thin film CIGS solar cells, photovoltaic modules, and the problems of modeling," *International Journal of Photoenergy*, vol. 2013, Article ID 817424, 12 pages, 2013.
- [17] A. C. Busacca, V. Rocca, L. Curcio et al., "Parametrical study of multilayer structures for CIGS solar cells," in *Proceedings of the International Conference on Renewable Energy Research and Application (ICRERA '14)*, pp. 964–968, Milwaukee, Wis, USA, October 2014.
- [18] G. Cipriani, V. Di Dio, R. Miceli et al., "CIGS PV module characteristic curves under chemical composition and thickness variations," in *Proceedings of the International Conference on Renewable Energy Research and Applications (ICRERA '14)*, pp. 969–973, Milwaukee, Wis, USA, October 2014.
- [19] P. D. Paulson, R. W. Birkmire, and W. N. Shafarman, "Optical characterization of CuIn_{1-x}Ga_xSe₂ alloy thin films by spectroscopic ellipsometry," *Journal of Applied Physics*, vol. 94, no. 2, pp. 879–888, 2003.
- [20] N. Hernández-Como and A. Morales-Acevedo, "Simulation of hetero-junction silicon solar cells with AMPS-1D," *Solar Energy Materials and Solar Cells*, vol. 94, no. 1, pp. 62–67, 2010.
- [21] H. Zhu, A. K. Kalkan, J. Hou, and S. J. Fonash, "Applications of AMPS-1D for solar cell simulation," *AIP Conference Proceedings*, vol. 462, pp. 309–314, 1999.
- [22] P. A. Basore and D. A. Clugston, "PC1D version 4 for windows: from analysis to design," in *Proceedings of the 25th IEEE Photovoltaic Specialists Conference*, pp. 377–381, May 1996.
- [23] S. Degraeve, M. Burgelman, and P. Nollet, "Modelling of polycrystalline thin film solar cells: new features in scaps version 2.3," in *Proceedings of the 3rd World Conference on Photovoltaic Energy Conversion*, pp. 487–490, IEEE, Osaka, Japan, May 2003.
- [24] S. Fonash, J. Arch, J. Cuifi et al., *A Manual for AMPS-1D for Windows 95/NT*, Pennsylvania State University, State College, Pa, USA, 1997.
- [25] Y. Liu, Y. Sun, and A. Rockett, "An improved algorithm for solving equations for intra-band tunneling current in hetero-junction solar cells," *Thin Solid Films*, vol. 520, no. 15, pp. 4947–4950, 2012.
- [26] <https://wiki.engr.illinois.edu/display/solarcellsim>.
- [27] B. J. Stanbery, "Copper indium selenides and related materials for photovoltaic devices," *Critical Reviews in Solid State and Materials Sciences*, vol. 27, no. 2, pp. 73–117, 2002.
- [28] Z. Jehl, F. Erfurth, N. Naghavi et al., "Thinning of CIGS solar cells: part II: cell characterizations," *Thin Solid Films*, vol. 519, no. 21, pp. 7212–7215, 2011.
- [29] A. Niemegeers, S. Gillis, and M. Burgelman, "A user program for realistic simulation of polycrystalline heterojunction solar cells: SCAPS-1D," in *Proceedings of the 2nd World Conference on Photovoltaic Energy Conversion*, Wien, Austria, July 1998.
- [30] R. Scheer, "Towards an electronic model for CuIn_{1-x}Ga_xSe₂ solar cells," *Thin Solid Films*, vol. 519, no. 21, pp. 7472–7475, 2011.
- [31] O. Lundberg, M. Edoff, and L. Stolt, "The effect of Ga-grading in CIGS thin film solar cells," *Thin Solid Films*, vol. 480–481, pp. 520–525, 2005.
- [32] S. M. Sze, *Physics of Semiconductor Devices*, Wiley, 2nd edition, 1981.
- [33] Y. Hirai, Y. Kurokawa, and A. Yamada, "Numerical study of Cu(In,Ga)Se₂ solar cell performance toward 23% conversion efficiency," *Japanese Journal of Applied Physics*, vol. 53, no. 1, Article ID 012301, 2014.
- [34] P. Ranade, H. Takeuchi, T.-J. King, and C. Hu, "Work function engineering of molybdenum gate electrodes by nitrogen implantation," *Electrochemical and Solid-State Letters*, vol. 4, no. 11, pp. G85–G87, 2001.
- [35] M. Gloeckler, A. L. Fahrenbruch, and J. R. Sites, "Numerical modeling of CIGS and CdTe solar cells: setting the baseline," in *Proceedings of the 3rd World Conference on Photovoltaic Energy Conversion*, vol. 1, pp. 491–494, IEEE, Osaka, Japan, May 2003.
- [36] P. Jackson, D. Hariskos, E. Lotter et al., "New world record efficiency for Cu(In,Ga)Se₂ thin-film solar cells beyond 20%," *Progress in Photovoltaics: Research and Applications*, vol. 19, no. 7, pp. 894–897, 2011.
- [37] M. Gloeckler and J. R. Sites, "Potential of submicrometer thickness Cu (In,Ga) Se₂ solar cells," *Journal of Applied Physics*, vol. 98, Article ID 103703, 2005.
- [38] G. Hanna, A. Jasenek, U. Rau, and H. W. Schock, "Influence of the Ga-content on the bulk defect densities of Cu(In,Ga)Se₂," *Thin Solid Films*, vol. 387, no. 1-2, pp. 71–73, 2001.
- [39] C. L. Perkins, B. Egaas, I. Repins, and B. To, "Quantitative analysis of graded Cu(In_{1-x}Ga_x)Se₂ thin films by AES, ICP-OES, and EPMA," *Applied Surface Science*, vol. 257, no. 3, pp. 878–886, 2010.
- [40] P. Salomé, V. Fjällström, A. Hultqvist, and M. Edoff, "Na doping of CIGS solar cells using low sodium-doped mo layer," *IEEE Journal of Photovoltaics*, vol. 3, no. 1, pp. 509–513, 2013.

Research Article

Light Scattering and Current Enhancement for Microcrystalline Silicon Thin-Film Solar Cells on Aluminium-Induced Texture Glass Superstrates with Double Texture

Yunfeng Yin,^{1,2} Nasim Sahraei,^{1,2} Selvaraj Venkataraj,¹ Sonya Calnan,³ Sven Ring,³ Bernd Stannowski,³ Rutger Schlatmann,³ Armin G. Aberle,^{1,2} and Rolf Stangl¹

¹Solar Energy Research Institute of Singapore, National University of Singapore, Singapore 117574

²Department of Electrical and Computer Engineering, National University of Singapore, Singapore 117583

³Helmholtz-Zentrum Berlin für Materialien und Energie GmbH, PVcomB, Schwarzschildstrasse 3, 12489 Berlin, Germany

Correspondence should be addressed to Yunfeng Yin; yunfeng.yin@nus.edu.sg

Received 26 October 2014; Accepted 23 December 2014

Academic Editor: Francesco Bonaccorso

Copyright © 2015 Yunfeng Yin et al. This is an open access article distributed under the Creative Commons Attribution License, which permits unrestricted use, distribution, and reproduction in any medium, provided the original work is properly cited.

Microcrystalline silicon ($\mu\text{c-Si:H}$) thin-film solar cells are processed on glass superstrates having both micro- and nanoscale surface textures. The microscale texture is realised at the glass surface, using the aluminium-induced texturing (AIT) method, which is an industrially feasible process enabling a wide range of surface feature sizes (i.e., 700 nm–3 μm) of the textured glass. The nanoscale texture is made by conventional acid etching of the sputter-deposited transparent conductive oxide (TCO). The influence of the resulting “double texture” on the optical scattering is investigated by means of atomic force microscopy (AFM) (studying the surface topology), haze measurements (studying scattering into air), and short-circuit current enhancement measurements (studying scattering into silicon). A predicted enhanced optical scattering efficiency is experimentally proven by a short-circuit current enhancement ΔI_{sc} of up to 1.6 mA/cm² (7.7% relative increase) compared to solar cells fabricated on a standard superstrate, that is, planar glass covered with nanotextured TCO. Enhancing the autocorrelation length (or feature size) of the AIT superstrates might have the large potential to improve the $\mu\text{c-Si:H}$ thin-film solar cell efficiency, by reducing the shunting probability of the device while maintaining a high optical scattering performance.

1. Introduction

Silicon thin-film solar cells are of industrial interest due to the fact that (1) the (hydrogenated) silicon layers are obtained directly from the gas phase (thus avoiding expensive crystallisation technologies and material consuming sawing technologies) and (2) the solar module production process can be directly integrated into the cell production process (“monolithic integration”). Hydrogenated microcrystalline silicon ($\mu\text{c-Si:H}$), a mixed-phase material containing both amorphous and crystalline silicon regions, is widely used as a material forming the bottom cell of tandem or multijunction thin-film solar cells [1, 2]. In order to reduce manufacturing cost and excess carrier recombination, the $\mu\text{c-Si:H}$ absorber layer should be as thin as possible. However, due to the material's finite absorption coefficient, it is difficult to generate

a sufficiently high photogeneration rate within the $\mu\text{c-Si:H}$ film for a single pass of the light through the film. Therefore, light scattering technologies have to be used to enhance the effective light path within the film [3–5]. With the help of light trapping methods, photogenerated currents of above 30 mA/cm² can be generated, using around 3 μm thick $\mu\text{c-Si:H}$ films, and very high PV efficiency has been reported [6–8]. The conventional thin-film light trapping is achieved by either etching the front transparent conductive oxide (TCO) layer of the solar cell prior to the $\mu\text{c-Si:H}$ deposition or growing the TCO layer with a self-organized surface texture [9]. This usually creates a nanotextured surface, with typical feature sizes ranging from several tens of nanometres to several hundred nanometres [3, 9, 10]. This surface texture generally provides good light trapping properties for wavelengths up to 650 nm, but the ability to scatter near-infrared light from 700

to 1100 nm is quite modest. To overcome this problem, surface textures with a larger feature size are needed [11]. Photolithography was used to create periodic honeycomb patterns with microscale size, and a significant improvement of near-infrared light absorption was shown for substrate-type n-i-p $\mu\text{c-Si:H}$ thin-film solar cells [7, 12]. For superstrate-type p-i-n $\mu\text{c-Si:H}$ thin-film solar cells, texturing of the glass superstrate (leading to a microtextured glass surface) has been proposed recently, that is, using imprint-textured glass [11], rough glass by 3D texture transfer by ion etching [13], or aluminium-induced texture (AIT) glass [14–16] in order to enhance light trapping. Besides, double-textured TCO, for example, using HCl and HF wet etching leading to microscale and nanoscale surface textures, respectively, was also proposed and demonstrated to improve the light trapping ability for the silicon thin-film solar cells [17, 18]. In the present study, we use a double texture, that is, aluminium-induced texture glass superstrates (microtexture) covered with etched TCO (nanotexture), and compare its light trapping ability to a standard single-textured reference superstrate (i.e., planar glass covered with etched TCO). The AIT method enables us to obtain an industrially feasible microtextured glass surface with typical feature sizes in the 1–3 μm range (“AIT glass”). It has already been theoretically proven, using numerical computer simulation, that a double-textured superstrate has an excellent light scattering potential for the entire wavelength range from 300 to 1100 nm because of the superimposed scattering behaviour [19]. Experimentally, a double-textured superstrate was investigated, using ion-etched textured glass in combination with a self-organised textured (MOCVD made) TCO growth, proving a short-circuit current enhancement ΔI_{sc} of 1.5 mA/cm^2 compared to the planar glass/textured TCO reference superstrate [20]. Using AIT glass covered with etched TCO (double texture), we so far only investigated scattering into air (i.e., haze and angular resolved scattering), thereby highlighting the potential of a large ΔI_{sc} enhancement using a double texture [16]. However, on a device level, this has not yet been proven. This demonstration is the scope of this paper.

In order to investigate the benefit of a double texture (i.e., the benefit of AIT glass when using TCO etching for light trapping), three different superstrates are used (see Figure 1): (1) planar glass covered with textured TCO (“single-textured” reference superstrate, REF), (2) AIT glass exhibiting a moderate correlation length l covered with textured TCO, and (3) AIT glass exhibiting a large correlation length l covered with TCO (i.e., two different “double-textured” AIT glass superstrates, AIT-1 and AIT-2). The surface morphologies of these superstrates are studied by means of atomic force microscopy (AFM) and subsequent image processing. Thin-film $\mu\text{c-Si:H}$ solar cells are processed on these textured superstrates and the resulting short-circuit currents I_{sc} are investigated using current-voltage (I - V) as well as external quantum efficiency (EQE) measurements, in order to determine the optical scattering enhancement into silicon, if a double-textured superstrate is used. Furthermore, the influence of different AIT glass morphologies on the ΔI_{sc}

and on the solar cell efficiency, compared to the single-textured reference superstrate, is discussed.

2. Experimental Details

Three pieces of $10 \times 10 \text{ cm}^2$ soda lime glass sheets (3 mm thick) were used. Two of them were textured on one surface with the AIT method [14–16, 21], and the remaining one was not textured (reference). By changing the Al thickness, reaction time, and etching time, the surface morphology and the corresponding haze values of AIT glass sheets can be well controlled; see [16] for a detailed study. The surface morphology and visible light haze values were measured using an atomic force microscope (Veeco, model DI-3100 Nanoman) and a digital hazemeter (BYK haze guard, model AT-4725, light source: tungsten lamp). The spectrally resolved haze values (ranging from 400 to 1200 nm) were measured by UV-VIS spectroscopy (Perkin-Elmer, Lambda 950). All three glass sheets (planar and textured) were cleaned with DI water and then coated with an aluminium-doped zinc oxide film (ZnO:Al or “AZO”), using DC magnetron sputtering from a ceramic $\text{ZnO:Al}_2\text{O}_3$ tube target. Next, the AZO films were etched in a highly diluted HCl solution, leading to a nanoscale surface texture on the AZO films. Thus, one single-textured reference superstrate (planar glass covered with nanotextured TCO) and two double-textured AIT superstrates (microtextured glass covered with nanotextured TCO) were processed [16]. All glass sheets were then cut into two parts. Half of them were used as superstrates for thin-film solar cell fabrication, while half were used for surface morphology characterisation. For solar cell fabrication, the AZO coated glass sheets were cut into $5 \times 5 \text{ cm}^2$ pieces. They were then attached to a $30 \times 30 \text{ cm}^2$ stainless steel sample holder and loaded into a conventional RF (13.56 MHz) PECVD system (Applied Materials, AKT 1600) for silicon thin-film deposition. Doped $\mu\text{c-SiO}_x\text{:H}$ films, doped with either boron or phosphorus, were used as p-type or n-type hole/electron collecting layers of the p-i-n thin-film solar cells, with a target thickness in the range of 20–30 nm for the reference superstrate. The intrinsic $\mu\text{c-Si:H}$ absorber layer (target thickness of 1.75 μm for the reference superstrate) was deposited at a temperature of 190°C. It is emphasised that the resulting absorber layer thickness for the AIT glass superstrates is significantly lower ($\sim 1.5 \mu\text{m}$), despite the fact that the same deposition run was used. This large thickness difference indicates a strong influence of the surface morphology on the thin-film deposition by PECVD, as, for example, highlighted in [22]. Next, a thin AZO film ($\sim 80 \text{ nm}$) combined with a 150 nm thick silver layer was deposited onto the thin-film silicon diode, serving as back surface reflector and rear contact of the solar cell. Finally, laser patterning was applied to define isolated cells with an area of $1.0 \times 1.0 \text{ cm}^2$. The I - V characteristics of the cells were measured under standard test conditions (AM1.5G spectrum, cell temperature 25°C), using a class AAA dual-light-source solar simulator (Wacom, WXS_156S_L2). Cross-sectional images of the solar cells were taken by field emission transmission electron microscopy (XTEM, JEOL-JEM, 2010F) to determine their thickness.

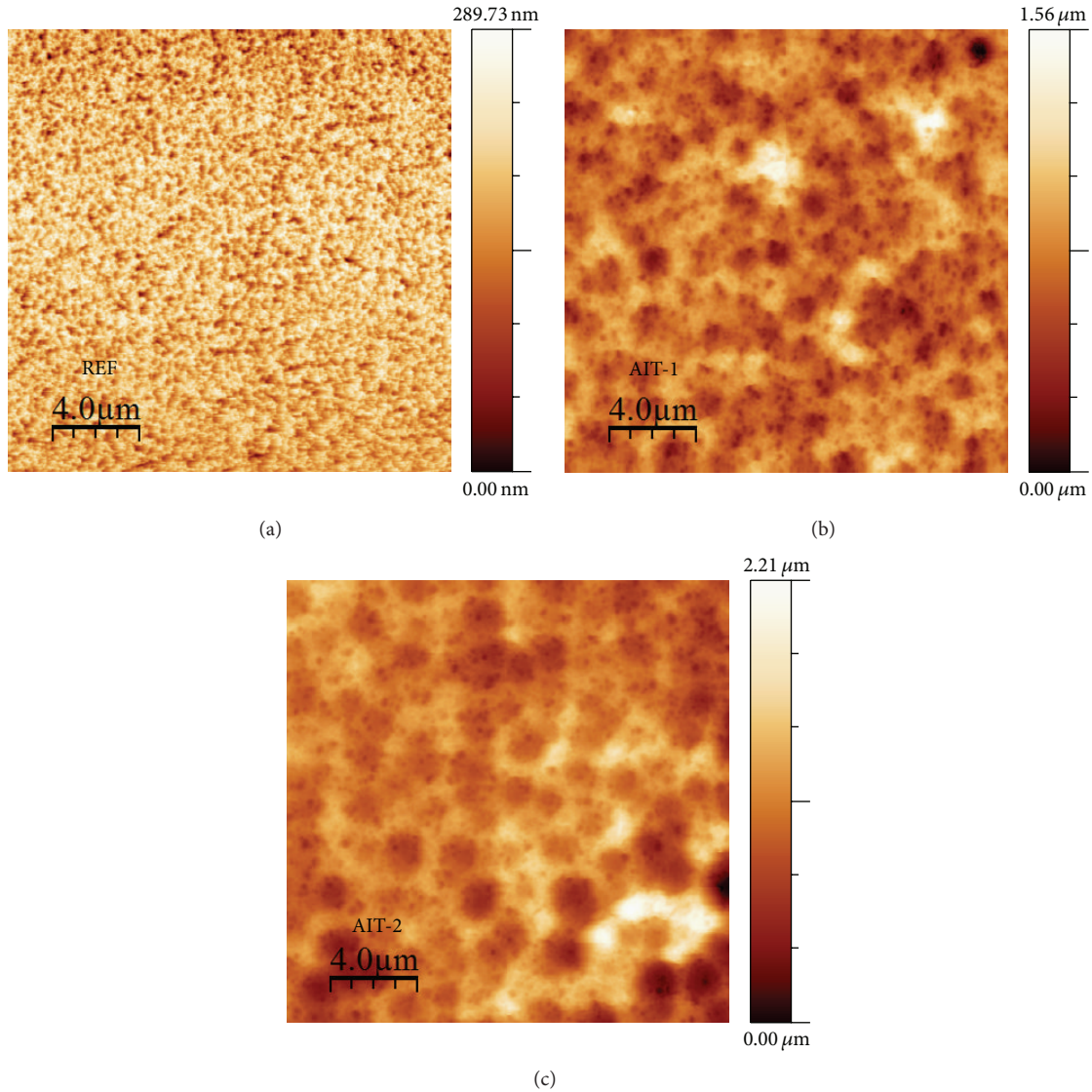


FIGURE 1: AFM images of the three different superstrates used in this study. (a) Planar glass superstrate covered with nanotextured TCO (reference superstrate); (b, c) microtextured AIT glass superstrate covered with nanotextured TCO. The AIT superstrate in (b) has an intermediate autocorrelation length l (mean feature size), while that in (c) has a large autocorrelation length.

3. Results and Discussion

3.1. Surface Morphology and Haze of the Superstrates. The three different superstrates mentioned above were investigated by AFM. From the $20 \times 20 \mu\text{m}^2$ AFM images as shown in Figure 1, surface morphology information such as mean surface roughness, surface angle distribution, and autocorrelation length were extracted (see Table 1) using the methods described in [23]. As compared to the reference superstrate (planar glass coated with nanotextured TCO), the AIT glass superstrates (microtextured glass coated with nanotextured TCO) show quite different characteristics. As expected, the AIT samples have much higher surface roughness (RMS) than the reference sample (about 200 nm versus 36 nm). Also the mean feature size of the textured superstrates (i.e., the autocorrelation length l , which is a good indicator for

the mean lateral feature size of randomly textured surfaces and which can be obtained from the autocorrelation function which can be extracted from AFM image data processing [23]; see Figure 2) differs considerably: for the reference superstrate the autocorrelation length is as small as 150 nm, whereas the AIT-1 superstrate has a moderate autocorrelation length of about 750 nm and the AIT-2 superstrate has a large autocorrelation length of about 1050 nm; see Table 1. The autocorrelation function is an indicator of spatial persistency (or similarity) of the surface structure to itself at two positions of the surface. The distance between these two points is called lag length [24]. Assuming that the autocorrelation function can be presented by an exponential function, the autocorrelation length l is defined as the lag length for which the autocorrelation function equals $1/e$ (0.3678); see Figure 2. As expected from the AFM images of the superstrates in Figure 1,

TABLE 1: Measured haze values of visible light and calculated surface morphology parameters for the different superstrates used. With the exception of haze, all parameters were measured after TCO deposition and TCO texturing; that is, the AIT glass superstrates are double-textured (microtextured glass covered with nanotextured TCO).

	Reference	AIT-1	AIT-2
Haze (no TCO) (%)	0	50	70
Haze (with TCO) (%)	12	65	74
RMS (nm)	36	188	284
Autocorrelation length l (nm)	150	742	1050
Average surface angle ($^{\circ}$)	20	40 (max at 30 and 50)	40 (max at 30 and 50)

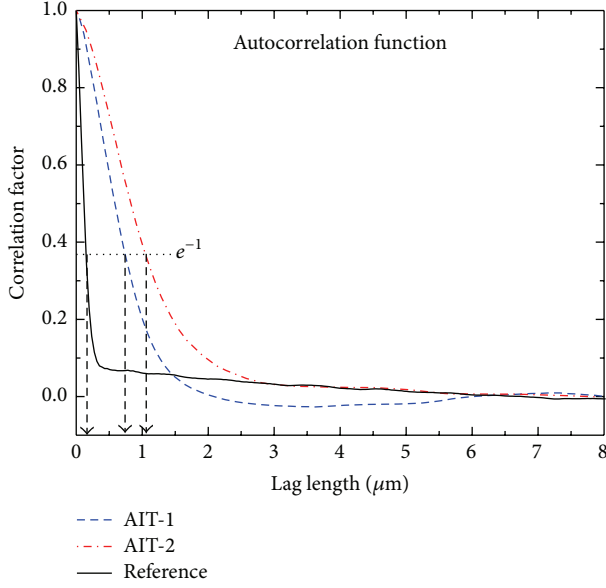


FIGURE 2: Determining the autocorrelation length l for the three different superstrates used.

the autocorrelation length (the mean feature size) of the reference superstrate is much smaller than that of the AIT samples.

Surface angle distributions were extracted from the AFM images, as described in [23], specifying the probability of encountering a specific surface angle between 0 degrees (flat surface) and 90 degrees (surface perpendicular to the substrate plane); see Figure 3. Interestingly, AIT-1 and AIT-2 have similar surface angle distributions; see Figure 3. Both superstrates exhibit an average surface angle of 40 degrees, with a pronounced maximum at 30 and 50 degrees, respectively. Based on the extracted surface morphology data, a simplified surface morphology model describing the three different superstrates is proposed; see Figure 4. Referring to this simplified surface morphology model, the reference superstrate is nanotextured with an autocorrelation length (mean self-repeating feature size) of 150 nm and an average surface angle about 20 degrees due to the texture. The AIT glass superstrates are double-textured (microtextured glass and nanotextured TCO). They have an autocorrelation length (mean self-repeating feature size) of 742 μm or 1050 μm , respectively, an average surface angle of 40 degrees due to the microstructured glass, and an additional average surface angle of ± 10 degrees due to the superimposed nanotexture

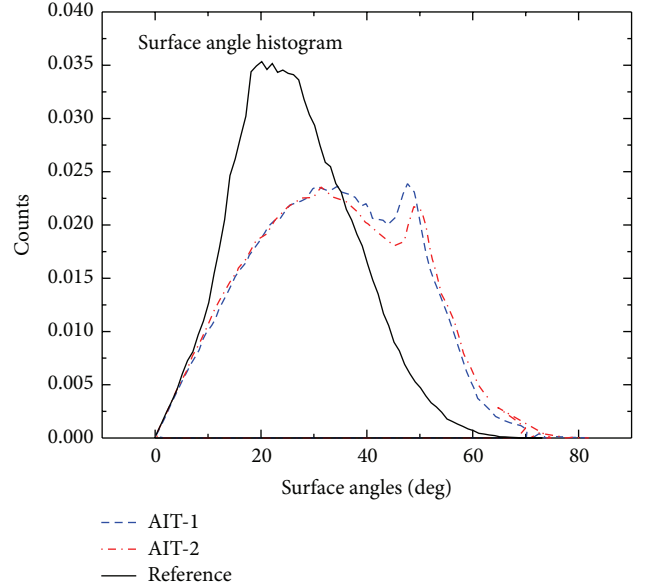


FIGURE 3: Surface angle distribution for the three different superstrates used.

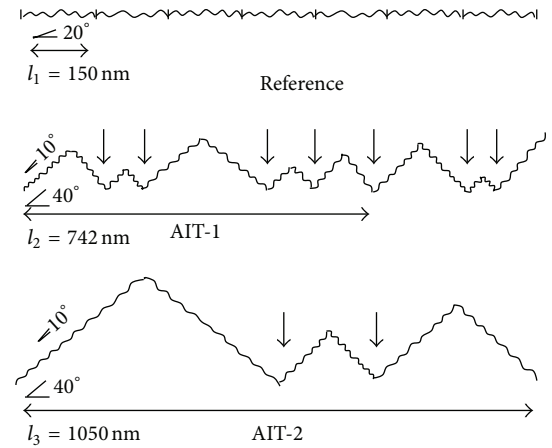


FIGURE 4: Schematic of the “simplified surface model” for the three different superstrates used.

stemming from the etched TCO. Thus, the average surface angle in the nanotextured surface valleys (“kinks”) of the double-textured AIT glass superstrates is either 30 or 50 degrees; see Figure 4. Furthermore, the number of “kinks” as

well as the surface roughness should correlate with the autocorrelation length l of the AIT glass superstrates (i.e., fewer “kinks” and higher surface roughness for AIT superstrates with higher autocorrelation length l).

“Kinks” are often found to be the sources of microcracks and thus also sources for recombination active regions within microcrystalline silicon solar cells [25]. They can also be sources for local shunt formation [26]. The schematic model clearly reveals that, within a certain area, the AIT-1 superstrate (with moderate correlation length l) has a much higher density of “kinks” than the AIT-2 superstrate (with large correlation length l). This means that AIT glass superstrates with a larger autocorrelation length have a lower shunting probability for the fabricated $\mu\text{c-Si:H}$ thin-film solar cells. The AIT-2 superstrate should therefore be less affected by local shunting, if used as a superstrate for $\mu\text{c-Si:H}$ solar cell processing.

Haze measurements (diffuse scattering into air) for visible light (400–700 nm) were performed on the 3 superstrates, both before and after the application of the nanotextured TCO. Without TCO, the reference superstrate (planar bare glass) shows no haze at all, while the haze values of the two AIT superstrates vary significantly (50% for AIT-1 and 70% for AIT-2). After the application of nanotextured TCO, the haze values of the two AIT glass superstrates differ much less (65% versus 74%), despite the fact that the autocorrelation length of the two samples is significantly different (742 versus 1050 nm). Compared to the haze of the reference superstrate (12%), the haze of the AIT superstrates is much higher. Table 1 compiles the measured haze and surface morphology parameters of the three investigated superstrates.

Furthermore, the spectrally resolved haze was measured; see Figure 5. Considering $\mu\text{c-Si:H}$ thin-film solar cells, the light scattering ability in the long-wavelength region (700–1100 nm) is most important. As can be seen in Figure 5, the haze values of the double-textured AIT superstrates improve significantly in the long-wavelength region (compared to the single-textured reference superstrate). Therefore a stronger scattering of long-wavelength photons and thus a higher short-circuit current enhancement ΔI_{sc} after $\mu\text{c-Si:H}$ thin-film solar cell processing can be expected for the AIT superstrates. Furthermore, it is expected that the AIT-2 superstrate will give a higher ΔI_{sc} than the AIT-1 superstrate.

3.2. Microcrystalline Silicon Thin-Film Solar Cells Grown on the Different Superstrates Used. Several 1 cm^2 $\mu\text{c-Si:H}$ thin-film solar cells were processed on the different superstrates discussed in the previous section. It is well known that the growth of $\mu\text{c-Si:H}$ is surface morphology dependent [26, 27]. As expected, the growth behaviour of $\mu\text{c-Si:H}$ was considerably different when deposited on the double-textured AIT glass superstrates (microtextured glass covered with nanotextured TCO) compared to depositing on the single-textured reference superstrate (planar glass covered with nanotextured TCO), that is, the resulting film thickness differs significantly. The $\mu\text{c-Si:H}$ layers deposited onto AIT glass superstrates are thinner (1.4–1.5 μm) compared to the layers deposited on the single-textured reference superstrate (1.7 μm), keeping the deposition time constant (i.e., using the same deposition process); see Figure 6. This difference can be attributed to

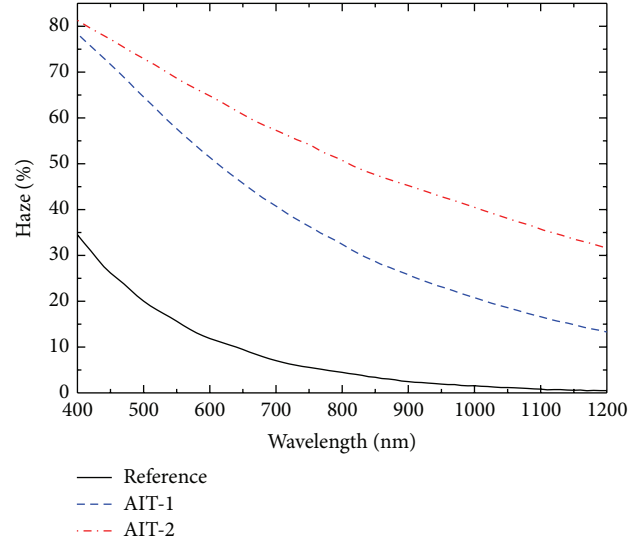


FIGURE 5: Spectrally resolved haze for the three investigated superstrates.

TABLE 2: One-sun I - V parameters of the best $\mu\text{c-Si:H}$ solar cells processed on the three investigated superstrates.

Superstrate	J_{sc} (mA/cm ²)	V_{oc} (mV)	FF (%)	Rsh ($\Omega\text{ cm}^2$)	Eff (%)
REF	20.1	487	64.9	440	6.4
AIT-1	21.3	431	57.9	220	5.3
AIT-2	21.7	475	59.9	270	6.2

the fact that the AIT superstrates have a larger surface area (around 13%) than the reference superstrate, stemming from the larger average surface angle of the microstructured AIT glass. Furthermore, the effects of shadowing and reemission should also be taken into consideration when depositing the films onto highly textured substrates [28].

Figure 7 and Table 2 show the corresponding one-sun I - V curves and the extracted solar cell parameters of the best $\mu\text{c-Si:H}$ solar cells obtained on the three investigated superstrates. As expected, processing on double-textured AIT superstrates does improve the light scattering within the solar cell: a significant ΔI_{sc} increase of 1.2 and 1.6 mA/cm² (5.8% and 7.7% relative) was observed for the AIT-1 and AIT-2 superstrates, respectively, compared to processing on the single-textured reference superstrate. Please note that the absolute short-circuit current density obtained for all solar cells is quite low ($\sim 21\text{ mA cm}^{-2}$) compared to the current state of the art (up to 30 mA cm^{-2}). This is due to three facts: (1) the processed $\mu\text{c-Si:H}$ deposition used was optimized for micromorph tandem (a-Si:H/ $\mu\text{c-Si:H}$) solar cell applications but not for single-junction $\mu\text{c-Si:H}$ solar cells like those investigated in this study, (2) a comparatively thin $\mu\text{c-Si:H}$ absorber layer thickness (1.4–1.5 μm) was used, compared to a 3 μm absorber thickness used in demonstrating an I_{sc} above 30 mA cm^{-2} [6, 7], and (3) an industrial feasible 3 mm thick soda lime glass was used instead of, for example, a 1 mm thin Corning glass. As expected, the current enhancement is

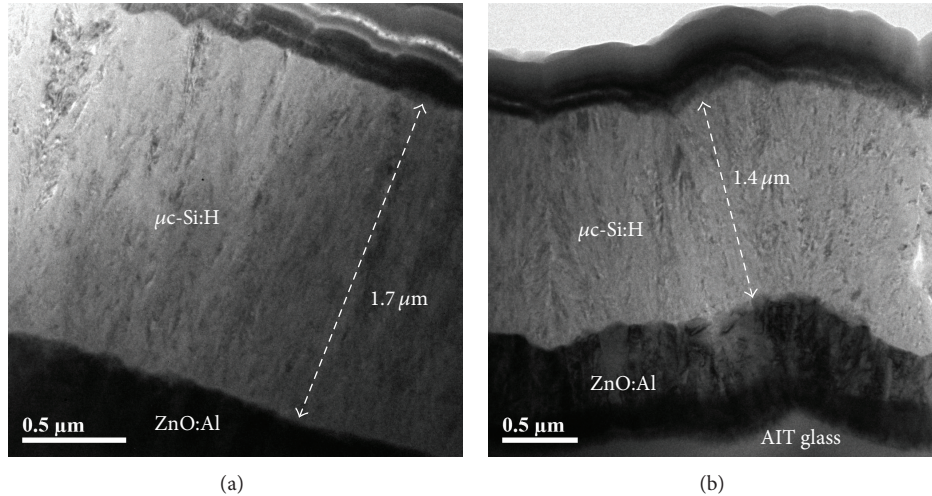


FIGURE 6: XTEM images of $\mu\text{c-Si:H}$ thin-film solar cells on (a) reference superstrate and (b) AIT glass superstrate.

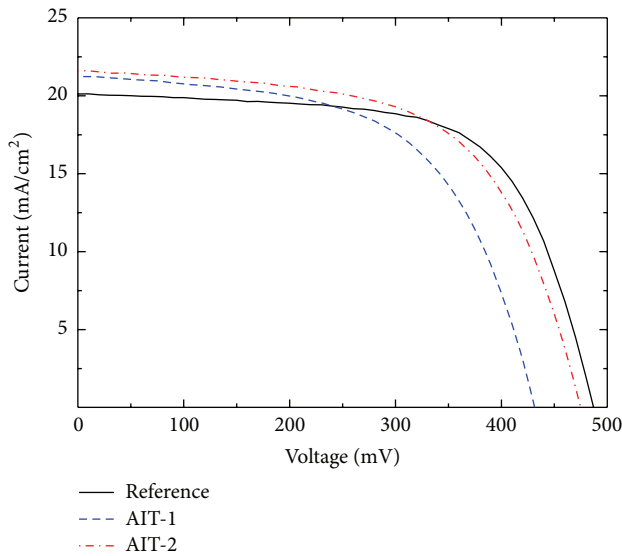


FIGURE 7: Measured one-sun I - V curves of $\mu\text{c-Si:H}$ solar cells processed on the three investigated superstrates.

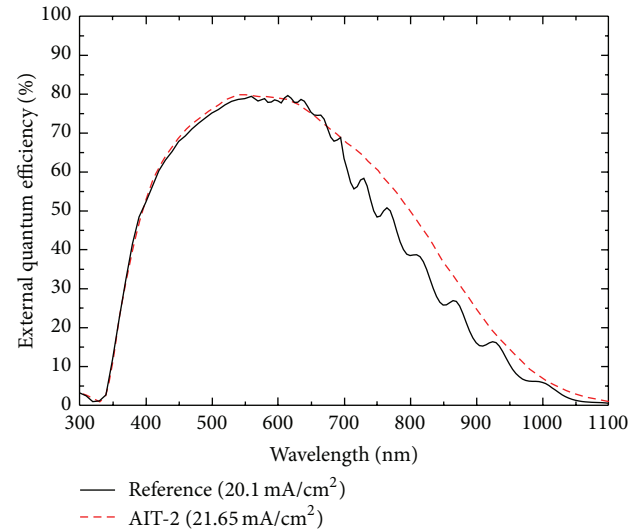


FIGURE 8: External quantum efficiency of $\mu\text{c-Si:H}$ thin-film solar cells processed on the reference superstrate and on the AIT-2 superstrate (the corresponding short-circuit current is indicated in the legend).

mainly ascribed to the better light absorption for the infrared light (700–1100 nm) (see the EQE curves in Figure 8) since the haze values in the long-wavelength region improved significantly by using AIT glass superstrates, as shown in Figure 5. Furthermore, given the fact that the $\mu\text{c-Si:H}$ film thickness on the AIT glass superstrates is thinner than on the reference superstrate, an even higher ΔI_{sc} increase can be expected if the film thickness is tuned to be identical. As expected, the AIT glass superstrate with the larger autocorrelation length (AIT-2) shows a higher ΔI_{sc} increase (compared to AIT-1).

Thus, analysing only the measured ΔI_{sc} using AIT glass superstrates clearly enhances the light scattering ability into silicon. However, analysing the resulting I - V curves, so far, all cells processed (even including the cells processed on the reference superstrate REF) do suffer from significant shunting. As expected, this shunting issue is much more severe with

processing on AIT glass superstrates. Thus a shunt-induced steep slope in the I - V curves towards low voltages is observed (for all three superstrates), and in case of the AIT superstrates the low shunt resistance even affects the open-circuit voltage (and also the measured short-circuit current) of the solar cells; see Figure 7 and Table 2. In case of no shunting, the short-circuit current enhancement of the AIT superstrate ΔI_{sc} would be even higher than reported. Again, in agreement with our expectations outlined above, the AIT superstrate with the larger autocorrelation length l (AIT-2) does suffer less from shunting compared to AIT-1. Indeed, defective areas (“cracks”) were observed when depositing $\mu\text{c-Si:H}$ films on AIT glass superstrates, that is, above deep valleys (“kinks”) which are induced by the AIT glass, as shown in Figure 9.

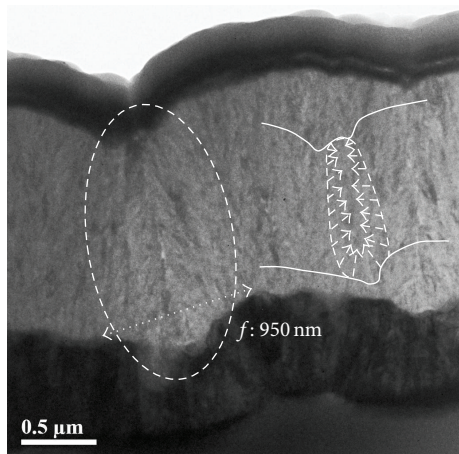


FIGURE 9: Measured crack or defective area formation (XTEM images) above deep valleys (“kinks”) induced by the AIT glass.

Further optimisation still needs to be done, that is, (1) extending the autocorrelation length of AIT samples as much as possible, thus experimentally determining the maximum ΔI_{sc} due to the use of AIT superstrates and simultaneously reducing the shunting probability and (2) depositing different $\mu\text{c-Si:H}$ thin-films on the microtextured AIT superstrates, which are better adapted to grow shunt-free on a microstructured texture, that is, using lower-crystallinity films. Generally, $\mu\text{c-Si:H}$ films with crystallinity of 50–60% are considered to be the best suited material for $\mu\text{c-Si:H}$ solar cells [29], when deposited on conventional superstrates (i.e., suitable for our reference superstrate, planar glass covered with nanotextured TCO). However, when deposited onto highly textured substrates (i.e., on AIT glass), it is proposed to use lower-crystallinity films (40–50%, with slightly poorer absorption of infrared wavelengths) or buffer layers [30]. Thus, it can be expected that by optimising the deposition conditions of $\mu\text{c-Si:H}$ films on AIT glass superstrates, as well as the AIT process itself, it should be possible to significantly reduce, or even eliminate, the local shunting problems experienced in our present experiments.

Based on the above analysis, $\mu\text{c-Si:H}$ thin-film solar cells processed on AIT superstrates show a large potential to improve the solar cell efficiency, since (1) the improved light trapping (a higher short-circuit current density compared to a standard reference superstrate) has been experimentally proven and (2) a reduction/elimination of the presently observed local shunt formation seems possible.

4. Conclusions

Microcrystalline silicon ($\mu\text{c-Si:H}$) thin-film solar cells were processed on aluminium-induced texture (AIT) glass superstrates. The influence of the surface topology on the optical scattering behaviour and on the $\mu\text{c-Si:H}$ film growth was investigated, by using a conventional single-textured reference superstrate (planar glass with nanotextured TCO) and two differently double-textured AIT glass superstrates (microtextured AIT glass covered with nanotextured TCO,

exhibiting a moderate or large autocorrelation length, resp.). Surface topology information, such as surface roughness, surface angle distribution, and autocorrelation length (indicating the mean surface feature size), was extracted from AFM images. Scattering was investigated via haze measurements (scattering into air) and via the measured short-circuit current enhancement compared to the reference superstrate (scattering enhancement into the silicon). A significant haze increase was observed when using AIT superstrates, resulting in a short-circuit current enhancement of 1.6 mA/cm^2 (7.7% relative increase). However, local shunt formation also emerged. A decreasing shunting probability was observed to correlate with an increasing autocorrelation length of the AIT superstrate. The experimental results predict that a further enhancement of the autocorrelation length (mean feature size) of the AIT superstrates shows a large potential for improving the solar cell efficiency, by reducing the shunting probability while maintaining (or even increasing) the light scattering abilities. Thus after optimization of the $\mu\text{c-Si:H}$ thin-film deposition process on highly textured surfaces, the use of double-textured AIT glass superstrates has a large potential for improving the efficiency of $\mu\text{c-Si:H}$ thin-film solar cells.

Conflict of Interests

The authors declare that there is no conflict of interests regarding the publication of this paper.

Acknowledgments

The Solar Energy Research Institute of Singapore (SERIS) is sponsored by the National University of Singapore (NUS) and Singapore’s National Research Foundation (NRF) through Singapore Economic Development Board (EDB). This work was partly supported by the PVcomB (Helmholtz-Zentrum Berlin), Germany.

References

- [1] A. Shah, J. Meier, E. Vallat-Sauvain et al., “Microcrystalline silicon and ‘micromorph’ tandem solar cells,” *Thin Solid Films*, vol. 403-404, pp. 179–187, 2002.
- [2] J. Yang, A. Banerjee, and S. Guha, “Triple-junction amorphous silicon alloy solar cell with 14.6% initial and 13.0% stable conversion efficiencies,” *Applied Physics Letters*, vol. 70, no. 22, pp. 2975–2977, 1997.
- [3] J. Müller, B. Rech, J. Springer, and M. Vaneczek, “TCO and light trapping in silicon thin film solar cells,” *Solar Energy*, vol. 77, no. 6, pp. 917–930, 2004.
- [4] C. Haase and H. Stiebig, “Thin-film silicon solar cells with efficient periodic light trapping texture,” *Applied Physics Letters*, vol. 91, no. 6, Article ID 061116, 2007.
- [5] K. Söderström, F.-J. Haug, J. Escarré, C. Pahud, R. Biron, and C. Ballif, “Highly reflective nanotextured sputtered silver back reflector for flexible high-efficiency n-i-p thin-film silicon solar cells,” *Solar Energy Materials and Solar Cells*, vol. 95, no. 12, pp. 3585–3591, 2011.

- [6] B. Yan, G. Yue, L. Sivec, J. Owens-Mawson, J. Yang, and S. Guha, "Correlation of texture of Ag/ZnO back reflector and photocurrent in hydrogenated nanocrystalline silicon solar cells," *Solar Energy Materials and Solar Cells*, vol. 104, pp. 13–17, 2012.
- [7] H. Sai, T. Koida, T. Matsui, I. Yoshida, K. Saito, and M. Kondo, "Microcrystalline silicon solar cells with 10.5% efficiency realized by improved photon absorption via periodic textures and highly transparent conductive oxide," *Applied Physics Express*, vol. 6, no. 10, Article ID 104101, 2013.
- [8] S. Hänni, G. Bugnon, G. Parascandolo et al., "High-efficiency microcrystalline silicon single-junction solar cells," *Progress in Photovoltaics: Research and Applications*, vol. 21, no. 5, pp. 821–826, 2013.
- [9] J. Bailat, D. Dominé, R. Schlüchter et al., "High-efficiency P-I-N microcrystalline and micromorph thin film silicon solar cells deposited on LPCVD ZNO coated glass substrates," in *Proceedings of the IEEE 4th World Conference on Photovoltaic Energy Conversion (WCPEC '06)*, pp. 1533–1536, May 2006.
- [10] M. Berginski, J. Hüpkes, M. Schulte et al., "The effect of front ZnO:Al surface texture and optical transparency on efficient light trapping in silicon thin-film solar cells," *Journal of Applied Physics*, vol. 101, no. 7, Article ID 074903, 2007.
- [11] U. W. Paetzold, W. Zhang, M. Prömpers et al., "Thin-film silicon solar cell development on imprint-textured glass substrates," *Materials Science and Engineering B: Solid-State Materials for Advanced Technology*, vol. 178, no. 9, pp. 617–622, 2013.
- [12] H. Sai, K. Saito, and M. Kondo, "Investigation of textured back reflectors with periodic honeycomb patterns in thin-film silicon solar cells for improved photovoltaic performance," *IEEE Journal of Photovoltaics*, vol. 3, no. 1, pp. 5–10, 2013.
- [13] W. Zhang, E. Bunte, J. Worbs et al., "Rough glass by 3d texture transfer for silicon thin film solar cells," *Physica Status Solidi (c)*, vol. 7, no. 3–4, pp. 1120–1123, 2010.
- [14] P. I. Widenborg and A. G. Aberle, "Polycrystalline silicon thin-film solar cells on AIT-textured glass superstrates," *Advances in Optoelectronics*, vol. 2007, Article ID 24584, 7 pages, 2007.
- [15] A. G. Aberle, P. I. Widenborg, and N. Chuangsuwanich, "Glass texturing," European Patent EP1613562 B1, 2011.
- [16] S. Venkataraj, J. Wang, P. Vayalakkara, and A. G. Aberle, "Light scattering enhancement by double scattering technique for multijunction thin-film silicon solar cells," *IEEE Journal of Photovoltaics*, vol. 3, no. 2, pp. 605–612, 2013.
- [17] M. Boccard, P. Cuony, C. Battaglia et al., "Nanometer- and micrometer-scale texturing for high-efficiency micromorph thin-film silicon solar cells," *IEEE Journal of Photovoltaics*, vol. 2, no. 2, pp. 83–87, 2012.
- [18] M. Steltenpool, E. Moulin, F.-J. Haug et al., "Nano-imprint technology combined with rough TCO morphology as double textured light-trapping superstrate for thin film solar cells," in *Proceedings of the 28th European Photovoltaic Solar Energy Conference and Exhibition (EU PVSEC '13)*, Paris, France, 2013.
- [19] O. Isabella, J. Krč, and M. Zeman, "Modulated surface textures for enhanced light trapping in thin-film silicon solar cells," *Applied Physics Letters*, vol. 97, no. 10, Article ID 101106, 2010.
- [20] A. Hongsingthong, T. Krajangsang, I. A. Yunaz, S. Miyajima, and M. Konagai, "ZnO films with very high haze value for use as front transparent conductive oxide films in thin-film silicon solar cells," *Applied Physics Express*, vol. 3, no. 5, Article ID 051102, 2010.
- [21] P. Vayalakkara, S. Venkataraj, J. Wang et al., "Aluminum induced glass texturing process on borosilicate and soda-lime glass superstrates for thin-film solar cells," in *Proceedings of the 37th IEEE Photovoltaic Specialists Conference (PVSC '11)*, pp. 003080–003083, Seattle, Wash, USA, June 2011.
- [22] M. Pelliccione, T. Karabacak, C. Gaire, G.-C. Wang, and T.-M. Lu, "Mound formation in surface growth under shadowing," *Physical Review B*, vol. 74, no. 12, Article ID 125420, 2006.
- [23] N. Sahraei, K. Forberich, S. Venkataraj, A. G. Aberle, and M. Peters, "Analytical solution for haze values of aluminium-induced texture (AIT) glass superstrates for a-Si:H solar cells," *Optics Express*, vol. 22, no. 1, pp. A53–A67, 2014.
- [24] J. M. Bennett and L. Mattsson, *Introduction to Surface Roughness and Scattering*, Optical Society of America, Washington, DC, USA, 1989.
- [25] H. B. T. Li, R. H. Franken, J. K. Rath, and R. E. I. Schropp, "Structural defects caused by a rough substrate and their influence on the performance of hydrogenated nano-crystalline silicon n-i-p solar cells," *Solar Energy Materials and Solar Cells*, vol. 93, no. 3, pp. 338–349, 2009.
- [26] M. Python, O. Madani, D. Dominé, F. Meillaud, E. Vallat-Sauvain, and C. Ballif, "Influence of the substrate geometrical parameters on microcrystalline silicon growth for thin-film solar cells," *Solar Energy Materials and Solar Cells*, vol. 93, no. 10, pp. 1714–1720, 2009.
- [27] Y. Nasuno, M. Kondo, and A. Matsuda, "Effects of substrate surface morphology on microcrystalline silicon solar cells," *Japanese Journal of Applied Physics, Part 2: Letters*, vol. 40, no. 4A, pp. L303–L305, 2001.
- [28] T. Karabacak, "Thin-film growth dynamics with shadowing and re-emission effects," *Journal of Nanophotonics*, vol. 5, no. 1, Article ID 052501, 18 pages, 2011.
- [29] Y. Mai, S. Klein, R. Carius et al., "Microcrystalline silicon solar cells deposited at high rates," *Journal of Applied Physics*, vol. 97, no. 11, Article ID 114913, 2005.
- [30] T. Söderström, F.-J. Haug, V. Terrazzoni-Daudrix, X. Niquire, M. Python, and C. Ballif, "N/I buffer layer for substrate microcrystalline thin film silicon solar cell," *Journal of Applied Physics*, vol. 104, no. 10, Article ID 104505, 2008.

Research Article

Optical Characterization of Different Thin Film Module Technologies

R. Ebner, B. Kubicek, G. Újvári, S. Novalin, M. Rennhofer, and M. Halwachs

Photovoltaic Systems, Energy Department, Austrian Institute of Technology (AIT), Giefinggasse 2, 1210 Vienna, Austria

Correspondence should be addressed to R. Ebner; rita.ebner@ait.ac.at

Received 26 November 2014; Revised 23 March 2015; Accepted 23 March 2015

Academic Editor: Aldo Di Carlo

Copyright © 2015 R. Ebner et al. This is an open access article distributed under the Creative Commons Attribution License, which permits unrestricted use, distribution, and reproduction in any medium, provided the original work is properly cited.

For a complete quality control of different thin film module technologies (a-Si, CdTe, and CIS) a combination of fast and nondestructive methods was investigated. Camera-based measurements, such as electroluminescence (EL), photoluminescence (PL), and infrared (IR) technologies, offer excellent possibilities for determining production failures or defects in solar modules which cannot be detected by means of standard power measurements. These types of optical measurement provide high resolution images with a two-dimensional distribution of the characteristic features of PV modules. This paper focuses on quality control and characterization using EL, PL, and IR imaging with conventional cameras and an alternative excitation source for the PL-setup.

1. Introduction

EL, PL, and IR imaging are nondestructive measurement techniques. These types of optical measurement provide fast, real-time, and high resolution images with a two-dimensional distribution of the characteristic features of PV modules. These technologies are applied effectively in quality control and development support and are important characterization tools in industry and research. In previous works, a combination of EL and IR measurements was proposed in order to quickly detect the most common defects in a PV module with high accuracy [1–3]. In this work a combination of EL, PL, and IR characterization tools is presented with the aim to increase the number of detectable defects and to determine their origin.

2. Theoretical Background

2.1. IR-Thermography. By means of IR measurements the thermal behavior of cells in a module and a number of defects (e.g., short circuits in solar cells, shunts, inactive cell parts, moisture, and defective bypass diodes) can be determined [4, 5]. IR measurements can be taken by using an external current or by applying light as heat source. Illuminated thermography imaging makes a comparison of modules operated

under different conditions, such as short circuit (I_{sc}), open circuit (U_{oc}), and maximum power point (P_m), possible. Several defects can be distinguished by varying the electrical load corresponding to certain states of the current-voltage characteristics [1].

In order to avoid thermal damaging in thin film modules, it has to be observed that the short circuit current of the module is not exceeded. For low voltages, below the threshold voltage of the diode, the current flows through the parallel resistance (R_p) and the series resistance (R_s). As $R_s < R_p$, the heating is mainly due to shunted areas. For voltages over the threshold, a large amount of the current flows through the diode itself and heats up the diode and the series resistance [6].

During measurements in the dark, no light is applied to the module but an external current (less than or equal to the short circuit current (I_{sc})) is supplied in forward direction [7]. In a previous work it was shown that dark thermography compared to illuminated thermography is a better tool for thin film modules [3]. Dark thermography images of thin film modules offer more detail and a better defect resolution compared to illuminated thermography images.

By means of an appropriate IR-camera, the temperature distribution can be identified and compared to EL and PL

measurements. Thermography imaging at AIT was performed by means of a portable, uncooled IR-camera. The wavelength sensitivity of the used IR-detector is between $7.5 \mu\text{m}$ and $15 \mu\text{m}$. As the front plate of all measured PV modules consists of a glass plate with a thickness of 3-4 mm and thus is only transparent for detectors with a wavelength of 3 to $5 \mu\text{m}$, only the temperature of the glass surface can be measured and not the radiation coming directly from the solar cells.

2.2. Dark Lock-In Thermography (DLIT). Dark lock-in thermography is a further nondestructive test method [8]. For DLIT, pulsed current is applied to the solar cell without illumination. Then, only the dark current flows within the cell. At shunt sites, an increased current causes heating of the solar cell which can be easily detected by LIT. The variations in temperature are in the area of one-tenth degree. The Fourier analysis of the local variations in temperature can be characterized as sinus wave with amplitude and phase. The ground frequency amplitude image gives information about the intensity of the heating sources in a module.

The dark lock-in thermography was mainly developed for the detection of shunts [9]. Noises, resolution, and contrast of DLIT analysis depend on the used excitation frequency as well as the recording time. By means of a cooled microbolometer based IR-camera and a power supply unit, a DLIT-System was built up. DLIT can be used for detailed failure analysis.

2.3. Electroluminescence (EL). EL measurements take advantage of the radiative interband recombination of excited charge carriers in solar cells. For EL investigations the module is operated as a light emitting diode. The emitted radiation due to recombination effects can be detected with a sensitive Si-CCD-camera. The wavelength window of the Si-CCD-camera is 300 to 1000 nm.

The solar cells are supplied with a defined external excitation current (current applied \leq short circuit current (I_{sc}) of the cell or module) while the camera takes an image of the emitted photons. Damaged areas of a solar module appear dark or radiate less than areas without defects. EL has proven to be a useful tool for investigating electrical inhomogeneities caused by intrinsic defects (e.g., grain boundaries, dislocations, shunts, or other process failures) and extrinsic defects (e.g., cell cracks, TCO corrosion, or interrupted contacts) [10–15]. The high resolution of the EL-images enables resolving some defects more precisely than in IR-images.

To determine the influence of defects (e.g., shunts), the EL-behavior of modules was investigated with different current densities [16]. When applying a low current density ($\sim 1/10$ of the I_{sc} of the cell or module) the conductivity of shunts is very high. When applying higher current densities ($\sim I_{sc}$ of the cell or module), the conductivity of the pn-junction increases compared to the shunt conductivity, and shunts are less influential on the EL intensity distribution. Thus, with low current densities, the material properties and, with high current densities, the properties of the electrical contacts can be investigated.

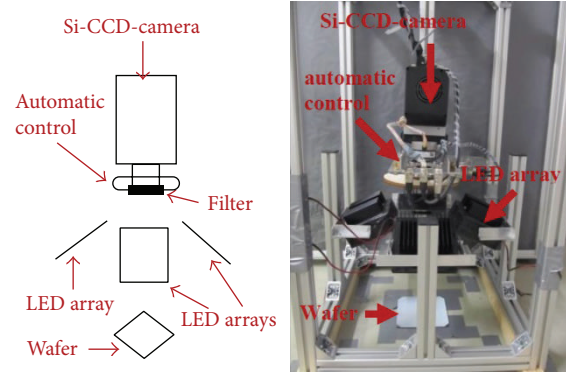


FIGURE 1: PL-setup.

2.4. Photoluminescence (PL). Photoluminescence (PL) imaging is, in contrast to EL imaging, a contactless and nondestructive measurement technique [17]. As no electric contacts are required, PL can be applied to solar cells before and after each processing stage.

The combination of PL imaging with EL imaging of finished cells gives further information about cell performance losses (e.g., resistance losses).

In PL imaging systems commonly high power lasers are used to generate excess charge carriers, and an InGaAs-CCD-camera works as detector. But as this equipment has limited resolution capacity, alternative equipment was searched for [18, 19]. Light emitting diode (LED) arrays turned out to be a very cost efficient alternative excitation source and further, a cooled Si-CCD-camera was used instead of an InGaAs camera.

The PL system built up at AIT consists of a sensitive Si-CCD-camera (300 to 1000 nm wavelength window) and different innovative IR-LED arrays with a peak wavelength between 534 nm and 850 nm (see Figure 1). Each LED spectrum was chosen to have a negligible overlap with the luminescence spectrum (950–1200 nm). In our setup the camera is placed on the same side as the LED arrays. This requires good filtering as a large portion of the excitation light is reflected on the wafer and strikes the camera. This is performed by a two-step filter, of which one is a custom-made anti-reflex-coated GaAs wafer, which is transparent in the range of the emitted PL photons. The second filter is a normal LP optical filter in front of the camera. The PL-setup as well as the EL-setup at AIT consists of an automatic control system, featuring a custom-made autofocus system. The problem is that the focus for visible and IR is different, and PL exposure times can be larger than 30 seconds. As manual focusing would be resource consuming, a computer-controlled system was created for this task. The measure for the sharpness is the average deviation of pixel brightness, and the approach occurs by a trisection algorithm, similar to normal binary dissection methods.

The PL-setup as well as the EL-setup at AIT consists of an automatic control system, featuring a custom-made autofocus system.

Depending upon the materials and the technology used, solar cells are better or worse at converting the different



FIGURE 2: EL-image, a-Si-module (before aging).

color bands of sunlight into electricity. The spectral sensitivity describes the wavelength range in which a cell works most efficiently and influences the efficiency under different irradiance conditions. While crystalline solar cells are particularly sensitive to long wavelength solar radiation, thin film cells utilize the visible light better. Amorphous silicon cells can absorb short wavelength light optimally. In contrast, CdTe and CIS are better at absorbing medium wavelength light. Because of the different sensitivity of thin film cells, for PL measurements of these technologies, also different LEDs have to be used. For a-Si-modules LED arrays with a peak wavelength of 550 nm, for CdTe-modules arrays with a peak wavelength of 680 nm, and for CIS/CIGS arrays with a peak wavelength of 850 nm are used. PL measurements of CIS, CdTe, and a-Si-modules were performed and compared with EL-images.

3. Experiments

3.1. Characterization of a-Si-Module

3.1.1. Characterization of an a-Si-Module before and after Aging Process. An a-Si-module was characterized, respectively, before and after performing some aging tests (preconditioning via light soaking, applying a reverse current). EL, IR, and performance measurements were executed and the results were compared. In the EL-image of the a-Si-module before aging (see Figure 2) there are no significant defects visible.

In the IR-image (see Figure 3) of the same module there are also hardly any defects identifiable. Only the metallic junction box was viewable as cooler area in the IR-image.

The EL-image of the a-Si-module after aging (Figure 4) mainly shows punctual shunts inside a cell or between the metal layers of two adjacent cells. In the cell area the punctual shunts appear as black points and between two cells, where the current flows through the shunt to the Si-layer of the next cell, bright points appear in the EL-image. The bright points are caused by increased recombination of electron-hole pairs and/or increased thermal radiation in the surroundings of the shunt area [20].

The dark thermography image of the a-Si-module (see Figure 5) almost shows the same defects compared to the

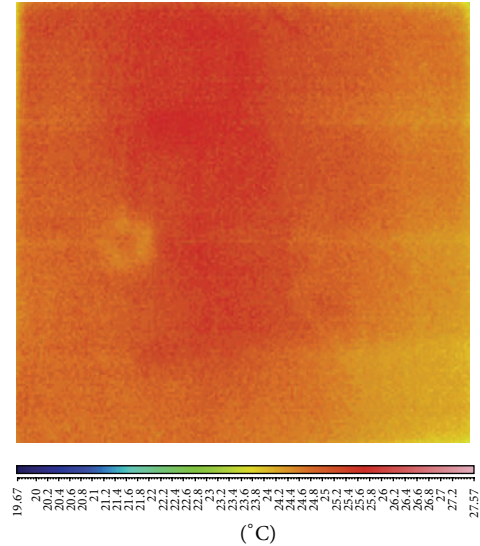


FIGURE 3: Dark IR-image, a-Si-module (before aging).

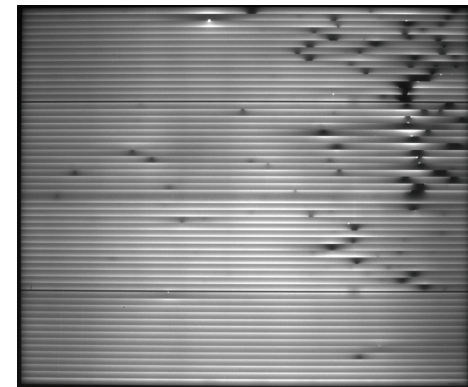


FIGURE 4: EL-image, a-Si-module (after aging).

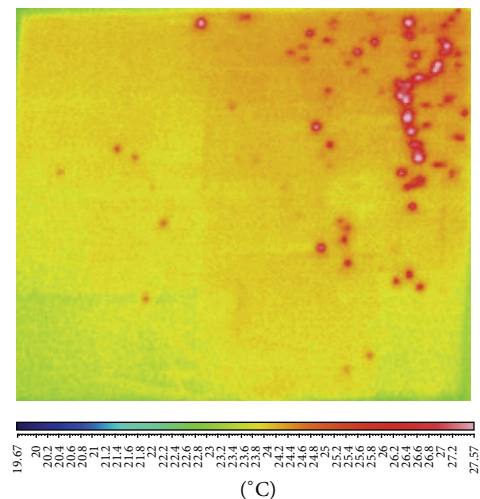


FIGURE 5: Dark IR-image, a-Si-module (after aging).

TABLE 1: Current-voltage measurement results.

	U_{oc} [V]	I_{sc} [A]	U_{mp} [V]	I_{mp} [A]	P_m [W]
Before aging	23.59	7.07	16.97	5.73	97.23
After aging	22.98	5.19	16.60	4.13	68.52

U_{oc} = open circuit voltage, I_{sc} = short circuit current, U_{mp} = voltage at P_m , I_{mp} = current at P_m , and P_m = maximum power point.

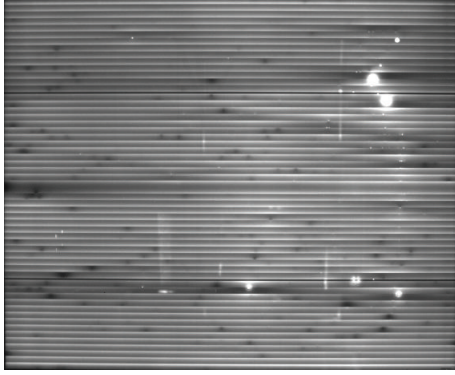


FIGURE 6: a-Si-module, EL-image.

EL-image. However, it is not always possible to identify the exact position of the defects.

As not all defects have an influence on the power output of cells or modules, performance measurements were executed in addition to the EL and IR measurements. These measurements show a relation between the increase of defects in a cell or module and the measured power losses.

After damaging the a-Si-module (Figure 4) a degradation of power of approximately 30% could be determined (Table 1). The reduced cell area leads to this power loss, mainly caused by the reduction of the short circuit current. The results of the current-voltage measurements before and after aging can be seen in Table 1.

3.1.2. Characterization of an a-Si-Module under External Bias and under Illumination. Another a-Si-module was characterized by means of EL and IR measurements. Before EL and IR measurements only preconditioning via light soaking was performed. The IR measurements were performed under external bias and under illumination.

The EL-image of an a-Si-module (see Figure 6) mainly shows punctual shunts inside a cell or between the metal layers of two adjacent cells. Inside a cell the punctual shunts appear as black points and between two cells, where the current flows through the shunt to the Si-layer of the next cell, bright points appear in the EL-image by increased recombination of electron-hole pairs [10].

The thermography images of the a-Si-module (Figures 7–10) almost show the same defects compared to the EL-image (Figure 6). Only in Figure 8, analyzing the illuminated thermography image of the a-Si-module operated at maximum power point, it was not possible to identify the exact position of the defects. The metal junction box of this a-Si-module is clearly viewable as cooler area in all illuminated IR-image.

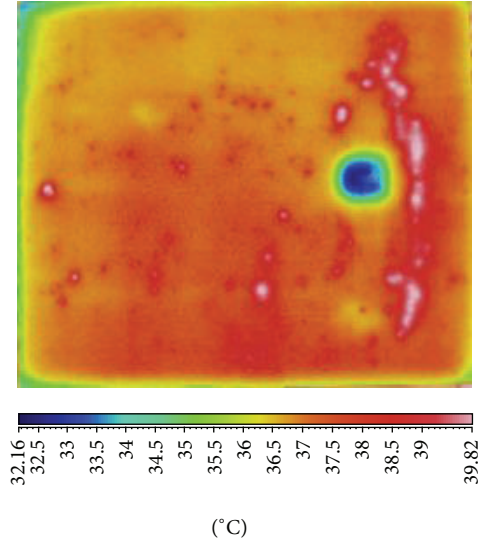
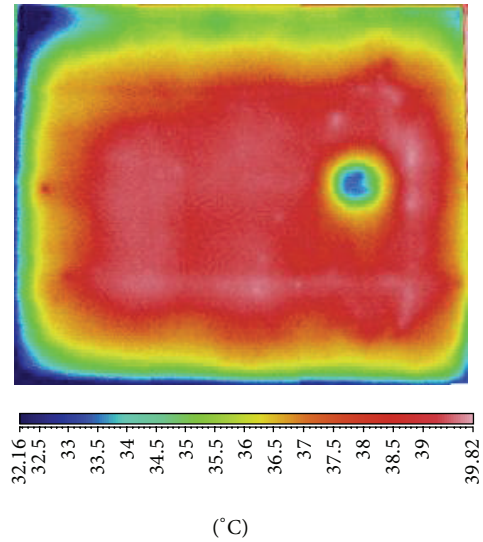
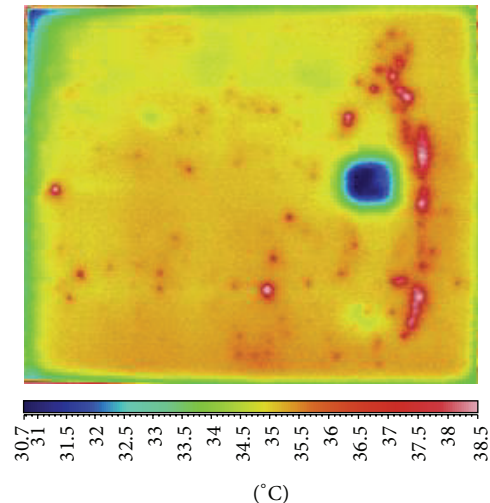
FIGURE 7: a-Si, I_{sc} operated, illuminated IR-image.

FIGURE 8: a-Si, MPP operated, illuminated IR-image.

FIGURE 9: a-Si, U_{oc} operated, illuminated IR-image.

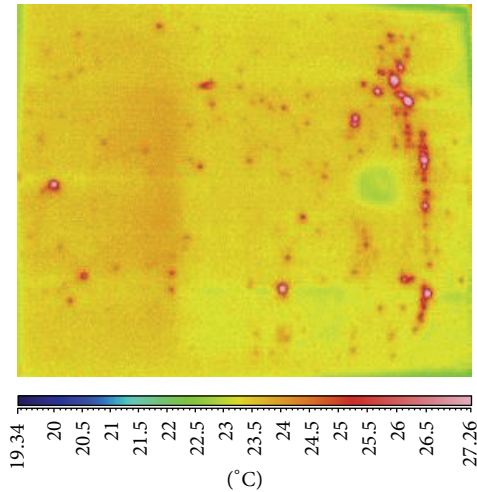


FIGURE 10: a-Si, dark thermography image.

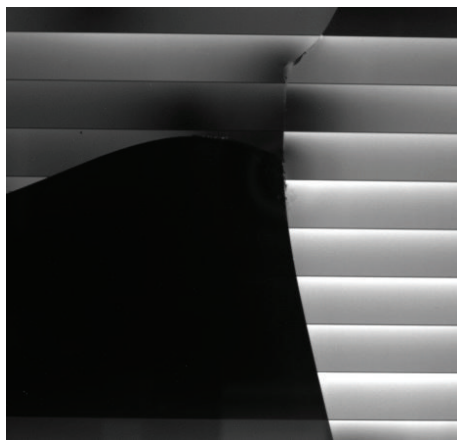


FIGURE 11: a-Si-module, EL-image.

Compared to the illuminated thermography images, the dark thermography image of the a-Si-module (Figure 10) supplies more details and a better defect resolution.

3.1.3. Comparison of Electroluminescence and Photoluminescence Images of a Broken a-Si-Module. Figure 11 shows the EL and Figure 12 the PL-image of a third a-Si-module. The module was broken after transport. The PL-image clearly gives more information about the material properties and the position and the origin of the defect. It is thus a fast and contactless method to investigate defect thin film modules.

3.2. Characterization of CdTe-Modules

3.2.1. Injection Current-Dependent EL Measurements of a CdTe-Module. A new CdTe-module was characterized by means of EL and IR measurements. Before EL and IR measurements only preconditioning via light soaking was performed. To determine the influence of defects (e.g., shunts) the EL-behavior of the module when applying different current densities was investigated. When applying a low current

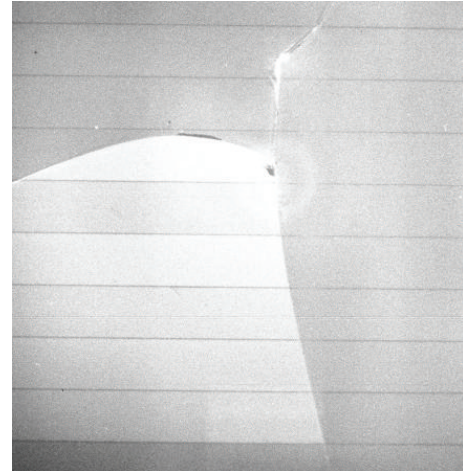


FIGURE 12: a-Si-module, PL-image.

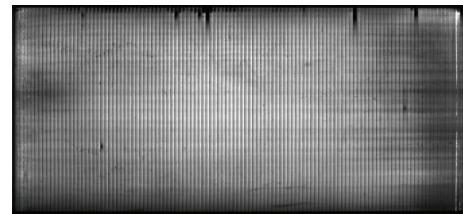


FIGURE 13: EL-image, CdTe-module (injected current: 1 A).

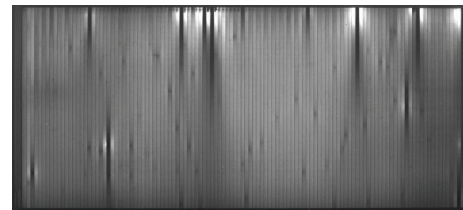


FIGURE 14: EL-image, CdTe-module (injected current: 0.1 A).

density the conductivity of shunts is very high. The stronger the shunts are the lower the EL intensity is in this area. Strong shunts are able to quench the EL intensity of a whole cell. When applying higher current densities, the conductivity of the pn-junction increases compared to the shunt conductivity, and shunts are less influential on the EL intensity distribution [21].

The EL-images of the CdTe-module, taken after applying different forward bias voltages, were compared. Figure 13 shows the EL-image of the CdTe-module with an injected current of 1 A (I_{sc} of the module) and Figure 14 shows the EL-image with an injected current of 0.1 A.

The comparison of the two EL-images shows very clearly that effective shunts are visible as punctual defects and thus better detectable when high currents are injected. On the contrary the EL intensity of the area around effective shunts is considerably increased when low currents are injected.

Most identified defects (mainly shunts) in the EL-image (Figure 14) of the CdTe-module are also visible in the dark

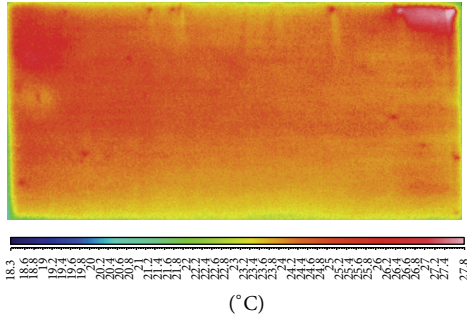


FIGURE 15: Dark IR-image, CdTe-module.

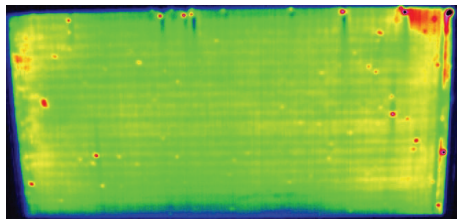


FIGURE 16: DLIT-image, CdTe-module. Temperature range: 0 to 0.05 Kelvin.

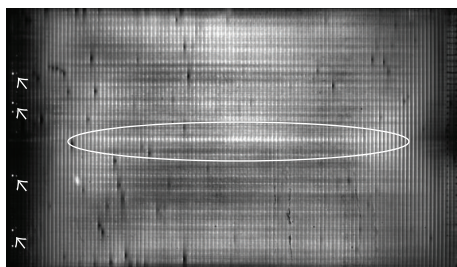


FIGURE 17: CdTe-module, EL-image.

thermography image (Figure 15). The hot spots identified in Figure 15 can be ascribed to areas with low shunt resistance, where the current flows through the defect and creates a heat source.

Figure 16 shows the dark lock-in thermography image (amplitude image) of the CdTe-module. Compared to the dark IR-image (Figure 15), the DLIT-image of the CdTe-module is even more detailed. The identification of the defect position is further improved and the DLIT-image is even better comparable to the EL-image (Figure 13). The interpretation is the same.

3.2.2. Characterization of a CdTe-Module under External Bias and under Illumination. A second CdTe-module was investigated. EL and IR measurements were performed. Before EL and IR measurements only preconditioning via light soaking was performed. Some identified defects (mainly shunts) in the EL-image (Figure 17) of the CdTe-module are also clearly visible in the dark thermography image (Figure 21). In the middle of the EL-image (marked with a white oval) there is an area with a very high intensity resulting from a higher local current density. This higher current density leads to an

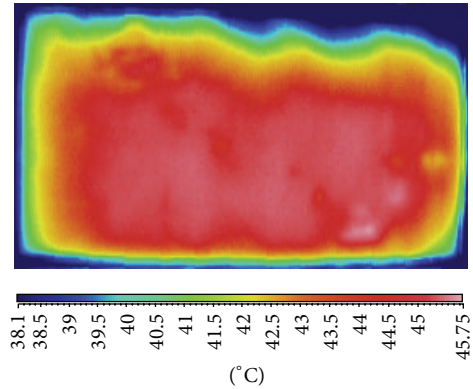
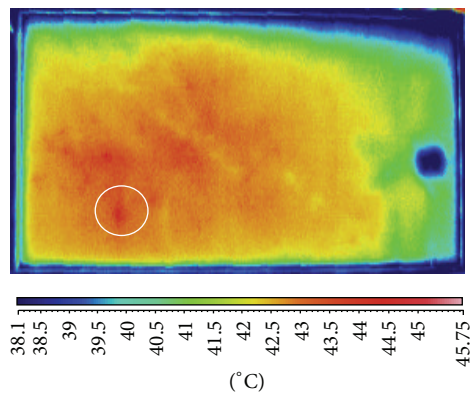
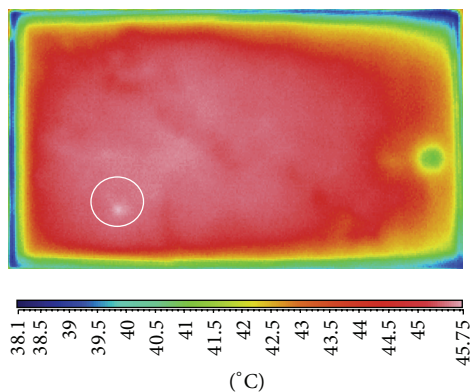
FIGURE 18: CdTe, I_{sc} operated, illuminated IR-image.

FIGURE 19: CdTe, MPP operated, illuminated IR-image.

FIGURE 20: CdTe, U_{oc} operated, illuminated IR-image.

increased heat development which can also be seen in the dark thermography image (Figure 21) of the CdTe-module. A reason for this defect could be a decreased electrical contact area (caused by corrosion or aging) next to this very active area.

One shunt which is marked with a white circle in Figure 19 could also be identified in Figure 20. In Figure 19, the illuminated thermography image of the CdTe-module operated at P_m , more defects could be detected than in Figures 18 and 20.

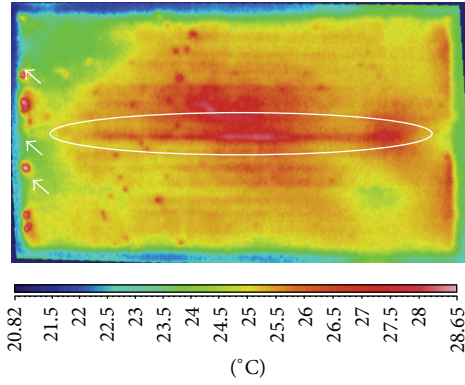


FIGURE 21: CdTe, dark thermography image.

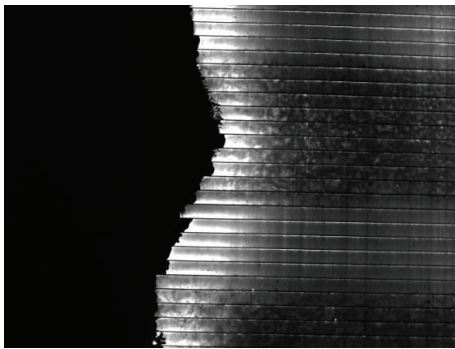


FIGURE 22: CdTe-module, EL-image.



FIGURE 23: CdTe-module, PL-image.

Some shunts, which are not so clearly identifiable on the left side of the EL-image (Figure 17, marked with white arrows), are clearly visible in the dark thermography image (Figure 21).

These performed illuminated IR measurements of the CdTe-modules confirmed again that dark thermography is a better tool for defect detection than illuminated thermography.

3.2.3. Comparison of Electroluminescence and Photoluminescence Images of a Broken CdTe-Module. Figure 22 shows the EL-image and Figure 23 the PL-image of a third CdTe-module. The module was broken after transport. The

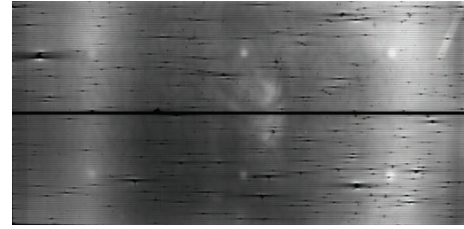


FIGURE 24: EL-image, CIS-module.

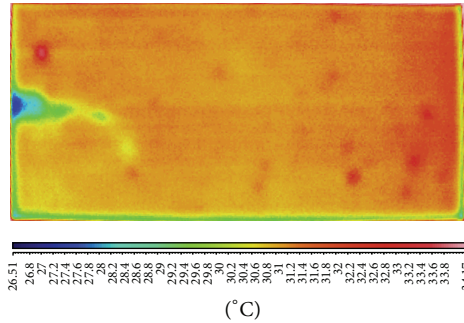


FIGURE 25: IR-image, I_{sc} operated, CIS-module.

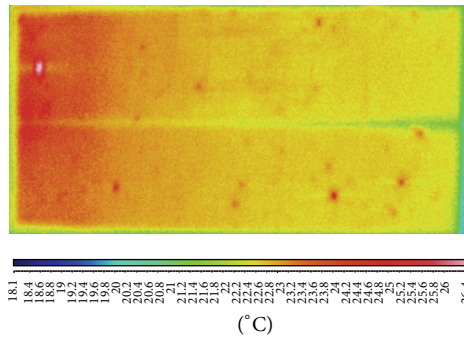


FIGURE 26: Dark IR-image, CIS-module.

PL-image clearly gives more information about the material properties and the position of the defect.

3.3. Characterization of CIS-Modules

3.3.1. Comparison of Electroluminescence and Thermography Images of a CIS-Module. A new CIS-module is analyzed by EL and IR measurements [22]. Before EL and IR measurements only preconditioning via light soaking was performed. Figure 24 shows the EL-image of a CIS-module. Punctual areas of reduced EL intensity can be caused by shunts. As shunts are easier to locate at high current densities the I_{sc} of the module was applied.

By means of an illuminated thermography image (Figure 25) of the CIS-module operated under short circuit some hot spots are visible but not as clearly as in the dark thermography image (see Figure 26).

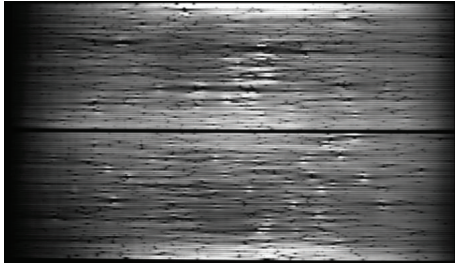
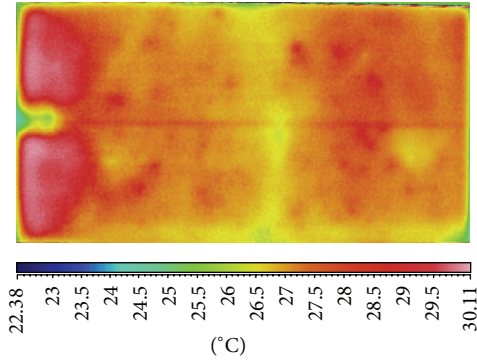


FIGURE 27: EL-image, CIS-module.

FIGURE 28: CIS, I_{sc} condition, illuminated IR-image.

It turned out that dark thermography measurements of CIS-modules generally supplied more detailed images than illuminated thermography measurements.

3.3.2. Comparison of Electroluminescence and Thermography of a Damaged CIS-Module. Figure 27 shows the EL-image of a CIS-module, where preconditioning via light soaking was performed and a reverse current ($< I_{sc}$) was applied. Punctual areas of reduced EL intensity are caused by shunts. Again the short circuit current (I_{sc}) of the module was applied in order to locate the shunts easier. The conductivity of the pn-junction increases with injected current densities compared to the shunt conductivity, and shunts are less influential on the EL intensity distribution.

The darker edges in the EL-image (see Figure 27) of the CIS-module, which corresponds well with a slight temperature rise in the IR-images, are due to reduced parallel resistance. In the case of reduced parallel resistance a part of the current flows through the shunt leaving less current to flow through the diode, which leads to a reduced EL intensity. The reason for reduced parallel resistance could be, for instance, conductive oxide layer corrosion.

By means of illuminated thermography images (Figures 28–30) and a dark thermography image of the CIS-module (Figure 31), a number of hot spots were identified. In Figures 28–30 hot spots can be ascribed to areas with low shunt resistance, where the current flows through the defect and creates a heat source.

The dark thermography image of this CIS-module again showed the defects (shunts) in more detail compared to the illuminated IR-images.

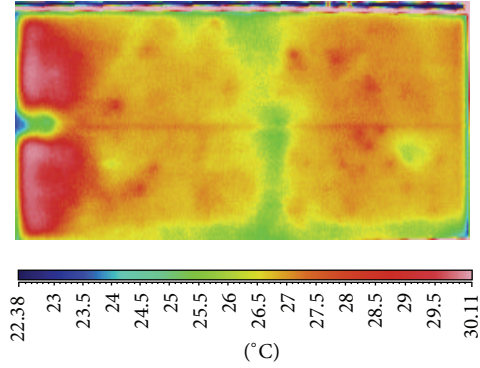


FIGURE 29: CIS, MPP condition, illuminated IR-image.

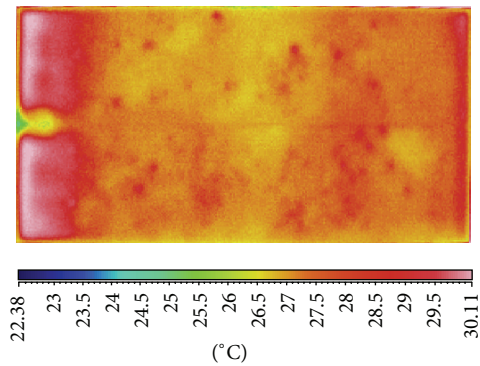
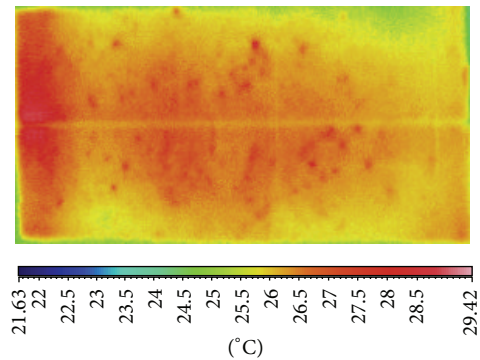
FIGURE 30: CIS, U_{oc} condition, illuminated IR-image.

FIGURE 31: CIS, dark thermography image.

Concerning IR-thermography measurements it could already be confirmed in previous publications that illuminated thermography is more suited for crystalline modules and dark thermography is a better tool for thin film modules [23]. Several defects can be distinguished by varying the electrical load corresponding to certain states on the current-voltage characteristic. Under short circuit condition the IR-image gives an impression of different short circuits of single cells. If the module is illuminated and operated at maximum power point condition (P_m), cells with low short circuit current (I_{sc}) no longer appear hot and only cells with high series resistance and severe cracks are identifiable. Modules

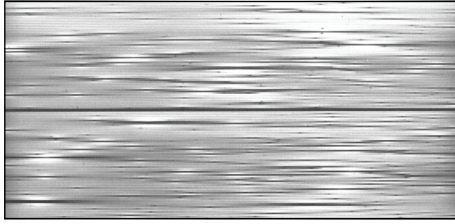


FIGURE 32: CIS-module, EL-image (0.1 A).

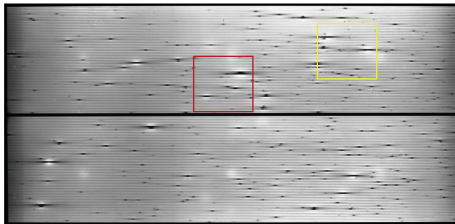


FIGURE 33: CIS-module, EL-image (1 A).

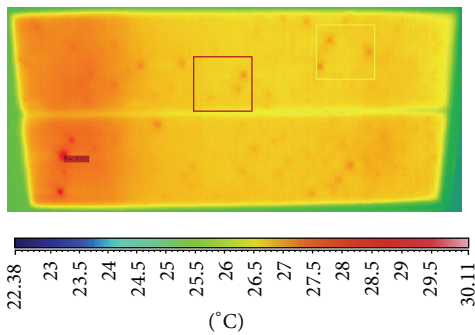


FIGURE 34: CIS-module, dark IR-image.

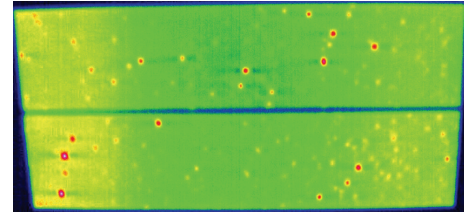


FIGURE 35: CIS-module, dark lock-in thermography image. Temperature range: 0–0.35 Kelvin.

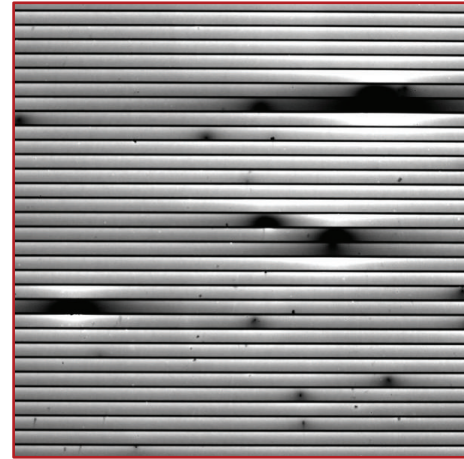


FIGURE 36: CIS-module, EL-image.

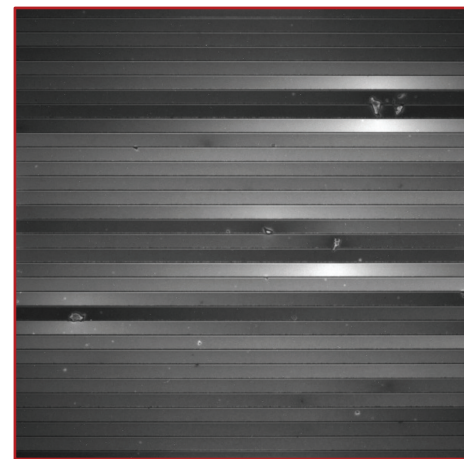


FIGURE 37: CIS-module, PL-image.

operated under open circuit condition (U_{oc}) are expected to show heating mainly caused by low I_{sc} and not by increased series resistance [24].

In summary, it can be stated that dark thermography images, compared to illuminated thermography images, supply more details and a better defect resolution for thin film modules. For crystalline modules the opposite is true [2].

3.3.3. Comparison of EL-, IR-, and PL-Images of a CIS-Module. Another CIS-module was investigated by EL, IR, and PL measurements [25]. Before the measurements only preconditioning via light soaking was performed. The EL-images of a CIS-module, taken after applying different forward bias voltages, were compared (see Figures 32 and 33). In Figure 32 the effectiveness of the shunts could be identified and Figure 33 shows the position of the defects (mainly shunts) in more detail.

Figure 34 shows the dark IR-image of the CIS-module and Figure 35 the dark lock-in thermography image of the same module. In the DLIT-image the defects are given in more detail and are thus better comparable to failures discovered in the EL-image (Figure 33).

In addition photoluminescence (PL) measurements were executed in order to further increase the defect analysis (Figures 37 and 39). EL- and PL-images of two sections of the CIS-module, which were marked with a red and a yellow rectangle, were performed and compared. It can be clearly seen that the defects are given in more detail in the PL-images. In the EL-images there are only dark areas with no exact position of the defect (Figures 36 and 38). In the PL-image the exact position is determinable.

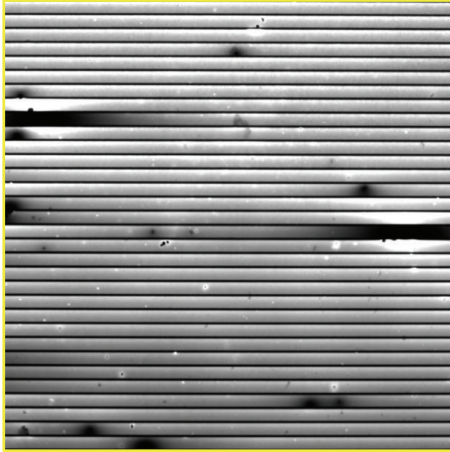


FIGURE 38: CIS-module, EL-image.

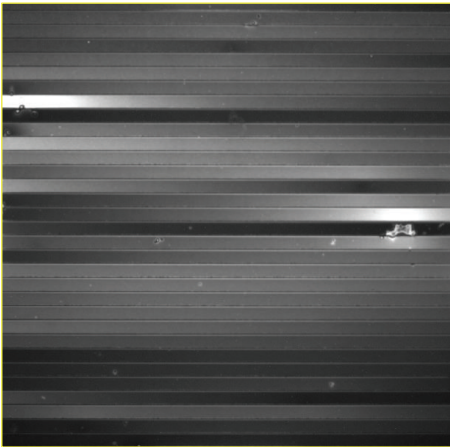


FIGURE 39: CIS-module, PL-image.

4. Summary

Table 2 shows a summary of the advantages and disadvantages of the different characterization methods (EL, PL, IR, and DLIT).

5. Conclusion

EL is a good method to detect microcracks, interrupted contacts, or a number of process failures (e.g., shunts) but it was not possible to determine the influence of these defects on the cell/module power output.

Performed IR measurements proved that on the one hand not all identified defects lead to an increase in temperature and on the other hand cells/modules with unremarkable EL-images sometimes supply IR-images with hot areas, which are caused by high power losses. In the thermography images of thin film modules the exact position of the defects could not

always be identified and the great number of small spots made a determination difficult.

In the case of sun illuminated thermography, varying of the electrical load helps to distinguish several defects. If the voltage is increased from zero to voltage at P_m , some hot spots disappear because of the different I_{sc} of the cells. The hot spots which vanish if the voltage is increased towards U_{oc} are caused by areas of increased series resistance [26].

DLIT-imaging is, compared to the dark IR imaging method, an improved characterization tool. The defects are better identifiable with a better resolution compared to dark IR measurements. Therefore, DLIT-images are also better comparable to failures discovered in the EL-image.

A very essential loss mechanism mainly for thin film modules is the loss due to localized shunts in the module. A typical thin film module consists of a number of elongated cells connected in series and separated from each other by scribe-lines. Shunt paths can be caused by imperfection in the scribing procedure, during film growth procedure (e.g., penetration of the junction depletion layer) or when layers are too thin or not properly deposited. The existence of localized shunts and, respectively, hot spots could also be proved in this work by means of EL and IR-thermography measurements.

Finally it could be proved that the effectiveness of defects (e.g., very strong shunts) is identifiable by means of current-dependent EL measurements.

First performed PL measurements of a-Si-, CdTe-, and CIS-modules were presented and compared with EL-images and IR-images. The PL-setup is further optimized.

PL measurements can be used to detect defects throughout the entire solar cell manufacturing process. In a previous work PL imaging was used for analyzing solar cells in PV modules and for the investigation of contact properties [27, 28]. PL-images help to find out if material defects or contacting problems are the reason for power losses in solar cells and modules. Compared to EL-images, PL imaging has the advantage that contacting failures do not influence the contrast of the PL-images.

Concerning thin film modules (CIS), the investigation with PL helped to identify the origin of many defects. This could be a great advantage for module producers.

Furthermore, it could be demonstrated that PL imaging of solar cells and modules could be carried out successfully by means of LED excitation instead of hazardous and costly laser excitation. Thus, PL imaging could become a more interesting tool for the PV industry than EL imaging.

As the origin of a defect is not always located in the identified high temperature area or the remarkable dark EL-areas, a combination of EL, PL, and IR techniques is necessary in order to identify as many defects as possible [29].

Disclosure

A poster about this topic was published at the 5th Photovoltaic Technical Conference-Thin Film & Advanced Silicon Solutions, Centre de Congrès, Aix en Provence, May 2014.

TABLE 2: Comparison of characterization methods.

⊕	⊖
	Electroluminescence (EL)
(i) High resolution (ii) Identifiable (a) Faulty laser scribing (b) Process failures (e.g., shunts, layer defects, and TCO corrosion)	(i) Origin of a defect is not identifiable (ii) Difficult to determine influence of defects on cell/module performance (iii) Unremarkable EL-images sometimes supply IR-images with hot areas (iv) Electrical contact necessary
	Photoluminescence (PL)
(i) Contactless (ii) Identifiable (a) Material properties (e.g., reduced minority carrier diffusion length) (b) Process failures	(i) Homogenous illumination source necessary (ii) Module measurements Each cell separately
	Infrared thermography (IR)
(i) Contactless (illuminated) (ii) Identifiable (a) Different thermal behavior (b) Shunts (c) Hot spots (d) Inactive cell parts (e) Moisture	(i) Not contactless (dark) (ii) Not all defects (EL) lead to a temperature increase (iii) High temperature area: not always the origin of defects (iv) Difficult to determine exact position of defects or large number of small spots (v) Not distinguishable between low shunt and high series resistance
	Dark lock-in thermography (DLIT)
(i) Identifiable (a) Different thermal behavior (b) Process failures (e.g., shunts) (ii) Origin of a defect being identifiable	(i) Not contactless (ii) Difficult to detect exact position of defects of large number of small spots (iii) Long measurement period

Conflict of Interests

The authors declare that there is no conflict of interests regarding the publication of this paper.

References

- [1] S. Zamini, "Non-destructive-techniques for quality control of photovoltaic modules: electroluminescence imaging and infrared thermography," *Photovoltaics International Journal, PV-Tech PRO*, no. 15, pp. 127–203, 2012.
- [2] R. Ebner, "Electroluminescence (EL) and infrared (IR) methods for characterizing different module technologies," in *Proceedings of the 26th European Photovoltaic Solar Energy Conference and Exhibition*, Hamburg, Germany, September 2011.
- [3] R. Ebner, "EL an infrared IR methods for characterizing different thin-film module technologies," in *Proceedings of the 3rd International Conference on Thin Film PV*, Munich, Germany, 2011.
- [4] C. Buerhop, "Quality control of PV-modules in the field using infrared-thermography," in *Proceedings of the 26th European Photovoltaic Solar Energy Conference and Exhibition (EU-PVSEC '11)*, Hamburg, Germany, 2011.
- [5] U. Hoyer, C. Buerhop-Lutz, and U. Jahn, "Electroluminescence and infrared imaging for quality improvements of PV modules," in *Proceedings of the 23rd European Photovoltaic Solar Energy Conference and Exhibition (EU-PVSEC '08)*, Valencia, Spain, September 2008.
- [6] U. Hoyer, C. Buerhop-Lutz, and U. Jahn, "Electroluminescence and infrared imaging for quality improvements of PV modules," in *Proceedings of the 23rd European Photovoltaic Solar Energy Conference and Exhibition (EU-PVSEC '08)*, pp. 2913–2916, Valencia, Spain, September 2008.
- [7] U. Hoyer, A. Burkert, R. Auer et al., "Analysis of PV modules by electroluminescence and IR thermography," in *Proceedings of the 24th European Photovoltaic Solar Energy Conference (EU-PVSEC '09)*, pp. 3262–3266, Hamburg, Germany, September 2009.
- [8] O. Breitenstein, *Lock-in Thermography: Basics and Use for Functional Diagnostics of Electronic Components*, Springer, 2003.
- [9] O. Breitenstein, "Lock-in thermography- basics and use for functional diagnostic of electronic module technologies," in *Proceedings of the the PV World Conference & Expo*, Tampa, Fla, USA, 2011.
- [10] M. Ankner, "Analyse von fehlerbildern an dünn-schichtmodulen über das EL-verfahren," in *Proceedings of the 25th PV Symposium*, Bad Staffelstein, Germany, March 2010.
- [11] S. Roy, "Estimation of shunt resistance by electroluminescence imaging," in *Proceedings of the 29th European Photovoltaic Solar Energy Conference and Exhibition*, Amsterdam, The Netherlands, September 2014.
- [12] G. Wang, H. Gong, and J. Zhu, "Failure analysis of dark cells detected by electroluminescence (EL)," in *Proceedings of the 28th European Photovoltaic Solar Energy Conference and Exhibition (EU-PVSEC '14)*, pp. 3173–3179, Amsterdam, The Netherlands, 2014.
- [13] M. Köntges, M. Siebert, D. Hinken, U. Eitner, K. Bothe, and T. Potthof, "Quantitative analysis of PV-modules by electroluminescence images for quality control," in *Proceedings of*

- the 24th European Photovoltaic Solar Energy Conference (EU-PVSEC '09)*, Hamburg, Germany, September 2009.
- [14] T. Weber, "Electroluminescence investigation on thin film modules," in *Proceedings of the 26th European Photovoltaic Solar Energy Conference and Exhibition (EU-PVSEC '11)*, Hamburg, Germany, 2011.
- [15] A. Mansouri, "Defect detection in photovoltaic modules using electroluminescence imaging," in *Proceedings of the Photovoltaic International*, 2010.
- [16] J. L. Crozier, "Identifying voltage dependant features in photovoltaic modules using electroluminescence imaging," in *Proceedings of the 29th European Photovoltaic Solar Energy Conference and Exhibition (EU-PVSEC '14)*, Amsterdam, The Netherlands, 2014.
- [17] T. Trupke, "Fast photoluminescence imaging of silicon wafers," in *Proceedings of the IEEE 4th World Conference on Photovoltaic Energy Conversion*, vol. 1, pp. 928–931, Waikoloa, Hawaii, May 2006.
- [18] A. Lawerenz, "Photoluminescence lifetime using LED arrays excitation source," in *Proceedings of the 25th European Photovoltaic Solar Energy Conference and Exhibition (PVSEC '10)*, Valencia, Spain, 2010.
- [19] M. Bailly, "Photoluminescence lifetime characterization with low pressure sodium lamps," in *Proceedings of the 28th European Photovoltaic Solar Energy Conference and Exhibition (EU-PVSEC '13)*, Paris, France, 2013.
- [20] R. Ebner, "Defect analysis of different photovoltaic modules using electroluminescence (EL) and infrared (IR)-thermography," in *Proceedings of the 25th European Photovoltaic Solar Energy Conference and Exhibition (EU-PVSEC '10)*, Valencia, Spain, 2010.
- [21] A. Helbig, T. Kirchartz, R. Schäffler, J. H. Werner, and U. Rau, "Electroluminescence analysis of Cu(In,Ga)Se₂ thin-film modules," in *Proceedings of the 24th European Photovoltaic Solar Energy Conference (EU-PVSEC '09)*, pp. 2446–2449, Hamburg, Germany, September 2009.
- [22] A. Helbig, T. Kirchartz, R. Schäffler, J. H. Werner, and U. Rau, "Electroluminescence analysis of Cu(In,Ga)Se₂ thin film modules," in *Proceedings of the 24th European Photovoltaic Solar Energy Conference (EU-PVSEC '09)*, pp. 2446–2449, Hamburg, Germany, 2009.
- [23] R. Ebner, "Defect analysis in different photovoltaic modules using electroluminescence (EL) and infrared (IR)-thermography," in *Proceedings of the 25th European Photovoltaic Solar Energy Conference and Exhibition (EU-PVSEC '10)*, Valencia, Spain, 2010.
- [24] U. Hoyer, A. Burkert, R. Auer et al., "Analysis of PV modules by electroluminescence and IR thermography," in *Proceedings of the 24th European Photovoltaic Solar Energy Conference (EU-PVSEC '09)*, pp. 3262–3266, Hamburg, Germany, September 2009.
- [25] S. Johnston, T. Unold, I. Repins et al., "Imaging characterization techniques applied to Cu(In, Ga)Se₂ solar cells," *Journal of Vacuum Science & Technology A*, vol. 28, p. 665, 2010.
- [26] R. Ebner, "Electroluminescence (EL) and infrared (IR) imaging of different module technologies," in *Proceedings of the PV World Conference & Expo*, Tampa, Fla, USA, 2011.
- [27] R. Ebner, B. Kubicek, and G. Ujvari, "Non-destructive techniques for quality control of PV modules: Infrared thermography, electro- and photoluminescence imaging," in *Proceedings of the 39th Annual Conference of the IEEE Industrial Electronics Society (IECON '13)*, pp. 8104–8109, Vienna, Austria, November 2013.
- [28] T. Trupke, R. A. Bardos, M. D. Abbott, F. W. Chen, J. E. Cotter, and A. Lorenz, "Fast photoluminescence imaging of silicon wafers," in *Proceedings of the IEEE 4th World Conference on Photovoltaic Energy Conversion (WCPEC '06)*, vol. 1, pp. 928–931, May 2006.
- [29] R. Ebner, S. Zamini, and G. Újvári, "Defect analysis in different photovoltaic modules using electroluminescence (EL) and infrared (IR)-thermography," in *Proceedings of the 25th European Photovoltaic Solar Energy Conference and Exhibition (PVSEC '10)*, pp. 333–336, Valencia, Spain, September 2010.

Research Article

Measurements and Simulations on the Mechanisms of Efficiency Losses in HIT Solar Cells

**Silvio Pierro,¹ Andrea Scuto,² Luca Valenti,² Marina Foti,³ Anna Battaglia,⁴
Giovanni Mannino,² Cosimo Gerardi,³ Felice Crupi,¹ and Salvatore Lombardo²**

¹*DIMES, Università della Calabria, Via P. Bucci, 87036 Rende, Italy*

²*CNR-IMM, Strada VIII 5, 95121 Catania, Italy*

³*STMicronics, Stradale Primosole 50, 95121 Catania, Italy*

⁴*3SUN S.r.l., Contrada Blocco Torrazze, sn, 95121 Catania, Italy*

Correspondence should be addressed to Silvio Pierro; pierro@dimes.unical.it

Received 1 October 2014; Revised 17 February 2015; Accepted 18 February 2015

Academic Editor: Olindo Isabella

Copyright © 2015 Silvio Pierro et al. This is an open access article distributed under the Creative Commons Attribution License, which permits unrestricted use, distribution, and reproduction in any medium, provided the original work is properly cited.

We study the electrical and the optical behavior of HIT solar cell by means of measurements and optoelectrical simulations by TCAD simulations. We compare the HIT solar cell with a conventional crystalline silicon solar cell to identify the strengths and weaknesses of the HIT technology. Results highlight different mechanisms of electrical and optical efficiency losses caused by the presence of the amorphous silicon layer. The higher resistivity of the a-Si layers implies a smaller distance between the metal lines that causes a higher shadowing. The worst optical coupling between the amorphous silicon and the antireflective coating implies a slight increase of reflectivity around the 600 nm wavelength.

1. Introduction

The heterostructure with intrinsic thin layer solar cell, so called HIT, is the most promising monocrystalline silicon based technology to enhance the cost/efficiency factor [1]. This assumption is based on the enhancement made by the HIT with respect to a monocrystalline solar cell by the cost reduction introduced by the lower thermal budget, and by the increasing of the open circuit voltage thanks to the heterojunction barrier that decreases the minority current [2]. From the previous considerations we expect a strong increase in the HIT performance with respect to the c-Si technology. The base research-cell efficiencies reported in literature tell us that the efficiency of the HIT solar cell is slightly higher than the efficiency of the microcrystalline bulk solar cell (25.6% of HIT against 25% of bulk microcrystalline) [3]. Subsequent improvements have allowed HIT solar cells to reach the efficiency of 25.6% [4]. Actually, the main focus to increase the HIT efficiency is connected to the surface

recombination velocity at amorphous-crystalline interface [5]. In order to further increase the cell efficiency we need to understand the main causes of efficiency losses and how to reduce them.

This paper focuses the attention on the physical aspects that affect the HIT solar cells different from technological aspects as surface passivation or defect densities. For this purpose we compare measurements of bulk crystalline silicon solar cell with the equivalent HIT solar cell. Furthermore, by using a commercial TCAD simulator [6] tuned with device measurements, we intend to investigate the main loss mechanisms for both structures and identify the main problems of the HIT technology.

The remainder of this paper is organized as follows. Section 2 describes the process details of the realized samples and the simulation setup. Section 3 reports the experimental and numerical results and discusses the main phenomena affecting the HIT efficiency. Section 4 reports the conclusions of this work.

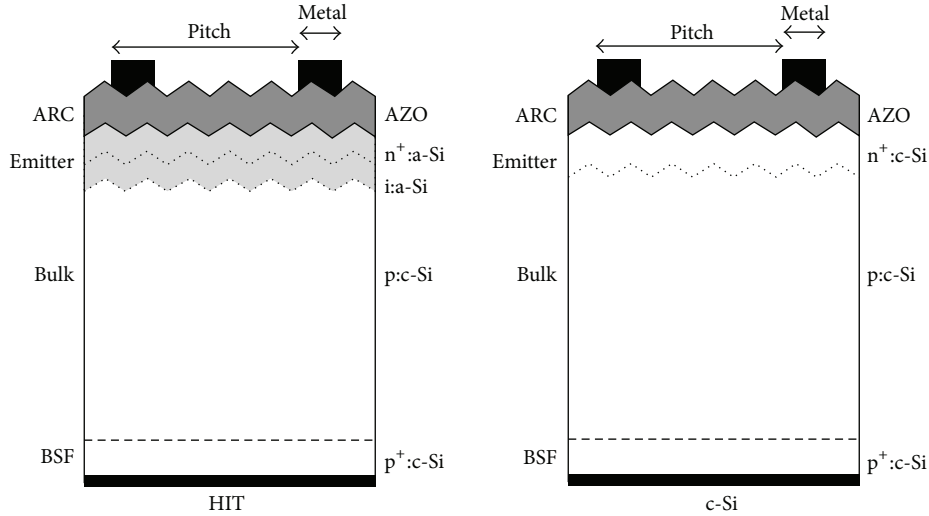


FIGURE 1: Schematic cross section of HIT and crystalline solar cell.

2. Experimental Details

The HIT structure is presented in Figure 1. Starting from a p-type CZ wafer, by a HF etching process a front random pyramids texturing is built. A highly doped p-type layer is deposited on the back surface, which is crystallized by a thermal process, forming the back surface field (BSF) layer. The intrinsic and the n-type amorphous layers are deposited by inductively coupled plasma chemical vapour deposition (ICPCVD) on the top surface of the wafer. The aluminum doped zinc oxide (AZO) is used as antireflective coating (ARC) layer and is grown by sputtering. To finalize the structure, the back metallization covers the entire device and is a Ti/Pt/Au multilayer; the top metal is made by screen printing of a silver paste. A double HIT structure was not realized, since the amorphous BSF does not add enhancement on a p-type HIT solar cell [7, 8]. For comparison purpose, we realized the crystalline structure shown in Figure 1. The device parameters of the HIT and the reference structures are reported in Table 1. The key difference between the two structures is the emitter region, which is crystallized by a thermal process in the case of the crystalline structure.

The electrical simulation setup uses a drift-diffusion model with Fermi statistics, with the Schenk bandgap narrowing model [9] and the Slotboom model for free mobility carrier degradation [10]. The Auger and Radiative recombination has been added as far as the SRH recombination for both bulk and surfaces. For the crystalline solar cell, the surface recombination velocity of c-Si/AZO interface uses the SRH surface recombination model, tuned with literature results [11]; the doping level for both emitter and BSF layers is tuned with spreading resistance measurements on our devices. The HIT solar cell is made by replacing the emitter with the i/n a-Si:H layers. The HIT physical model requires adding the thermionic current and the surface recombination at the amorphous-crystalline interface [12, 13]. The amorphous silicon density of states (DOS) is modeled by three Gaussian

TABLE 1: Measurements of electrical and geometrical parameters for HIT and c-Si structures.

	Unit	HIT	c-Si
Sheet resistance	Ω/sq	14	7.78
AZO thickness	nm	91	88
Emitter thickness	nm	—	50
Emitter doping	cm^{-3}	—	1×10^{20}
n-type a-Si:H thickness	nm	10	—
n-type a-Si:H doping	cm^{-3}	1×10^{18}	—
i-type a-Si:H thickness	nm	5	—
Emitter/AZO SRV	cm/s	8.7×10^4	2.1×10^4
i/n a-Si SRV	cm/s	—	10^2
Electrical measurements			
Voc	V	0.563	0.552
Isc	mA/cm^2	25.0	30.5
FF	—	0.527	0.579
Efficiency	%	7.4	9.7

distributions, two for the conduction and valence band tails and one for the mid gap defect concentration [13]. The most relevant a-Si:H electrical parameters used in the simulations are reported in Table 2. The optical simulation solves an extended version of the Transfer Matrix Method with diffused and direct light to take into account surface texturing [14, 15]. The coherent light follows the direct path, while the diffused ray follows a scattered function, the so-called angular distribution function [16]. The ratio between the scattered and direct ray is the haze parameter. In the simulation above, the haze parameter has been set to 0.73 and the haze profile follows a square cosine law. The values of refractive index and absorption coefficient for the materials used in the solar cell are consistent with literature data [17].

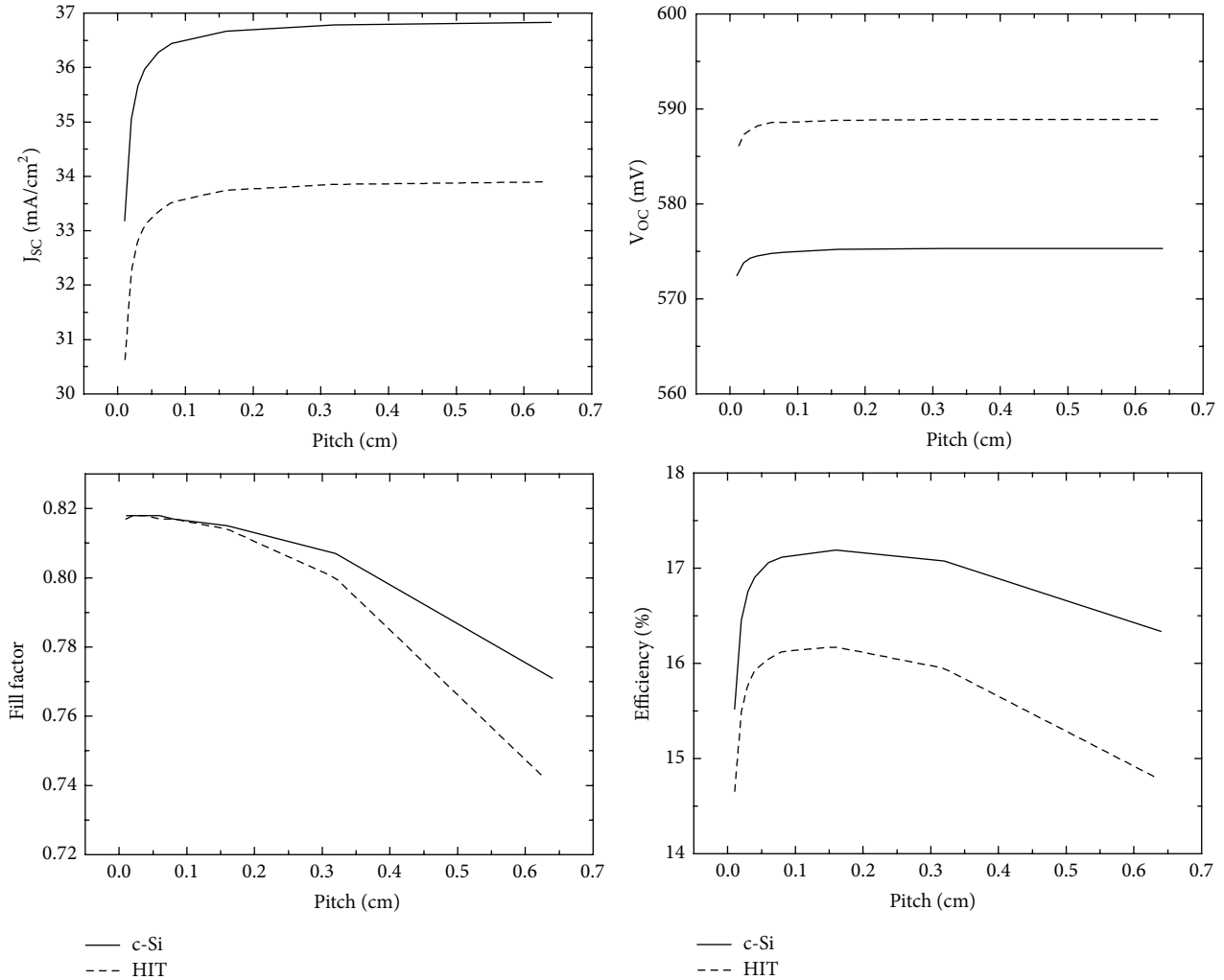


FIGURE 2: Simulated electrical parameters as a function of sun pitch length. The HIT shows a lower efficiency compared to the crystalline silicon structure.

3. Results and Discussion

Figure 2 shows the main electrical parameters of HIT and crystalline (subsequently c-Si) solar cells as a function of pitch. According to literature, the open circuit voltage of the HIT cell is greater than c-Si [2]; on the other hand, the short circuit current and the fill factor are lower. This translates into a lower efficiency value of the HIT compared to c-Si, and the difference increases as the pitch increases. Figure 3 shows the optimized pitch distance that reaches the highest efficiency; this value reaches a trade-off between the shadowing losses and the fill factor that show opposite trends as a function of pitch length. Increasing the sun concentration, the pitch distance decreases faster in the c-Si solar cell compared to HIT, thus increasing the efficiency of HIT compared to c-Si. In order to understand the fill factor loss we analyze simulation results for both HIT and c-Si structures at maximum power peak; results are shown in Figure 4, where the black lines are the current path and the color is the current density. It is worth noting that the current

flows vertically inside the bulk, while it goes in direction of the contact in both the emitter and the AZO regions. The current direction into the emitter causes an increase of the density current near to the contact, thus increasing the electrostatic potential loss inside the emitter. This effect depends on the pitch width and the emitter resistivity. In order to gain insight on the lateral loss effect, Figure 5 compares the electrostatic potential along the c-Si/a-Si heterointerface for the HIT structure and the electrostatic potential at the p-n junction for the c-Si structure. Moving away from the contact, the potential decreases due to the emitter and AZO resistivity. The potential loss is highly close to the contact due to the higher current density and is higher in the HIT compared to the reference one, due to the higher resistivity of a-Si compared to c-Si. The electrostatic potential at the interface causes an increase in the dark current that decreases the photogenerated current. This effect depends on the operation condition. At short circuit current condition, the dark current is low with respect to the photogenerated current, so the effect can be neglected. By increasing the voltage, the diode current

TABLE 2: Main physical parameters for the a-Si material for simulation.

Name	Unit	Value
Electron affinity	eV	3.9
Bandgap	eV	1.74
Electron mobility	$\text{cm}^2\text{V}^{-1}\text{s}^{-1}$	20
Hole mobility	$\text{cm}^2\text{V}^{-1}\text{s}^{-1}$	2
DOS in CB	cm^{-3}	2.5×10^{20}
DOS in VB	cm^{-3}	2.5×10^{20}
Conduction band tail		
Traps concentration	cm^{-3}	1×10^{18}
Standard deviation	—	0.08
Capture cross section for e^-	cm^{-2}	1×10^{-16}
Valence band tail		
Traps concentration	cm^{-3}	1×10^{18}
Standard deviation	—	0.08
Capture cross section for e^-	cm^{-2}	1×10^{-19}
Mid gap		
Traps concentration	cm^{-3}	1×10^{16}
Standard deviation	—	0.15
Capture cross section	cm^{-2}	1×10^{-16}

becomes relevant with respect to the photogenerated current, and the effect cannot be neglected anymore. At open circuit voltage, the diode dark current is equal to the photogenerated current, since the dark current depends on the lateral effect; there is an open circuit voltage reduction. This phenomenon is present in both HIT and crystalline devices. As can be seen from Figure 5, the potential variation in the HIT structure is higher than the crystalline solar cell because of the higher emitter resistivity; the higher potential variation produces a decrease in the fill factor and in the open circuit voltage. In order to reduce this effect we need to shrink the pitch, thus causing a higher shadowing that decreases efficiency. The optimum value between lateral losses and shadowing is shown in Figure 3. Because of the previous effect, the HIT solar cell needs a smaller pitch than the c-Si, but with increasing sun concentration this effect tends to decrease, since the c-Si solar cell pitch decreases faster than the HIT and when the two pitch values are the same the HIT efficiency becomes greater than the c-Si one.

Figure 6 shows the reflectivity of the devices for both simulations and measurements. As can be seen, the HIT structure shows a higher reflectivity from 300 nm to 600 nm with respect to the c-Si structure. This reflectivity increase translates into a lower energy absorbed by the solar cell and less energy. Figure 7 shows the difference of spectral power density absorbed by the HIT and c-Si solar cell with respect to the AM1.5G spectral density; this is an optical analysis derived from the overall reflectivity and transmittance; we cannot notice electrical issues and cannot determine which layer adsorbs the light. The optical stack of HIT structure differs from the c-Si structure by the addition

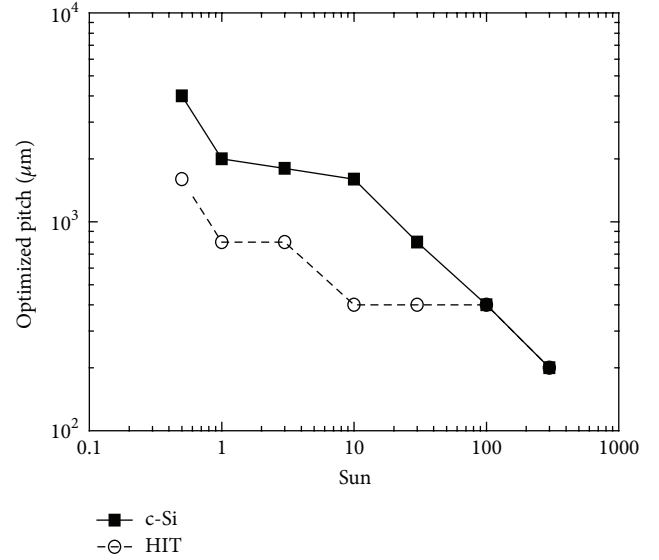


FIGURE 3: Optimized pitch for planar solar cell with metal line width equal to $100 \mu\text{m}$ in HIT and c-Si solar cell. Lower values are observed for HIT, unless at very high sun concentration.

of the two a-Si:H layers, the n-doped and intrinsic layers (stack successfully called a-Si:H) in between the silicon bulk and the AZO layer. From literature we know that a good antireflective layer in between two materials must obey some rules; in particular, the thickness of the layer must ensure the destructive interference of the reflected wave and the refractive index must be as close as possible to the square root of the product of the refractive indices of the two materials. If the layers are more than one, we must use the same rule for the two neighbor materials. Figure 8 shows the refractive index of the c-Si, a-Si:H, and AZO material compared with the optimum refractive index for the case of 1 layer in between c-Si and the air and the case of 2 layers (like HIT structure). As can be seen, the AZO is a good material to use as single inner layer for c-Si solar cell; this ensures a low reflectivity in c-Si solar cell. The a-Si:H shows a refractive index similar to the c-Si for wavelength higher than 550 nm; then the reflectivity in this wavelength range should be approximated to the c-Si solar cell. For smaller frequencies, the a-Si:H and c-Si refractive indices are no more similar; this implies that the optical behavior must follow the model with 2 layers in between the silicon and the air. Under this range, the AZO is still a good material, but the a-Si:H is close enough to the optimum level for wavelength smaller than 400 nm; before this value the worst index matching does not ensure a low reflectivity. This analysis is in good agreement with the optical measurements shown in Figure 6. The integral of the reflectivity value is used as a figure of merit for the system and Figure 9 shows this integral as a function of the a-Si:H layer thickness compared to the structure with no a-Si:H layer. The inset figure shows that the AZO reaches a minimum of reflectivity when its thickness is 91 nm and this value is not dependent on the a-Si:H thickness. The a-Si:H thickness affects the reflectance and there is a maximum of reflectance

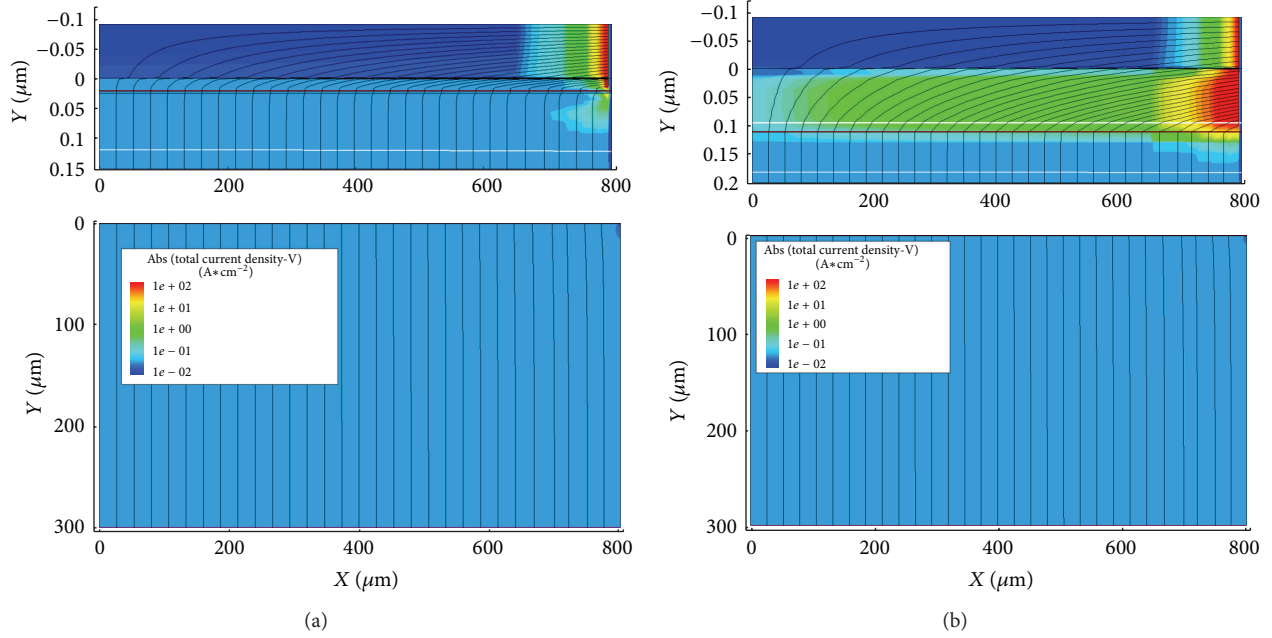


FIGURE 4: Cross section of HIT (a) and reference (b) solar cell for AM 1.5G illumination spectrum, at the voltage of maximum power peak, the top image is a zoom on the emitter region. Lines are for the current and colors for current density. The emitter contact is on the right.

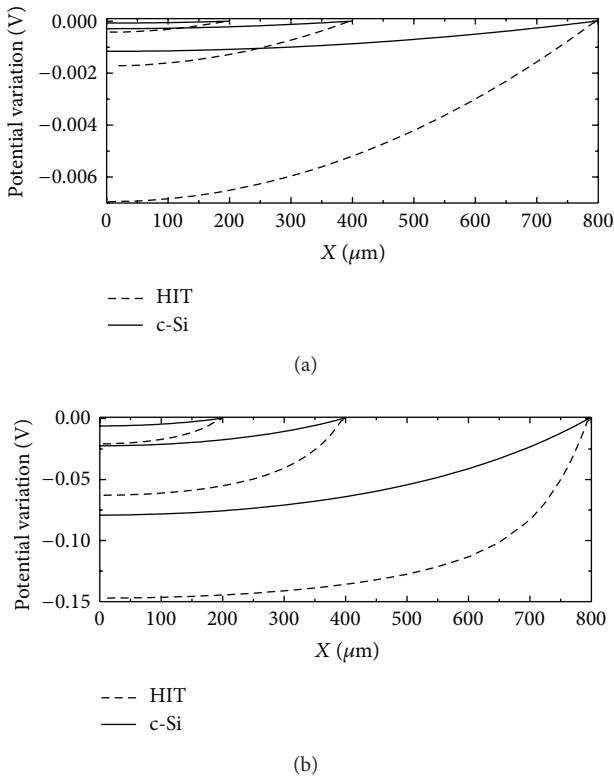


FIGURE 5: Horizontal cutline of the electrostatic potential profile at amorphous/crystalline heterojunction in HIT and at junction level for reference solar cell. Both cells are at maximum power condition. (a) For sun = 1 and (b) for sun = 100. The metal width is 10 μm and the pitch is 400, 800, and 1600 μm.

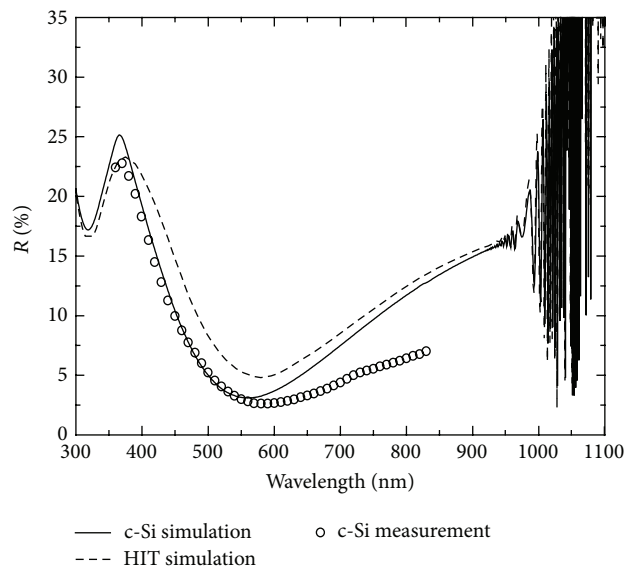


FIGURE 6: Measured and simulated reflectivity of c-Si solar cell and HIT solar cell with AZO as ARC. HIT solar cell exhibits a lower (higher) reflectivity at lower (higher) wavelengths with respect to the c-Si solar cell. The minimum reflectivity value for the HIT solar cell occurs at higher wavelength than the c-Si solar cell.

at 20 nm. This result tells us to use a very thin a-Si:H layer or a greater one. But using a thick layer implies a bigger series resistance and a layer thinner than 5 nm can be a problem for quantum effects [18].

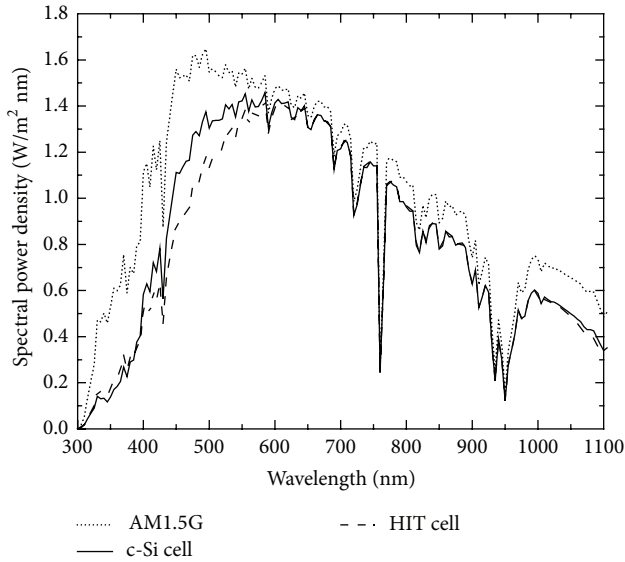


FIGURE 7: Spectral power density transmitted to the solar cell compared to the solar spectrum AM1.5G. This measurement shows a difference between the crystalline and HIT cell from 400 nm to 600 nm, related to the higher reflectivity.

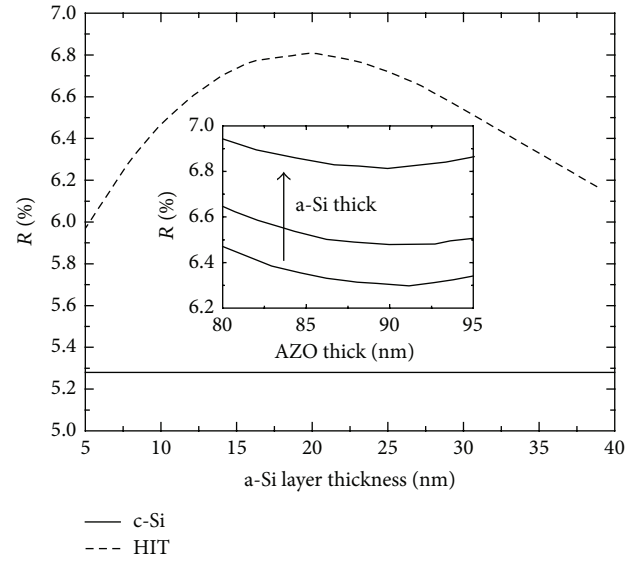


FIGURE 9: Total reflectivity of HIT as a function of a-Si:H layer thickness compared to c-Si. Inset figure for total reflectivity as a function of AZO thickness for a-Si:H layer thickness of 8, 10, and 20 nm.

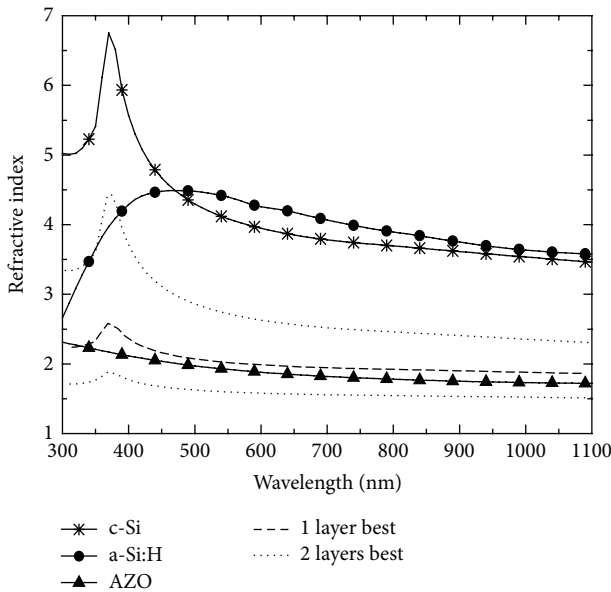


FIGURE 8: Refractive index of c-Si, a-Si:H, and AZO (by ellipsometry measures) compared to the ideal refractive index of an antireflective coating composed of 1 layer and 2 layers.

4. Conclusions

In this paper we compared the HIT solar cell with a c-Si solar cell to identify the main problems of the HIT technology. We made measurements and simulation and by comparing the optimized structure for both technologies we noticed two losses differences into HIT. A lower fill factor and a higher reflectivity for the HIT solar cell. The fill factor decrease is due to a higher potential loss along the p-n junction that causes

a higher diode current. To prevent this we need to shrink the pitch, causing a higher shadowing. The lower short circuit current is caused by higher reflection losses into HIT. This is caused by the worst optical coupling between the amorphous silicon and the antireflective coating in the wavelength range from 400 nm to 600 nm; we cannot reduce this effect since the reduction is related to optical properties of the amorphous layer; to reduce the reflectivity we must shrink the a-Si layer, but the thickness cannot be smaller than the value in use to prevent quantum effects.

Conflict of Interests

The authors certify that they have no affiliations with or involvement in any organization or entity with any financial interest (such as honoraria; educational grants; participation in speakers' bureaus; membership, employment, consultancies, stock ownership, or other equity interests; and expert testimony or patent-licensing arrangements) or nonfinancial interest (such as personal or professional relationships, affiliations, knowledge, or beliefs) in the subject matter or materials discussed in this paper.

References

- [1] M. Tanaka, M. Taguchi, T. Matsuyama et al., "Development of new a-Si/c-Si heterojunction solar cells: ACJ-HIT (Artificially Constructed Junction-Heterojunction with Intrinsic Thin-layer)," *Japanese Journal of Applied Physics*, vol. 31, no. 11, pp. 3518–3522, 1992.
- [2] M. Nath, P. Chatterjee, J. Damon-Lacoste, and P. Roca i Cabarrocas, "Criteria for improved open-circuit voltage in a-Si:H(N)/c-Si(P) front heterojunction with intrinsic thin layer

- solar cells,” *Journal of Applied Physics*, vol. 103, no. 3, Article ID 034506, 2008.
- [3] M. A. Green, K. Emery, Y. Hishikawa, W. Warta, and E. D. Dunlop, “Solar cell efficiency tables (version 39),” *Progress in Photovoltaics: Research and Applications*, vol. 20, no. 1, pp. 12–20, 2012.
- [4] S. Tohoda, D. Fujishima, A. Yano et al., “Future directions for higher-efficiency HIT solar cells using a Thin Silicon Wafer,” *Journal of Non-Crystalline Solids*, vol. 358, no. 17, pp. 2219–2222, 2012.
- [5] T. Mishima, M. Taguchi, H. Sakata, and E. Maruyama, “Development status of high-efficiency HIT solar cells,” *Solar Energy Materials & Solar Cells*, vol. 95, no. 1, pp. 18–21, 2011.
- [6] SYNOPSIS, *Sentaurus Device User Manual*, chapter 21, 2013.
- [7] L. Zhao, C. L. Zhou, H. L. Li, H. W. Diao, and W. J. Wang, “Design optimization of bifacial HIT solar cells on p-type silicon substrates by simulation,” *Solar Energy Materials and Solar Cells*, vol. 92, no. 6, pp. 673–681, 2008.
- [8] A. Datta and P. Chatterjee, “Computer modeling of heterojunction with intrinsic thin layer ‘HIT’ solar cells: sensitivity issues and insights gained,” in *Solar Cells—Thin-Film Technologies*, L. A. Kosyachenko, Ed., InTech, 2011.
- [9] A. Schenk, “Finite-temperature full random-phase approximation model of band gap narrowing for silicon device simulation,” *Journal of Applied Physics*, vol. 84, no. 7, pp. 3684–3695, 1998.
- [10] D. B. M. Klaassen, “A unified mobility model for device simulation—I. Model equations and concentration dependence,” *Solid-State Electronics*, vol. 35, no. 7, pp. 953–959, 1992.
- [11] M. J. Kerr, J. Schmidt, A. Cuevas, and J. H. Bultman, “Surface recombination velocity of phosphorus-diffused silicon solar cell emitters passivated with plasma enhanced chemical vapor deposited silicon nitride and thermal silicon oxide,” *Journal of Applied Physics*, vol. 89, no. 7, pp. 3821–3826, 2001.
- [12] A. Kanevce and W. K. Metzger, “The role of amorphous silicon and tunneling in heterojunction with intrinsic thin layer (HIT) solar cells,” *Journal of Applied Physics*, vol. 105, no. 9, Article ID 094507, 2009.
- [13] K. Horio and H. Yanai, “Numerical modeling of heterojunctions including the thermionic emission mechanism at the heterojunction interface,” *IEEE Transactions on Electron Devices*, vol. 37, no. 4, pp. 1093–1098, 1990.
- [14] A. Gerrard and J. M. Burch, *Introduction to Matrix Methods in Optics*, Dover Publications, 2012.
- [15] J. Krč, F. Smole, and M. Topič, “Analysis of light scattering in amorphous Si:H solar cells by a one-dimensional semi-coherent optical model,” *Progress in Photovoltaics: Research and Applications*, vol. 11, no. 1, pp. 15–26, 2003.
- [16] P. Beckmann and A. Spizzichino, *The Scattering of Electromagnetic Waves from Rough Surfaces*, Artech House, Norwood, Mass, USA, 1987.
- [17] E. D. Palik, *Handbook of Optical Constants of Solids*, Academic Press, Boston, Mass, USA, 1985.
- [18] A. Muoz, N. Chetty, and R. M. Martin, “Modification of heterojunction band offsets by thin layers at interfaces: role of the interface dipole,” *Physical Review B*, vol. 41, no. 5, pp. 2976–2981, 1990.